Mathematical Modelling of Cancer Treatments Involving Radiation Therapy and Hypoxia-Activated Prodrugs

by

Cameron Meaney

A thesis
presented to the University of Waterloo
in fulfillment of the
thesis requirement for the degree of
Master of Mathematics
in
Applied Mathematics

Waterloo, Ontario, Canada, 2019

Author's Declarations

This thesis consists of material all of which I authored or co-authored: see Statement of Contributions included in the thesis. This is a true copy of the thesis, including any required final revisions, as accepted by my examiners.

I understand that my thesis may be made electronically available to the public.

Statement of Contributions

This thesis contains three research works either published or in submission to scientific journals. The author lists for each paper and contributions made by myself and various coauthors are as follows:

Spatial Optimization for Radiation Therapy of Brain Tumours

Cameron Meaney[1], Marek Stastna[1], Mehran Kardar[2], Mohammad Kohandel[1]
1 Department of Applied Mathematics, University of Waterloo, Waterloo, Ontario, Canada
2 Department of Physics, Massachusetts Institute of Technology, Cambridge, Massachusetts, United States of America

C. Meaney contributed to the design of the computer code, running of simulations, derivation of analytical results, and the writing and editing of manuscipt. M. Stastna contributed to the design of the computer code, running of simulations, and the editing of the manuscript. M. Kardar contributed to the derivation of analytical results, and the editing of the manuscript. M. Kohandel contributed to the derivation of analytical results, and the writing and editing of the manuscript.

Role of Hypoxia-Activated Prodrugs in Combination with Radiation Therapy: An *In Silico* Approach

Cameron Meaney[1], Gibin Powathil[2], Ala Yaromina[3], Ludwig Dubois[3], Philippe Lambin[3], Mohammad Kohandel[1]
1 Department of Applied Mathematics, University of Waterloo, Waterloo, Ontario, Canada
2 Department of Mathematics, College of Science, Swansea University, United Kingdom
3 Department of Precision Medicine, The M-Lab, GROW School for Oncology and Developmental Biology, Maastricht University Medical Centre, Maastricht, The Netherlands

C. Meaney contributed to the design of the mathematical model, design of the computer code, running of simulations, and the writing and editing of the manuscript. G. Powathil contributed to the design of the mathematical model, design of the computer code, running of simulations, and the writing and editing of the manuscript. A. Yaromina, L. Dubois, and P. Lambin contributed to the editing of the manuscript. M. Kohandel contributed to the design of the mathematical model, design of the computer code, and the writing and editing of the manuscript.

***In Silico* Analysis of Hypoxia-Activated Prodrugs in Combination with Anti-Angiogenic Therapy through Nanocell Delivery**

Cameron Meaney[1], Sander Rhebergen[1], Mohammad Kohandel[1]
1 Department of Applied Mathematics, University of Waterloo, Waterloo, Ontario, Canada

C. Meaney contributed to the design of the mathematical model, design of the computer code, running of simulations, and the writing and editing of the manuscript. S. Rhebergen contributed to the design of the compute code, running of simulations, and the editing of the manuscript. M. Kohandel conributed to the design of the mathematical model and the writing and editing of the manuscript.

Abstract

Cancer is one of the world's deadliest diseases despite immense investments into oncological research in recent years. Although great strides have been made in our understanding of cancer, much remains unknown regarding its genesis, progression, and optimal treatment. The benefits of mathematical modelling have been realized in many fields of science, and oncology is no exception. Mathematical modelling has become increasingly popular in recent years and today, studies involving both biologists and mathematicians are rather commonplace. This thesis focuses on mathematical oncology, detailing three distinct research works involving the mathematical analysis of cancer. They specifically focus on modelling the applications of various treatment methods including external-beam radiation therapy, hypoxia-activated prodrugs, antiangiogenic agents, and drug-carrying nanocells. The mathematics involves partial differential equation models solved analytically and by using various computational methods. Altogether, the analyses herein show that mathematical modelling is an invaluable tool in oncology which will be a crucial part of future research.

Acknowledgements

First and foremost, I would like to thank my supervisor Dr. Mohammad Kohandel. In addition to being an excellent graduate supervisor, he allowed me to get my foot in the door with academic research as an undergraduate student. His willingness to provide me with exciting opportunities and his patience to answer my many questions is much appreciated. I sincerely look forward to continuing our work together.

I would also like to thank Dr. Matt Scott for his mentorship throughout my schooling. My love for the world of mathematical biology was discovered during my summer working with him in the lab. Thanks to him for the opportunity and for the enthusiasm.

Additionally, I would like to thank Dr. Mehran Kardar for his guidance and supervision while I completed part of my degree at the Massachusetts Institute of Technology in Cambridge, MA. My time spent working with him was extremely valuable and enjoyable.

Appreciation also goes to Dr. Siv Sivaloganathan and the many coauthors on parts of the work herein including Dr. Gibin Powathil, Dr. Sander Rhebergen, Dr. Marek Stastna, Dr. Ludwig Dubois, Dr. Philippe Lambin, and Dr. Ala Yaromina.

Finally, the financial support provided by the Natural Science and Engineering Research Council of Canada, Mitacs, the University of Waterloo, and the Government of Ontario is gratefully acknowledged.

Table of Contents

List of Figures

List of Tables

List of Abbreviations

AA Anti-Angiogenic Agents 4, 45–51, 54, 56, 61, 64, 67–69

AHAP Activated Hypoxia-Activated Prodrugs 32–34

Br-IPM Bromo-Isophosphoramide Mustard 44, 46, 51, 61, 63

HAP Hypoxia-Activated Prodrugs 3, 27–51, 54, 56, 57, 61, 64, 67–69

HIF-1α Hypoxia-Inducible Factor 48

MRI Magnetic Resonance Images 7, 69

NTCP Normal Tissue Control Probability 7, 25

ODE Ordinary Differential Equation 13

OER Oxygen Enhancement Ratio 52

PDE Partial Differential Equation 13, 56, 69

TCP Tumour Control Probability 6, 7, 9, 10, 24, 25

TGF-β Tumour Growth Factor - β 47

TSP-1 Thrombospondin-1 47

VEGF Vascular Endothelial Growth Factor 47

XRT External-Beam Radiation Therapy 3, 5, 6, 8, 9, 12, 13, 19, 24, 25, 69, 84

Chapter 1

Introduction

1.1 Cancer Background

Cancer is best described as a disease of the cells characterized by unregulated proliferation and invasion caused by underlying genetic mutations. As cancer is not one single disease, but rather a category encompassing similar diseases, it is difficult to be more precise than the above definition. Instead, cancer is commonly defined by the presentation of a subset of traits known to be regularly associated with tumours. These traits, termed the 'Hallmarks of Cancer' by Hanahan and Weinberg, describe the behaviours typical of cancer cells which result in, or accompany, their problematic growth [35]. Modern-day cancer treatments are often designed with these hallmarks in mind, seeking to counteract or take advantage of them directly. These treatments are generally effective, increasing patient survival time and quality of life for nearly all cancers. Unfortunately, existing treatments are often difficult to implement or involve adverse side effects for patients, and while many candidate treatments are promising, they frequently fail to meet necessary efficacy standards. Furthermore, cancer remains Canada's deadliest disease, accounting for over 30% of all deaths despite considerable investments into oncological research [15]. Approximately half of Canadians develop cancer during their lifetime, and cancer is the cause of death for half of those afflicted [15]. Questions in oncology are some of the most pressing in all of science as much remains unknown about the genesis, progression, and optimal treatment of tumours. Even so, researchers continue to be optimistic for the future of cancer, continually championing improved understanding and new advancements.

A timeline of humanity's knowledge of cancer can be loosely broken into three stages. The first of these stages began around 400BC when Hippocrates provided the first hypoth-

esis of cancer, postulating that an accumulation of "black bile" (the result of an unbalanced personality) was the cause of tumours [21]. Naturally, this was emphatically disproven, though it survived as the dominant theory for nearly two millennia, during which time our knowledge of cancer was decidedly primitive. The second stage began at the end of the 19$^{\text{th}}$ century when increased cancer rates due to carcinogenic occupational hazards spurred a renewed interest in cancer research [100]. In this stage, improvements in our understanding of cancer came along with improvements in our understanding of molecular biology itself, particularly in the discovery of genetics and DNA. A similar story has evolved in the modern stage, where oncology has been propelled forward in bursts by the advent of exciting medical technologies including medical imaging, biomarking, and genetic screening. The phenomenon of 'flurries' of scientific discoveries is not unique to oncology. Physics, for example, underwent distinct periods of rapid advancement throughout history, most notably during the early 20$^{\text{th}}$ century with the theories of quantum mechanics, relativity, *etc.* Interestingly, the birth of modern physics has been largely attributed to the widespread incorporation of mathematics into the physical sciences. Conversely, the integration of mathematics into biology and medicine started significantly later, and the full potential of the combination is yet to be realized. Accordingly, many believe that the realization of this potential will spark a revolution in the 21$^{\text{st}}$ century for biology and medicine much as it did in the 20$^{\text{th}}$ century for physics. This thesis focuses on one part of that potential revolution and what could be considered the fourth stage in the history of cancer: mathematical oncology, which broadly refers to the use of mathematical and computational techniques to answer questions related to the progression and treatment of cancer.

1.2 Mathematical Modelling in Cancer

As quantifiable evidence is arguably the defining trait of modern science, it is unsurprising that mathematical modelling has gained popularity. In oncology, the use of mathematical modelling has increased steadily over the past few decades, largely due to the dramatic rise in availability of biological data created by modern medical technologies [5]. With this increase has been a wider acceptance of modelling by biologists and clinicians, a group which has been historically slow to embrace fundamental changes to their field. Today, studies involving both experimentalists and mathematicians are commonplace with many experiments designed specifically to be validated by accompanying mathematical analyses. The amount of these collaborations is expected to grow in future years with some even speculating fundamental changes to medical testing procedures themselves - indeed, *in silico* drug trials are a promising addition to the process [71].

Mathematical modelling does not simply pose a theoretical future benefit to oncological research: these techniques have already been applied to clinical and experimental situations, extending our knowledge and improving existing techniques. Tumour angiogenesis, oxygen transport, immune system evasion, various treatment methods, as well as many other cancer-related topics have all been examined using mathematical models (see [8, 42, 43, 75, 87] for example).

1.3 Outline of Thesis

This thesis contains three individual research works on mathematical oncology published or in submission to scientific journals. I, Cameron Meaney, am the first author on each of these pieces and was responsible for the majority of the work on each (see Statement of Contributions). Each work is included as its own chapter herein, minimally altered to maintain consistency in formatting and adhere to the specifications as required by the University of Waterloo. The title of each chapter corresponds directly to the title of the published or submitted work and the text of each paper is otherwise unchanged from their accepted or most recent version as of June 5th, 2019.

Chapter 2 contains the paper *Spatial Optimization for Radiation Therapy of Brain Tumours* which was published in *PLOS ONE* on June 28th, 2019. This work develops a mathematical model which is used to optimize the spatial application of External-Beam Radiation Therapy (XRT). It utilizes both analytical and computational mathematical methods as well as data from MRI imaging.

The paper *Role of Hypoxia-Activated Prodrugs in Combination with Radiation Therapy: An In Silico Approach* is the topic of chapter 3. It was published in *Mathematical Biosciences and Engineering* on July 4th, 2019. This work develops a mathematical model describing the action of Hypoxia-Activated Prodrugs (HAP) in a tumour. The model is then used to compare the efficacy of HAPs in tumours of different hypoxic levels as well as examine the optimal treatment scheduling of a combination of HAPs with radiation therapy.

Chapter 4 consists of the paper *In Silico Analysis of Hypoxia-Activated Prodrugs in Combination with Anti-Angiogenic Therapy through Nanocell Delivery* which was submitted for publication to *Computational and Mathematical Methods in Medicine* on May 31st, 2019. This paper develops a mathematical model to address the problem of inefficient delivery of HAPs to a tumour due to overvascularization. It mathematically establishes and deciphers the dilemma of HAP delivery vs. activation when HAPs are used with

Anti-Angiogenic Agents (AA). The dilemma is solved with the use of drug nanocells which achieve improved delivery while maintaining high activation.

Relevant biological background and previous literature is given within each chapter as necessary. A summary of the thesis and its contained works is provided in chapter 5 along with directions for future studies and extensions.

Chapter 2

Spatial Optimization for Radiation Therapy of Brain Tumours

Abstract

Glioblastomas are the most common primary brain tumours. They are known for their highly aggressive growth and invasion, leading to short survival times. Treatments for glioblastomas commonly involve a combination of surgical intervention, chemotherapy, and external-beam radiation therapy (XRT). Previous works have not only successfully modelled the natural growth of glioblastomas *in vivo*, but also show potential for the prediction of response to radiation prior to treatment. This suggests that the efficacy of XRT can be optimized before treatment in order to yield longer survival times. However, while current efforts focus on optimal scheduling of radiotherapy treatment, they do not include a similarly sophisticated spatial optimization. In an effort to improve XRT, we present a method for the spatial optimization of radiation profiles. We expand upon previous results in the general problem and examine the more physically reasonable cases of 1-step and 2-step radiation profiles during the first and second XRT fractions. The results show that by including spatial optimization in XRT, while retaining a constant prescribed total dose amount, we are able to increase the total cell kill from the clinically-applied uniform case.

2.1 Introduction

Glioblastomas are the most aggressive, and unfortunately most common, form of primary brain tumour [11, 12, 20, 59, 63]. They are characterized by rapid growth and invasiveness, yielding survival times that seldom exceed a year [23]. Because of this, treatments for glioblastomas are swift and aggressive, usually involving a combination of surgical intervention, chemotherapy, and external-beam radiation therapy (XRT). Furthermore, the tendency for recurrence of glioblastomas after surgery makes postoperative chemotherapy and XRT a crucial part of effective treatments. Although current treatment plans do often extend survival time, they are far from perfect and leave much room for improvement. However, while these efforts focus on optimal scheduling of radiotherapy, they do not include a similarly sophisticated spatial optimization.

Non-uniform dose distributions are not a new concept in radiation oncology. Phenotypic variations across the volume of a tumour can result in differing levels of radiation effectiveness. In particular, hypoxic regions cause a difference in cell radio-sensitivity, making radiation less effective in those areas. This leads to a technique called "dose-painting" in which different regions are prescribed a different dose to combat the reduced effect (see [2, 10] for an overview). Dose painting divides the tumour into a small, discrete number of regions allowing a different dose to be prescribed to each area. Additionally, we may need to apply non-uniform radiation to areas with different cell density, irrespective of radio-sensitivity.

Several previous works have addressed the dependence of the optimal beam shape on the density profile of the tumour, (see [13, 87, 95, 98] for example). A possible criterion for optimality (used in our calculation) is minimizing the total number (N) of tumour cells remaining after application of XRT; another is to maximize the Tumour Control Probability (TCP), e^{-N} (see below, Eq. (2.7)). Naturally either minimization must satisfy a number of physical constraints. The constraint on the total radiation dose (used in the paper) leads to a particular shape of the beam, which was also obtained in previous studies [13, 95, 98]. By contrast, a constraint on the mean dose, weighted by the local cell density, leads to a uniform beam profile [87].

In this paper, we study the following question: given a maximum allowable total dose to administer, what dose profile results in the maximum global TCP. As an equivalent metric to the TCP, we instead minimize the total number of surviving tumour cells after radiotherapy. We then go further, making our conclusions clinically reasonable by discretizing this optimal profile and considering multiple radiation fractions. While we do not deal with tumour heterogeneity in particular, we do include an alternative death mechanism

which can account for different radio-sensitivities resulting from tumour heterogeneity such as hypoxia. Other works have examined optimization of radiation therapy incorporating Normal Tissue Control Probability (NTCP) in addition to TCP [1, 2]. The NTCP is an important measure to consider as it quantifies the chance of problems arising in nearby organs at risk. While we do not include NTCP in this work, an interesting topic for future study would be to incorporate TCP and NTCP in a single mathematical optimization.

Naturally, when discussing optimization in a given system, mathematical modelling is an invaluable tool. In the context of brain tumours, mathematical models have been widely used by many different investigators (for example, [14, 36, 82, 92, 93]). While originally developed for investigations of brain tumours, we anticipate that these models and the following approach and results can be easily generalized to study other types of tumours. In the following, we build upon a host of previous works (see [68] for a review) which show that the natural growth of glioblastomas can be well-described by two governing parameters, ρ and D_n, which describe growth and invasion processes respectively. The two mathematical models most commonly used to describe growth of tumours are the so-called exponential and logistic growth laws. The more general logistic growth naturally provides a better description of tumour proliferation and stabilization. However, during the relatively short time frame before the growth of the tumour begins to plateau, exponential growth is a reasonable approximation. Including a linear (Laplacian) diffusion term, commonly used to model tumour invasion, we arrive at the well-established equation for tumour growth

$$\frac{\partial n(\vec{x},t)}{\partial t} = D_n \nabla^2 n(\vec{x},t) + \rho n(\vec{x},t)\Big(1 - \frac{a n(\vec{x},t)}{n_{max}}\Big). \tag{2.1}$$

Here, $n(\vec{x},t)$ is the tumour cell density at position $\vec{x} = (x_1, \cdots, x_d)$, and $\nabla^2 = \sum_{\alpha=1}^{d} \partial^2/\partial x_\alpha^2$ is the Laplacian operator. We have introduced d as the number of dimensions; $d = 3$ in three dimensions, while for certain computations we focus on the two dimensional case of $d = 2$. Exponential growth corresponds to $a = 0$, while $a = 1$ leads to logistic growth to a maximal density n_{max}.

Prior to treatment, two Magnetic Resonance Images (MRI) are commonly performed: one diagnostic and one to aid in treatment planning. Using the measures for velocity of growth and tumour abnormality obtained from these two scans alone, the tumour-specific values for ρ and D_n can be estimated [36].

We begin by presenting the general mathematical model, followed by studies of a number of special cases. First, the optimal continuous profile is derived for the cases of one and two radiative fractions with both exponential and logistic cytotoxic action. The insights from these cases are subsequently extended to show that the optimal tumour cell

density is uniform for any radiation procedure. From there, we move to optimization of non-continuous radiation profiles, and derive the optimal scenario for the cases of one-step and two-step profiles for single or multiple fractions, constrained individually or together. Finally, the non-continuous optimization is extended to include a logistic cytotoxic action for one and two step radiation profiles.

2.2 Materials and Methods

2.2.1 Model Derivation

Consider a tumour that has evolved according to Eq. (2.1) for some time, such that its cell density profile is given by $n(\vec{x}, t_0)$. Now we intend to apply XRT to this tumour. To do so, we introduce a function $f(\vec{x}, t)$ which we call the cytotoxic profile. The action of most therapeutic interventions is to remove a fraction of existing cells, which is incorporated in our model by adding a term $-\gamma f(\vec{x}, t)n(\vec{x}, t)(1 - bn(\vec{x}, t)/n_{max})$ to the right hand side of Eq. (2.1). For radiation, the parameter γ is a measure of the radiation rate, and can be written as $\gamma = \alpha\dot{D}$ (1/day) where α is the linear coefficient in the well-known Linear-Quadratic model ($S = e^{-\alpha D - \beta D^2}$) for radiation efficacy, and $\dot{D}$ is the dose rate applied to the tumour. For simplicity, we do not include the quadratic term of the Linear-Quadratic model into the model as it does not affect the qualitative shape of the radiation profile, which is the focus of this study. This is clear mathematically since the inclusion of the quadratic component simply perturbs the value of γ in Eq.(2.2) below, which acts as a scaling constant. The parameter b, much like a in the growth term, simply differentiates between exponential ($b = 0$) and logistic ($b = 1$) cell killing. It is also known that saturated tumours with a high cell-density and low proliferation are less affected by radiation than low cell-density tumours. A logistic death term is mathematically able to capture this behaviour as a higher cell density reduces the magnitude of the final term. This addition modifies the governing equation to

$$\frac{\partial n}{\partial t} = D_n \nabla^2 n + \rho n\Big(1 - \frac{an}{n_{max}}\Big) - \gamma f(\vec{x}, t)n\Big(1 - \frac{bn}{n_{max}}\Big). \tag{2.2}$$

Normal XRT occurs in a series of bursts called fractions. We therefore impose that $f(\vec{x}, t)$ is an on-again-off-again function in time such that $f(\vec{x}, t) = 0$ for all times except during the scheduled fractions. This greatly simplifies the solution to the nonlinear partial differential equation, as during the time interval Δt over which each fraction is applied, the processes of cell division and spreading have little effect on the cell density. The natural growth of

tumours proceeds on scales of days, months, or years, while radiation fractions occur over a scale of minutes. Thus, during each fraction, the first two terms on the right hand side of Eq. (2.2) can be mathematically neglected, leading to

$$\left.\frac{\partial n}{\partial t}\right|_{fraction} \approx -\gamma f(\vec{x},t)n\Big(1-\frac{bn}{n_{max}}\Big). \tag{2.3}$$

Integrating this (now ordinary) differential equation in the interval $t \in [t_0, t_0+\Delta t]$, leads to

$$n(\vec{x},t_0+\Delta t) = n(\vec{x},t_0)e^{-\gamma f(\vec{x},t_0)\Delta t}, \tag{2.4}$$

in the exponential case ($b=0$), and

$$n(\vec{x},t_0+\Delta t) = \frac{n_{max}}{1-\left(\frac{n(\vec{x},t_0)-n_{max}}{n(\vec{x},t_0)}\right)e^{-\gamma f(\vec{x},t_0)\Delta t}}, \tag{2.5}$$

in the logistic case ($b=1$). We focus on the first and second fractions of XRT and further impose a simple upper bound for $f(\vec{x},t)$ to adhere to patient safety standards. We write this constraint as $0 \le f(\vec{x},t) \le C$ for some C. The final constraint on $f(\vec{x},t)$ limits the total dose received by the patient. This constraint is mathematically represented by

$$\gamma \int d^d\vec{x}\ dt\ f(\vec{x},t) \le F\ , \tag{2.6}$$

where the time integral is over the entire treatment length. This constrains the total radiation dose over all fractions (where we expect the inequalities to be saturated to achieve maximal effectiveness).

Our goal is to determine the function $f(\vec{x},t)$ that minimizes the total number of tumour cells after the final fraction, $N(T)$, obtained by integrating the tumour cell density as

$$N(T) = \int d^d\vec{x}\ n(\vec{x},T). \tag{2.7}$$

To contrast, Brahme and Agren [13] instead optimized the TCP, which they defined as (using our notation) TCP $= e^{-N(T)}$ where $N(T)$ is the number of cells surviving the treatment. Regarding $n(\vec{x},t_0+\Delta t)$ as the mean of a probability density for cells following XRT, TCP is the probability that all cells are exterminated. Clearly, one can see that minimizing $N(T)$ is equivalent to maximizing $e^{-N(T)}$. Furthermore, for the simplest case, we indeed achieve the same result.

2.3 Results

2.3.1 Continuous Profile Optimization

We begin by analysing continuous cytotoxic profiles for one fraction of radiation. In the case of exponential death, the result matches that of previous studies, and from it we can derive a precise shape of the profile. In the case of logistic death, the resulting profile is more complex, but remains mathematically consistent with the previous case. A similar analysis of the second fraction of radiation is significantly more challenging as the effect of normal tumour progression must be taken into account. While it is possible, the results are far less interesting since the optimal profile will leave a uniform (or flat-topped) cell density (proof of this in appendix A.1) . The second fraction is mathematically examined in the appendix A.2 for the case of exponential death.

Optimal Profile with one Fraction of Exponential Death

To proceed in the case of exponential cytotoxic action, we impose the first constraint in Eq. (2.6) with a Lagrange multiplier λ, which requires extremizing

$$\tilde{N}_1 = \int d^d\vec{x}\; n(\vec{x},t_0)e^{-f(\vec{x},t_0)} + \lambda\Big(\int d^d\vec{x}\; f(\vec{x},t_0) - F\Big), \tag{2.8}$$

where we have set $\gamma = \Delta t = 1$ for convenience. Solving the resulting Euler-Lagrange equation for $f(\vec{x},t_0)$, we find the optimal profile

$$f(\vec{x},t_0) = \ln\left[\frac{n(\vec{x},t_0)}{\lambda}\right], \tag{2.9}$$

with λ chosen such that Eq. (2.6) is satisfied. Using this cytotoxic profile would give us the optimal cell kill from the radiation fraction. Not surprisingly, following the simplifications leading to Eq. (2.9), the above result is independent of the parameters ρ and D_n. The appearance of the logarithm is merely a consequence of the killing effect of therapy being proportional to the number of existing cells, with the cytotoxic profile appearing in the exponent of Eq. (2.4).

This result has been previously derived by many others ([13, 87, 95] for example). An interesting consequence of this optimal profile is that it leaves the resulting cell density as a uniform distribution. Stavreva *et al* [87] applied an extremization of TCP subject to a constraint on the mean dose defined as $D_v \propto \int n(\vec{x},t_0)f(\vec{x},t_0)d^dx$, i.e. weighting the dose

according to the local cell density. It is clear that if this constraint is used in Eq. (2.8) in place of the unweighted net dose, the resulting beam profile will be uniform.

While a useful starting point, the cytotoxic profile in Eq. (2.9) is not guaranteed to satisfy the constraints of $0 \leq f(\vec{x}, t) \leq C$. In particular, it leads to unphysical negative values when $n(\vec{x}, t_0) < \lambda$. To better understand the limitations of this result, and how to overcome them, let us consider the simplest case of a Gaussian profile arising from radially symmetric growth of a single cell in exponential growth: assuming that the tumour begins with a single oncogenic transformation or single-cell metastasis, modelled by a delta-function cell density, exponential growth for a time t_0 leads to the cell density profile

$$n(r, t_0) = n_0 e^{-\frac{r^2}{2\sigma^2}}, \tag{2.10}$$

where r is the radial distance from the initial cell (tumour center). The width of the Gaussian profile is $\sigma = \sqrt{2D_n t_0}$, while $n_0 = e^{\rho t_0}/(2\pi\sigma^2)^{d/2}$ is the cell density at its center. Equation (2.9) now leads to a parabolic cytotoxic profile. Cutting off the negative portions of the parabola leads to the (semi-circular) profile

$$f(\vec{x}, t_0) \equiv f_1(r) = \ln\left(\frac{n_0}{\lambda}\right) - \frac{r^2}{2\sigma^2} \equiv \begin{cases} f_m\left(1 - \frac{r^2}{r_m^2}\right) & \text{if} \quad r \leq r_m \\ 0 & \text{if} \quad r \geq r_m \end{cases}. \tag{2.11}$$

We have introduced the parameters $f_m = \ln(n_0/\lambda)$ and $r_m = \sigma\sqrt{2f_m}$ to indicate the maximum value of the cytotoxic profile, and the radius over which it is applied, respectively. The total radiation dose in this fraction is then given by

$$F = \int d^d\vec{x}\ f_1(r) = \frac{2S_d}{d(d+2)} f_m r_m^d, \tag{2.12}$$

where S_d is the d-dimensional solid angle, with $S_3 = 4\pi$ and $S_2 = 2\pi$. Using $f_m = r_m^2/(2\sigma^2)$ from Eq. (2.11), we conclude that the optimal radius of the semi-circular beam is given by

$$r_m = \left(\frac{d(d+2)}{S_d}\right)^{\frac{1}{d+2}} F^{\frac{1}{d+2}} \sigma^{\frac{2}{d+2}}, \tag{2.13}$$

while its maximal intensity equals

$$f_m = \frac{1}{2}\left(\frac{d(d+2)}{S_d}\right)^{\frac{2}{d+2}} F^{\frac{2}{d+2}} \sigma^{-\frac{2(d+1)}{d+2}}. \tag{2.14}$$

If the above value of f_m exceeds the maximum allowed intensity of C, we should instead use

$$f_1^C(r) = \begin{cases} C - \frac{r^2}{2\sigma^2} & \text{if} \quad r \leq r_m \\ 0 & \text{if} \quad r \geq r_m \end{cases}, \tag{2.15}$$

with $r_m(F)$ now constrained by the maximal allowed density according to Eq. (2.12). In either case, the cell density profile after application of XRT will attain a flat-top profile, as

$$n(r, t_0 + \Delta t) = \begin{cases} n_0 e^{-f_m} & \text{if} \quad r \leq r_m \\ n(r, t_0) & \text{if} \quad r \geq r_m \end{cases}. \tag{2.16}$$

A flat post-XRT profile is also predicted for any initial tumour cell density $n(\vec{x}, t_0)$, although the volume over which the beam is applied will be different. In the best outcome, the density profile will be below the (single-cell) threshold for future growth. If not, additional fractions need to be applied.

Optimal Profile with One Fraction of Logistic Death

Mathematically, the switch from an exponential to a logistic cell death does not change much. We now simply use Eq. (2.5) instead of Eq. (2.4) in our optimization. Again imposing the constraint of Eq. (2.6) using a Lagrange multiplier and setting $\gamma = \Delta t = 1$ for convenience, we arrive at the optimal profile

$$f(\vec{x}, t_0) = \ln\left[\left(\frac{n_{max} - n(\vec{x}, t_0)}{n(\vec{x}, t_0)}\right)\left(\frac{2\lambda}{2\lambda + n_{max} + \sqrt{n_{max}(n_{max} + 4\lambda)}}\right)\right]. \tag{2.17}$$

Like the previous single-fraction case, this result is independent of ρ and D_n. It also is not guaranteed to satisfy the bounds of $0 \leq f(\vec{x}, t) \leq C$. As a quick check on the validity of this result, one can let $n_{max} \to \infty$ and see that Eq. (2.9) is recovered. Note that the optimal profile again has a uniform or flat-topped form. This can be seen by substituting Eq. (2.17) into Eq. (2.5).

2.3.2 Discrete Profile Optimization

Computational methods exist for determining how to administer a heterogeneous dose, primarily *sub-volume boosting* and *dose painting by numbers* [2, 10]. Unfortunately, these methods are limited by the mathematical optimization techniques as well as the physical

reasonability of their results. Specifically, current technology is not capable of producing beams with a high degree of precision for clinical use such as those derived above in the continuous profile optimization. The standard procedure is to coalesce several beams on the location of the tumour, creating an area of high radiative strength. As such, a reasonably practical non-uniform beam profile is a step function. In the following, we consider cases of both one-step and two-step radiation profiles. We emphasize that our aim is to explore the feasibility of spatial optimization and to gain qualitative insights, and thus make mathematical simplifications throughout to reflect this. The first simplification is to consider *radially symmetric profiles in two dimensions*. In the following, we assume exponential growth ($a = 0$) leading to a Gaussian profile, as in Eq. (2.10). A summary of the parameter values used in calculations can be seen in Table 2.1.

D1: One-Step Radial Profile

The simplest step-function case of XRT involves a uniform beam of radius r_1 and strength f_1, applied for a duration Δt at time t_0, i.e.

$$f(r,t) = \begin{cases} f_1 & 0 \le r \le r_1 \text{ and } t_0 \le t \le t_0 + \Delta t, \\ 0 & \text{otherwise.} \end{cases} \tag{2.18}$$

The goal is minimize $N(t_0 + \Delta t) = 2\pi \int r\ n(r, t_0 + \Delta t)\ dr$, subject to a constraint on F which we rewrite as a constraint on $F' \equiv \frac{F}{\pi \Delta t \gamma} = r_1^2 f_1$. Approximating the Partial Differential Equation (PDE) as an Ordinary Differential Equation (ODE) as before, the tumour cell density distribution immediately after the fraction is obtained as

$$n(r, t_0 + \Delta t) = \begin{cases} n(r,t_0)e^{-\gamma f_1 \Delta t} & 0 \le r \le r_1, \\ n(r,t_0) & r_1 < r \le R. \end{cases} \tag{2.19}$$

Integrating this result gives the total number of cells as

$$\begin{aligned} N(t_0 + \Delta t) &= \iint n(r, t_0 + \Delta t) dA \\ &= 2\pi \left[e^{-\gamma f_1 \Delta t} n_0 \int_0^{r_1} r e^{-\frac{r^2}{2\sigma^2}} dr + n_0 \int_{r_1}^{R} r e^{-\frac{r^2}{2\sigma^2}} dr \right] \\ &= 2\pi n_0 \sigma^2 \left[e^{-\gamma f_1 \Delta t} \left(1 - e^{-\frac{r_1^2}{2\sigma^2}} \right) + e^{-\frac{r_1^2}{2\sigma^2}} - e^{-\frac{R^2}{2\sigma^2}} \right]. \end{aligned} \tag{2.20}$$

The constraint on the total beam flux can be imposed through a Lagrange multiplier λ to create an augmented N,

$$\tilde{N} = 2\pi n_0 \sigma^2 \Big[e^{-\gamma f_1 \Delta t} \Big(1 - e^{-\frac{r_1^2}{2\sigma^2}} \Big) + e^{-\frac{r_1^2}{2\sigma^2}} - e^{-\frac{R^2}{2\sigma^2}} \Big] - \lambda (f_1 r_1^2 - F') \ . \tag{2.21}$$

Extremizing with respect to r_1, f_1, and λ leads to the following system of equations:

$$0 = 2\pi n_0 r_1 \Big[e^{-\frac{r_1^2}{2\sigma^2} - \gamma f_1 \Delta t} - e^{-\frac{r_1^2}{2\sigma^2}} \Big] - 2\lambda f_1 r_1, \tag{2.22}$$

$$0 = 2\pi n_0 \sigma^2 \Big[-\gamma \Delta t e^{-\gamma f_1 \Delta t} + \gamma \Delta t e^{-\frac{r_1^2}{2\sigma^2} - \gamma f_1 \Delta t} \Big] - \lambda r_1^2, \tag{2.23}$$

$$0 = f_1 r_1^2 - F'. \tag{2.24}$$

After eliminating f_1 and λ from the above equations, we arrive at the following implicit expression for r_1:

$$0 = e^{-\frac{F' \gamma \Delta t}{r_1^2}} + \Big(\frac{r_1^4}{2F' \gamma \Delta t \sigma^2} - 1 \Big) e^{-\frac{r_1^2}{2\sigma^2} - \frac{F' \gamma \Delta t}{r_1^2}} - \frac{r_1^4}{2F' \gamma \Delta t \sigma^2} e^{-\frac{r_1^2}{2\sigma^2}}. \tag{2.25}$$

Values of r_1 that satisfy Eq. (2.25) can be used to find a corresponding f_1, together specifying the optimal $N(r_1, f_1)$. We assume that the duration of radiation is approximately 10 minutes, or $\Delta t = 0.007$ (days), and use the linear model for the radiation $\gamma = \alpha \dot{D}$, where α is the radiobiological parameter and $\dot{D}$ is the dose rate. For $\alpha = 0.08$ (1/Gy) (taken from an average of the values obtained in [82]) and the standard dose rate of 5 (Gy per radiation time), we obtain $\gamma = 60$ (1/day). Using the parameter values $C = 2.5$ (corresponding to the maximum allowed dose rate of 5 (Gy per radiation time)), $F' = 25$ (mm^2), and a range of (n_0, σ) pairs chosen such that $N(t = t_0) = 10^7$ (cells) is constant, we can solve for r_1 and calculate the corresponding f_1. The location of the optimal radius r_1 is plotted in Fig. 2.1. As expected, larger values of σ require radiation over a wider radius. However, the increase of r_1 with σ is sub-linear, and quite well fitted by $r_1 \propto \sigma^{1/2}$. This is precisely the scaling behavior predicted in Eq. (2.13) for the semi-circular beam shape in $d = 2$. The scaling of the optimal radius with tumour size thus appears to be robust, irrespective of the beam shape. This procedure is done for 5 different (n_0, σ) pairs in Table 2.2 and the profiles can be seen in Fig. A.2 (appendix). Note that for the $\sigma = 1$ and $\sigma = 2$ cases, the optimal r_1 falls below $\sqrt{10}$ (mm). However, due to our constraints of $F' = 25 = f_1 r_1^2$ and $0 \leq f(r,t) \leq C = 2.5$, we have a lower bound of $r_1 \geq \sqrt{10}$ (mm). Also note that the calculated values in Table 2.2, and in the following data tables, are truncated decimals, but the values of N are calculated using more precise solutions. Therefore, inserting the values for r_1 and f_1 found from Table 2.2 into Eq. (2.20) will not necessarily exactly reproduce the listed values of N.

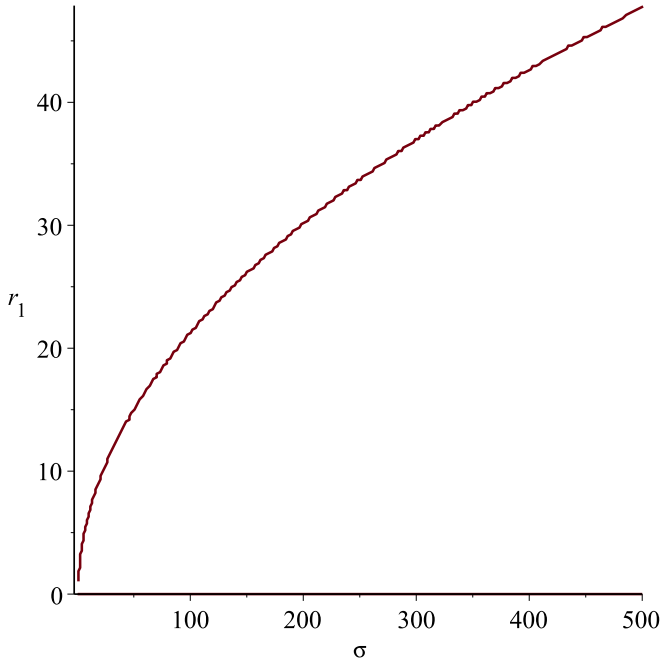

Figure 2.1: Optimal beam radius r_1 vs. tumour size σ from Eq. (2.25).

Parameter	Symbol	Value (Unit)	Reference
Initial Total Cell Number	N	10^7 (cells)	Chosen
Tumour Cell Diffusivity	D_n	0.32 (mm^2/day)	[51]
Tumour Cell Proliferation Rate	ρ	0.35 (1/day)	[51]
Linear-Quadratic Parameter	α	0.08 (1/Gy)	Average of values from [82]
Dose Rate during Radiation	$\dot{D}$	5 (Gy/fraction)	Chosen within range from [81]
Radiation Effect Parameter	γ	60 (1/day)	Estimated from α and $\dot{D}$
Dose Limiting Parameter	C	2.50 (Gy)	Chosen

Table 2.1: Model parameters used in the various calculations and simulations throughout the paper. Those with the given reference of 'Chosen' were selected within a biologically reasonable range from various sources as an example for calculations.

σ (mm)	n_0	r_1 (mm)	f_1	$N(t+dt)$
1	1.59e6	$\sqrt{10}$	2.50	3.54e6
2	3.98e5	$\sqrt{10}$	2.50	5.36e6
3	1.78e5	3.71	1.82	7.16e6
4	1.04e5	4.28	1.36	8.01e6
5	7.36e4	4.79	1.09	8.43e6

Table 2.2: Optimal one-step profile for one fraction of radiation with exponential growth and death. n_0 and σ are the magnitude and standard deviation of the initial Gaussian tumour cell density, which starts with 10^7 total cells. r_1 and f_1 are the radius and strength of the step in the cytotoxic radiation profile. $N(t+dt)$ is the final tumour cell number at the end of radiation.

D2: Two-Step Radial Profile

Now we consider the more elaborate example of a 2-step cytotoxic profile, but still applied in only one fraction. Introducing two new variables, r_2 and f_2, the radiation profile is:

$$f(r, t_0 \leq t \leq t_0 + \Delta t) = \begin{cases} f_1 & 0 \leq r \leq r_1, \\ f_2 & r_1 < r \leq r_2, \\ 0 & r_2 < r \leq R. \end{cases} \tag{2.26}$$

where f_2 applies a different dosage to the outer region of the tumour. Adding the second radial arc modifies the constraint on dosage to

$$F' = \frac{F_1}{dt} = f_1 r_1^2 + f_2(r_2^2 - r_1^2). \tag{2.27}$$

We need to minimize the total cell number, N, with respect to the four-parameter set $(r_1,\ r_2,\ f_1,\ f_2)$. Using the Lagrange multiplier method as above results in a system of 5 coupled transcendental equations. Unfortunately, this set of equations has many local extrema, making the result heavily dependant on the initial guess used in the computational solver. This makes identification of the global extreme difficult. To avoid this, we use a Monte Carlo method to identify the optimal shape of the radiation beam. First, a random

σ (mm)	r_1 (mm)	r_2 (mm)	f_1	f_2	$N(t+dt)$
1	3.06	3.27	2.50	1.18	3.54e6
2	2.81	3.47	2.50	1.27	5.30e6
3	2.81	3.98	2.10	1.06	7.10e6
4	3.26	4.61	1.57	0.78	7.98e6
5	3.64	5.15	1.26	0.64	8.41e6

Table 2.3: Optimal two-step profile for one fraction of radiation with exponential growth and death. σ is the standard deviation of the initial Gaussian tumour cell density, which starts with 10^7 total cells. r_1, r_2, f_1 and f_2 are the two radii and strengths of the steps in the cytotoxic radiation profile. $N(t+dt)$ is the final tumour cell number at the end of radiation.

radiation beam is generated by selecting a point from the parameter space (r_1, r_2, f_1, f_2). The selection of this point is made by randomly assigning values to 3 of the parameters within their acceptable ranges, then calculating the fourth according to Eq. (2.27) such that the dose constraint is satisfied. This generated parameter set defines the candidate radiation beam. The total cell number resulting from each beam is calculated and compared to the previous minimum. This is done many times ($\sim 10^9$ in our simulations) such that N converges to a global minimum. The point in the parameter space which generates this minimum is then inserted back into the equations for the optimal profile to check that they are indeed satisfied. Such a point parameterizes the optimal profile (in subsequent optimizations the parameter space will become more complex, however this method will remain the same). The numerical values resulting from this method are summarized in Table 2.3, and the resulting cell density profiles are shown in Fig. A.3 (Supporting Information). As a check on the numerical optimization, we do find that the the addition of the second radial arc leads to better treatment outcomes. Once the constraint on maximal value of $f_1 = 2.5$ is no longer operative (for $\sigma > 2$ mm), the resulting cell density profiles are close approximations to the flat-top profiles expected from a semi-circular beam. The optimal two step radial profile thus represents a crude approximation to the semi-circular beam.

D3: Two Fractions Individually Constrained

We next consider application of a second fraction of radiation, with dosage separately constrained on each fraction. Describing the second fraction requires introducing four new

variables to fully parametrize $f(r,t)$. We modify the previous notation by adding a second index to each of the radii and strengths of $f(r,t)$, with the first index indicating the step-number and the second corresponding to the fraction number. Thus, r_1, r_2, f_1, and f_2 from before become r_{11}, r_{21}, f_{11}, and f_{21} respectively, with corresponding r_{12}, r_{22}, f_{12}, and f_{22} for the second fraction. The interval between the two fractions will be labelled τ, such that the second fraction takes place over the interval $[t_0+\Delta t+\tau, t_0+2\Delta t+\tau]$. Note that we assume the lengths of the two fractions to be the same. Defining $t_0^* \in [t_0, t_0+\Delta t]$ and $t_1^* \in [t_0+\Delta t+\tau, t_0+2\Delta t+\tau]$, we can write $f(r,t)$ during the separate fractions as

$$f(r,t_0^*) = \begin{cases} f_{11} & 0 \le r \le r_{11} \\ f_{21} & r_{11} < r \le r_{21} \\ 0 & r_{21} < r \le R \end{cases}, \qquad \text{and} \qquad f(r,t_1^*) = \begin{cases} f_{12} & 0 \le r \le r_{12} \\ f_{22} & r_{12} < r \le r_{22} \\ 0 & r_{22} < r \le R \end{cases}. \tag{2.28}$$

In this section, we consider the fractions constrained individually, such that

$$F' = f_{11}r_{11}^2 + f_{21}(r_{21}^2 - r_{11}^2), \qquad \text{and} \qquad F' = f_{12}r_{12}^2 + f_{22}(r_{22}^2 - r_{12}^2). \tag{2.29}$$

Since our constraint on $f(r,t_0^*)$ is the same as before, the optimal $f(r,t_0^*)$ does not change from that in Table 2.2. We can use the same optimization procedure for the second fraction, but with a modified starting cell density profile. In order to deal with profiles with simple analytic expression, we further assume that the time interval τ between the fractions is small enough to neglect spatial migrations described by the diffusion term (mathematically, this can be expressed as the condition $D_n\tau \ll \sigma^2$, which can be derived from a simple scale analysis). If so, the density profile simply grows exponentially, by a factor $e^{\rho\tau}$ without changing its spatial form, and immediately before the second fraction is given by

$$n(r, t_0+dt+\tau) = \begin{cases} n_0 e^{\rho\tau} e^{-\frac{r^2}{2\sigma^2}} e^{-\gamma f_{11}\Delta t} & 0 \le r \le r_{11} \\ n_0 e^{\rho\tau} e^{-\frac{r^2}{2\sigma^2}} e^{-\gamma f_{21}\Delta t} & r_{11} < r \le r_{21} \\ n_0 e^{\rho\tau} e^{-\frac{r^2}{2\sigma^2}} & r_{21} < r \le R \end{cases}.$$

The density profile immediately after application of the second fraction is then given by:

$$n(r, t_0+2dt+\tau) = \begin{cases} n(r, t_0+dt+\tau) e^{-\gamma f_{12}\Delta t} & 0 \le r \le r_{12} \\ n(r, t_0+dt+\tau) e^{-\gamma f_{22}\Delta t} & r_{12} < r \le r_{22} \\ n(r, t_0+dt+\tau) & r_{22} < r \le R \end{cases}.$$

For each set of radii, r_{11}, r_{21}, r_{12}, and r_{22}, the cell density is a piecewise continuous function. The total number N can then be obtained as before by integration, as an explicit

$\sigma(mm)$	$r_{11}(mm)$	$r_{21}(mm)$	f_{11}	f_{21}	$r_{12}(mm)$	$r_{22}(mm)$	f_{12}	f_{22}	$N(T)$
1	3.06	3.27	2.50	1.18	2.93	3.36	2.50	1.30	1.29e6
2	2.81	3.47	2.50	1.27	1.97	4.04	2.42	1.26	3.41e6
3	2.81	3.98	2.10	1.06	4.61	5.03	1.07	0.57	5.59e6
4	3.26	4.61	1.57	0.78	5.36	5.84	0.80	0.39	6.80e6
5	3.64	5.15	1.26	0.64	5.98	6.54	0.64	0.31	7.52e6

Table 2.4: Optimal two-step profile for two separately constrained fractions of radiation with exponential growth and death. σ is the standard deviation of the initial Gaussian tumour cell density, which starts with 10^7 total cells. $r_{11}, r_{21}, r_{12}, r_{22}, f_{11}, f_{21}, f_{12}$ and f_{22} are the radii and strengths of the steps in the cytotoxic radiation profiles. $N(t+dt)$ is the final tumour cell number at the end of radiation.

analytic expression. For the same initial combinations of (n_0, σ) as above, we search for the radii (r_{12}, r_{22}) that optimize the second fraction using our Monte Carlo method (the optimal radii (r_{11}, r_{21}) are naturally the same as obtained previously in Table 2.3). The results of this minimization are summarized in Table 2.4.

Note that if diffusion is ignored, the final cell density after a second fraction of radiation is given by $n(\vec{x}) = n_0(\vec{x}) \exp\{\rho\tau - \gamma[f_1(\vec{x}) + f_2(\vec{x})]\Delta t\}$. From this expression it follows that in this limit, the order in which the two fractions are applied is not important. Indeed the same conclusion applies to any number of fractions, each separately optimized. Thus it is not necessary to use the XRT profile that is optimal at the time of its application, as long as there are planned future fractions that boost the overall amount of radiation at each point to the optimal value. This freedom provides an additional tool for therapeutic planning.

D4: Two Fractions with Overall Constraint

As a final example within this class, with non-diffusive exponential growth between the two fractions, we consider the case when the overall dose is constrained, i.e. as

$$2F' = f_{11}r_{11}^2 + f_{21}(r_{21}^2 - r_{11}^2) + f_{12}r_{12}^2 + f_{22}(r_{22}^2 - r_{12}^2).$$

The optimization procedure can be carried out as before through a Monte Carlo search. However, each step of the search now involves an exploration in the space of 8 variables (as opposed to separate searches in a space of 4 variables), subject to one constraint. Note

σ (mm)	r_{11} (mm)	r_{21} (mm)	f_{11}	f_{21}	r_{12} (mm)	r_{22} (mm)	f_{12}	f_{22}	$N(T)$
1	3.06	3.27	2.50	1.18	2.93	3.36	2.50	1.30	1.29e6
2	2.81	3.47	2.50	1.27	1.97	4.04	2.42	1.26	3.41e6
3	3.55	4.92	1.63	0.82	2.56	4.31	1.61	0.78	5.59e6
4	4.20	5.74	1.21	0.61	2.97	4.92	1.22	0.55	6.79e6
5	4.63	6.34	1.02	0.50	3.28	5.52	0.96	0.43	7.42e6

Table 2.5: Optimal two-step profile for two mutually constrained fractions of radiation with exponential growth and death. σ is the standard deviation of the initial Gaussian tumour cell density, which starts with 10^7 total cells. $r_{11}, r_{21}, r_{12}, r_{22}, f_{11}, f_{21}, f_{12}$ and f_{22} are the radii and strengths of the steps in the cytotoxic radiation profiles. $N(t+dt)$ is the final tumour cell number at the end of radiation.

also that (except for the replacement of $2F'$ for F') this is exactly the search that would be performed for a single fraction with a 4-step profile. The optimal values of these parameters are given in Table 2.5.

Observe that for each σ, the optimal N with the single overall constraint is either better, or the same as, in the individually constrained case. From the perspective of optimization, this is not unexpected as the latter also explores the subset of the space available to the former. In view of this, the surprising result may appear to be that for $\sigma = 1$ and 2 (see Table 2.6) the minimum occurs in the separately constrained space. However, the structure of the general optimization problem is such that for $D_n = 0$, the same result should hold with one or more constraints (appendix). We are thus unable to conclude if the unequal partition of flux between the two fractions (in cases of $\sigma = 3$, 4, 5) is correct or a computational artifact (we indeed find many solutions close to the optimum, so finding the true optimum requires considerable computation and precision).

D5: Tumour Densities from Logistic Growth

The Gaussian density profiles employed to model the initial cell densities above are appropriate only for small undeveloped tumours. For contrast, in this section we consider density profiles resulting from the logistic growth ($a = 1$ in Eq. (2.1)). Such profiles are obtained by evolving the partial differential equation

$$\frac{\partial n}{\partial t} = D_n \nabla^2 n + \rho n(1 - \frac{n}{n_{max}}), \tag{2.30}$$

σ (mm)	1st Fraction	2nd Fraction
1	25.00	25.00
2	25.00	25.00
3	30.08	19.92
4	30.77	19.23
5	31.27	18.73

Table 2.6: Distribution of radiation flux over two radiation fractions based on standard deviation of initial tumour cell density. The '1st Fraction' number represents the amount of dose (out of 50) that is allocated to the 1st radiation fraction and the '2nd fraction' the amount allocated to the 2nd radiation fraction.

σ	a_1	b_1	c_1
1	2.0697e6	0.4237	0.04007
3	1.0978e6	-0.3069	-0.004395
5	1553387	-0.02081	-0.01505

Table 2.7: Fitting parameters for initial density generated by simulation with logistic growth. Parameters correspond to those in Eq. (2.31).

starting with a localized initial condition. While there is no exact analytic form for the resulting solution, as an analytical approximant, we use the form

$$n(r, t_0) = \frac{a_1}{1 + b_1\, e^{c_1\, r^2}}, \tag{2.31}$$

where a_1, b_1, and c_1 are fit parameters. Logistic growth causes the tumour to form a flat-top profile as the density in the centre approaches n_{max}. Equation (2.31), which is known as a Fermi Function, also describes a flat-top form, which is why we use it for fitting. A numerical implementation of Eq. (2.1) was used to generate the fit parameters. For this procedure and more information, see supporting information. The values of the fitted parameters are given in Table 2.7.

We consider the same radial step-functions as previous, and the optimization procedures are carried out in the same manner as before. The results for application of a single 2-step fraction are reported in Table 2.8 and the resulting profiles can be seen in Fig. A.6. If this treatment is followed by a second, separately constrained 2-step fraction, the resulting

σ	r_1 (mm)	r_2 (mm)	f_1	f_2
1	3.89	5.23	1.16	0.61
3	6.73	10.00	0.34	0.17
5	5.80	10.00	0.26	0.24

Table 2.8: Optimal one-step profile for one fraction of radiation with logistic growth and exponential death. σ is the standard deviation of the initial Gaussian tumour cell density, which starts with 10^7 total cells. r_1, r_2, f_1, and f_2 are the radii and strengths of the steps in the cytotoxic radiation profiles. $N(t+dt)$ is the final tumour cell number at the end of radiation.

σ	r_{11}	r_{21}	f_{11}	f_{21}	r_{12}	r_{22}	f_{12}	f_{22}
1	3.89	5.23	1.16	0.61	5.92	6.37	0.66	0.33
3	6.73	10.00	0.34	0.17	3.98	10.00	0.31	0.24
5	5.81	10.00	0.26	0.24	8.47	10.00	0.25	0.25

Table 2.9: Optimal two-step profile for two separately constrained fractions of radiation with logistic growth and exponential death. σ is the standard deviation of the initial Gaussian tumour cell density, which starts with 10^7 total cells. $r_{11}, r_{21}, r_{12}, r_{22}, f_{11}, f_{21}, f_{12}$ and f_{22} are the radii and strengths of the steps in the cytotoxic radiation profiles. $N(t+dt)$ is the final tumour cell number at the end of radiation.

parameters for the second application are given in Table 2.9 and the resulting profiles can be seen in Fig. A.7.

D6: Tumour Densities from Logistic Growth and Logistic Death

The previously examined cases of exponential cytotoxic action do not incorporate the phenomenon of radiation having a larger effect on faster-proliferating cells than on slower-proliferating cells due to the cell's position in the cell cycle and factors such as oxygen concentration [48]. If we instead consider logistic action ($b = 1$), then some aspects of such tendency are reproduced. This qualitative behavior is important to incorporate because the vast majority of tumours exhibit some form of treatment resistance. This resistance is conferred to a tumour through heterogeneities of various traits across its volume, such as cell-type, phenotypic expression, and stem-ness. Of particular interest to radiation therapy, tumour hypoxia is a prominent feature that leads to increased radioresistance. As

σ	r_1	r_2	f_1	f_2
1	4.3933	5.7914	0.0000	1.7557
3	9.4731	9.9886	0.0005	2.4875
5	9.4774	9.9906	0.0009	2.4940

Table 2.10: Optimal two-step profile for one fraction of radiation with logistic growth and death. σ is the standard deviation of the initial Gaussian tumour cell density, which starts with 10^7 total cells. r_1, r_2, f_1, and f_2 are the radii and strengths of the steps in the cytotoxic radiation profiles. $N(t+dt)$ is the final tumour cell number at the end of radiation.

we will see, inclusion of logistic cytotoxic action reproduces this behavior and dramatically changes the results. We note that this is a purely phenomenological effect and not meant to describe the underlying biology at play. We make the same simplifications as before leading to the piecewise equivalent to Eq. (2.5),

$$n(r, t_0+\Delta t) = \begin{cases} \frac{a_1 n_{max} e^{-\gamma f_1 \Delta t}}{a_1(e^{-\gamma f_1 \Delta t}-1)+n_{max}(1+b_1 e^{c_1 r^2})} & 0 \le r \le r_1 \\ \frac{a_1 n_{max} e^{-\gamma f_2 \Delta t}}{a_1(e^{-\gamma f_2 \Delta t}-1)+n_{max}(1+b_1 e^{c_1 r^2})} & r_1 < r \le r_2 \\ \frac{a_1}{1+b_1 e^{c_1 r^2}} & r_2 < r \le R. \end{cases}$$

The results of the Monte Carlo optimization are summarized in Table 2.10 and the resulting profiles can be seen in Fig. A.8.

Mathematically, the results here differ dramatically from the exponential case in which the optimal profile focused the radiative strength in the center of the tumour where the cell-density was larger. With the incorporation of logistic cell death, the effectiveness of radiation in the center of the tumour diminishes. The optimal profile must now balance this with still attacking areas with high cell densities. We see that in the case with the smallest initial spread of cells, the optimal cytotoxic profile achieves this by focusing strength in a ring through the middle of the tumour. For the other two cases, the density was far more spread out initially, leading to an optimal profile which focused on cells at the outside of the tumour. This was because the effect of the logistic death was stronger than the decreased cell density.

In the case of exponential death, we were able to continue our discussion and optimize the second fraction as we did the first. In the logistic death case, the computations in the optimization method become significantly more challenging. For that reason, we do not

Subsection	Dose Profile	# Fractions	Constraint	Growth	Death	Optimization
D1	One-Step	1	F_1	Exp	Exp	Lagrange Multiplier
D2	Two-Step	1	F_1	Exp	Exp	Monte Carlo
D3	Two-Step	2	F_1 and F_2	Exp	Exp	Monte Carlo
D4	Two-Step	2	$F_1 + F_2$	Exp	Exp	Monte Carlo
D5	Two-Step	1	F_1	Log	Exp	Monte Carlo
D6	Two-Step	1	F_1	Log	Log	Monte Carlo

Table 2.11: Overview of Cases for Spatial Optimization of Radiation Therapy.

pursue the second fraction of radiation here.

2.4 Conclusion and Discussion

In this paper we pose the question of how to spatially shape a sequence of XRT treatments to best eliminate tumour cells. To answer this question, we need to know **(i)** how the tumour grows in time; **(ii)** how it responds to treatment; and **(iii)** what constraints apply to radiation dosage. Answers to all questions need to be expressed in mathematical terms, which necessitates simplifications and approximations. We have relied on assumptions and mathematical models commonly used in the literature, and hope our general results are insensitive to choice of model.

The most important result follows from the assumption that the effect of XRT is to destroy a fraction of existing tumour cells, proportional to its strength. This assumption is embodied by the term $-\gamma f(\vec{x},t)n(1-bn/n_{max})$ in Eq. (2.2). It immediately leads to the conclusion that the optimal beam profile should depend non-uniformly on the tumour density at the time of its application. Shaping the beam to such a precise form is likely impossible, and may further violate constraints on the strength of the beam. As such, optimal beam profiles can be sought within certain constraints on the shape of the beam. In particular, we consider XRT profiles obtained by superposing several radially symmetric beams. Clinically, the normal procedure is to irradiate the entire radius of the visible tumour with a uniform beam. As can be seen from the various tables above, a uniform $f(r,t)$ will not lead to optimal cell kill. Using a spatially optimized $f(r,t)$ can reduce the total number of cells within a tumour significantly from what is currently done clinically.

The metric of TCP is not the only quantity that can be used to measure radiation

efficacy. Others such as NTCP, conformity index, homogeneity index, and survival time have been used by other researchers [3, 24, 29, 107]. We focused our analysis here on TCP as it is intuitively simple and mathematically straightforward. We stress that this is an exploratory study meant to discern qualitative behaviour, and note that a more complete study should include analysis and comparison of other methods of radiation treatment planning. More work in this direction would be interesting and similar mathematical tools could theoretically be used.

For more than one fraction of XRT, it is necessary to account for the growth of the tumour in between the two treatments. A simple commonly used model is logistic growth, depending on three parameters ρ, D_n and $n_{\max}$. In the various studies above, we have mostly neglected the change in the shape of the tumour between two fractions. However, this needs to be included in a more comprehensive study. Given all our results, we can propose a procedure for spatial optimization of radiation as follows:

- Image tumour twice. The change in shape of the tumour can then be used to model its growth mode; e.g. in order to deduce the parameters ρ, D_n, and $n_{\max}$. The most important ingredient for shaping the optimal beam is the cell density $n(\vec{x})$.
- Determine dose prescription and treatment schedule for the tumour. This provides constraints on individual and total allowed dosage, $\{F_n\}$ and the time intervals between fractions, $\{\tau_n\}$.
- Determine the physical limitations of the radiation apparatus; e.g. how many radial steps is the apparatus capable of accurately producing and superposing.
- Optimize the first radiation fraction using the above optimization procedure.
- Use the growth model deduced from the initial two images to model the growth of the tumour cells between fractions. The deduced cell density profile prior to each fraction can then be used as input to optimize the shape of the beam in that fraction. The assumptions on evolution of the profile after a fraction and in between fractions are likely to introduce errors. Ideally, more imaging can be done to obtain more precise cell density profiles at intermediate times.

This exploratory work examines spatial variations in the shape of radiation beams, and proposes improvements to radiation therapy by shaping beams according to the pre-treatment cell-density. The advantage of this method is the opportunity to reduce the total tumour cell number below that obtained in uniform radiation. In addition to the

initial tumour density profile, the method relies only on few tumour-specific parameters in order to carry out the optimization. In its current implementation, the method does not take into account other factors in radiation planning such as nearby organs at risk, scheduling, or other scoring indices used to compare dose distributions. Such factors could potentially be included in a more elaborate model, a direction that we hope to pursue in the future. A major limitation of the model is the exclusion of heterogeneity across the tumour volume as tumours usually vary in cell type, stemness, phenotypic expression, and perhaps most importantly, hypoxia. Although we added a logistic cytotoxic action term to account for different radiation efficacy across the area, this is relatively simplistic and could be improved with a more thorough specification of tumour heterogeneity. Another direction that was not examined here is the interaction of this spatially-varying radiation treatment with other therapies such as chemotherapy. We hope that this exploratory work sheds light on the spatial variation of radiation beams and inspires further work in the area.

Chapter 3

Role of Hypoxia-Activated Prodrugs in Combination with Radiation Therapy: An *In Silico* Approach

Abstract

Tumour hypoxia has been associated with increased resistance to various cancer treatments, particularly radiation therapy. Conversely, tumour hypoxia is a validated and ideal target for guided cancer drug delivery. For this reason, hypoxia-activated prodrugs (HAPs) have been developed, which remain inactive in the body until in the presence of tissue hypoxia, allowing for an activation tendency in hypoxic regions. We present here an experimentally motivated mathematical model predicting the effectiveness of HAPs in a variety of clinical settings. We first examined HAP effectiveness as a function of the amount of tumour hypoxia and showed that the drugs have a larger impact on tumours with high levels of hypoxia. We then combined HAP treatment with radiation to examine the effects of combination therapies. Our results showed radiation-HAP combination therapies to be more effective against highly hypoxic tumours. The analysis of combination therapies was extended to consider schedule sequencing of the combination treatments. These results suggested that administering HAPs before radiation was most effective in reducing total cell number. Finally, a sensitivity analysis of the drug-related parameters was done to examine the effect of drug diffusivity and enzyme abundance on the overall effectiveness of the drug. Altogether, the results highlight the importance of the knowledge of tumour hypoxia levels before administration of HAPs in order to ensure positive results.

3.1 Introduction

Tumourigenesis is a complex, multi-step process which leads to the formation of solid malignancies. A critical step in this process is angiogenesis in which tumours develop their own vasculature and blood supply. In normal tissues, angiogenesis is carefully self-regulated and tightly controlled, whereas in tumours, the vessels are structurally and functionally abnormal. Accordingly, they are often characterized by defective endothelia, basement membranes, and pericyte coverage leading to inefficient nutrient delivery to tumour cells despite a high global blood flow in the environment [16]. In particular, the poor delivery of oxygen results in regions of severe hypoxia - a trait observed in nearly all solid malignancies [96]. Tumour hypoxia has been linked to the increase of many cancerous behaviors such as genomic instability, malignant progression, and metastasis formation [40, 60].

The clinical implications of hypoxia for cancer therapy are also of great importance, most evidently in the context of radiation and chemotherapy. It has been established that resistance to radiation is conferred by hypoxia, and the mechanism by which this is achieved is well understood [38, 40]. The radioresistance arises in the hypoxic regions because of the relatively fewer oxygen-derived free radicals generated by ionizing radiation that compromise the cytotoxic effects of radiotherapy. In the case of chemotherapy, hypoxia has also been shown to elicit an overall decrease in efficacy *in vivo*. This is likely related to inefficient drug delivery due to the abnormal tumour vasculature, though the underlying mechanisms dictating this are less well understood [40, 66].

On the other hand, hypoxia is a theoretically ideal ideal target for guided drug delivery. To overcome hypoxia-induced treatment resistance, hypoxia-activated prodrugs (HAPs) have been developed that are nontoxic under physiological oxygen concentrations but are activated through a bioreduction specifically in hypoxic tumour regions. Once HAPs become activated at hypoxic sites, some of them are able to diffuse back out of hypoxic areas allowing them to attack nearby, non-hypoxic cells as well - a phenomenon called the bystander effect. These bystander effects play a vital role in the overall cytotoxic effectiveness of HAPs. Furthermore, the failure of several recent clinical studies involving HAPs suggests that one of the several factors contributing to this failure is insufficient classification of patients based on their hypoxia and nitroreductase expression statuses [44, 67]. Hence, not only the presence of hypoxia, but also its spatial distribution, might significantly influence the efficacy of treatments involving HAPs. Preclinical studies have examined the effect of HAPs, administered singly or in combination with conventional treatments such as chemotherapy and radiotherapy, resulting in very promising outcomes

in the control of tumour growth [55, 72, 104] [1]. Despite the theoretical and preclinical results, several HAPs have recently failed to demonstrate efficacy in clinical trials. The disconnect between theory and practice is hypothesized to be mainly due to sub-optimal patient selection and heterogeneities in distributions of hypoxia, in addition to other issues common to chemotherapies such as poor delivery due to the insufficient blood supply and high interstitial fluid pressures [44, 74]. A better understanding of these therapies and their interactions with tumour cells and the surrounding micro-environment for individual patients is required before they can be successfully translated into clinical practice.

Mathematical modelling approaches have been used to study the interaction between hypoxia and external beam radiation therapy [51, 73, 76, 105] as well as the action of HAPs [25, 26, 39, 54, 85]. Here, we developed an experimentally motivated mathematical model to predict the effect of HAPs by incorporating the amount of tumour hypoxia and the action of the prodrug as well as the sensitivity of activated metabolites. Once the model is calibrated and validated with appropriate experimental data, it can be used to determine the efficient administration of HAPs for a given tumour and to predict the outcome of a combination of HAPs and radiotherapy. Moreover, the developed mathematical model can be further used to analyse and generate testable hypotheses that can be further studied experimentally.

3.2 Mathematical Model

Our mathematical model is developed based on the experimental observations of TH-302 administration by Peeters *et al* [72]. In this study, Rhabdomyosarcoma R1 and H460 NSCLC xenografts were treated with TH-302 and external beam radiation therapy, and the effects on tumour size and hypoxic fraction were examined. Furthermore, the TH-302 efficacy based on initial hypoxia level was assessed as well as efficacy of its combination with radiation as well as order of treatment administration. In order to study the effect of HAPs and their bystander effects on tumour cells - particularly hypoxic tumour cells - we consider the spatio-temporal evolution of tumour cell concentration, oxygen distribution, inactive HAP distribution, and active metabolite distribution. If we denote $n(\mathbf{x}, t)$, $k(\mathbf{x}, t)$, $c(\mathbf{x}, t)$ and $c_a(\mathbf{x}, t)$ as the concentrations of tumour cells, oxygen, HAPs (inactive) and active metabolite at the location $\mathbf{x}$ and time t, we can write the model equations as given below.

[1] https://www.youtube.com/watch?v=LjbfbQ_OON8&t=s

Cancer Cells

$$\frac{\partial n(\mathbf{x},t)}{\partial t} = \underbrace{D_n \nabla^2 n(\mathbf{x},t)}_{\text{Diffusion}} + \underbrace{\frac{r\, k(\mathbf{x},t)^p}{k_g^p + k(\mathbf{x},t)^p}\, n(\mathbf{x},t)}_{\substack{\text{Oxygen-dependent} \\ \text{growth}}} - \underbrace{\delta_a c_a(\mathbf{x},t)\, n(\mathbf{x},t)}_{\substack{\text{Cell death by} \\ \text{activated HAPs}}} - \underbrace{\alpha_k\, d_t\, n(\mathbf{x},t)}_{\substack{\text{Cell death by} \\ \text{radiation}}} \quad (3.1)$$

$$\alpha_k = \alpha_h \frac{(\alpha_n/\alpha_h)\, k(\mathbf{x},t) + k_s}{k(\mathbf{x},t) + k_s} \quad , \quad d_t = \frac{d}{\tau} f(t) \quad (3.2)$$

Oxygen

$$\frac{\partial k(\mathbf{x},t)}{\partial t} = 0 = \underbrace{D_k \nabla^2 k(\mathbf{x},t)}_{\text{Diffusion}} + \underbrace{r_k v(\mathbf{x},t)}_{\text{Production}} - \underbrace{\frac{q_k k(\mathbf{x},t)^m}{k_c^m + k(\mathbf{x},t)^m}\, n(\mathbf{x},t)}_{\substack{\text{Oxygen-dependent} \\ \text{consumption}}} \quad (3.3)$$

Hypoxia Activated Prodrugs (HAPs)

$$\frac{\partial c(\mathbf{x},t)}{\partial t} = 0 = \underbrace{D_c \nabla^2 c(\mathbf{x},t)}_{\text{Diffusion}} + \underbrace{r_c g(t) v(\mathbf{x},t)}_{\text{Production}} - \underbrace{\frac{q_a k_a^u}{k_a^u + k(\mathbf{x},t)^u}\, c(\mathbf{x},t)}_{\text{Activation}} - \underbrace{\lambda_c c(\mathbf{x},t)}_{\text{Decay}} \quad (3.4)$$

Activated HAP (AHAPs)

$$\frac{\partial c_a(\mathbf{x},t)}{\partial t} = 0 = \underbrace{D_a \nabla^2 c_a(\mathbf{x},t)}_{\text{Diffusion}} + \underbrace{\frac{q_a k_a^u}{k_a^u + k(\mathbf{x},t)^u}\, c(\mathbf{x},t)}_{\text{Activation}} - \underbrace{\lambda_a c_a(\mathbf{x},t)}_{\text{Decay}} = 0 \quad (3.5)$$

The description of the relevant parameters and corresponding values are given in Table 3.1. Here, we assume that cancer cells ($n(\mathbf{x},t)$) follow an oxygen-dependent, exponential growth law and are treated with HAPs alone or in combination with external beam radiation therapy. The oxygen-dependent growth is incorporated to account for the well-known phenomenon of cancer cells altering their growth pathway in the absence of oxygen [99]. Mathematically, this is incorporated by the use of a Hill function, which is commonly used

to model the dependence of a rate on a specific quantity. Notice that as the oxygen concentration increases, the Hill function in the oxygen-dependent growth term approaches r (its maximum growth rate) and that as oxygen decreases, the growth rate approaches zero. The parameter δ_a, the rate of HAP-induced cell death, is assumed to be cell-specific and reflects the death rate of the cancer cells to the activated HAPs (sensitivity to warhead). The radiation induced cell kill is incorporated into the model using a linear term with a radiosensitivity parameter α_k and dose rate d_t. While α_k is a constant dependent on the tissue of interest, we employ an oxygen enhancement ratio to show the decreased effect of radiation in hypoxic areas of tumours. This is common in modelling the interaction of radiation with hypoxia and is shown above in equation (2) where oxygen concentration is incorporated into the equation for α_k [26]. When modelling external beam radiation therapy, the linear-quadratic model is often used to describe tumour survival. Here, we make the simplification that the linear term is dominant and exclusion of the quadratic term does not impact the qualitative results (as done in [51] for example). Radiation schedule is incorporated with the model using the function, $f(t)$, where $f(t) = 1$ when the radiation is given. Oxygen and drug distributions follow reaction diffusion equations and are assumed to be in quasi-steady state with respect to the computational time-step length used in numerical simulations. Specifically, their distributions are time-dependent over the course of the simulation, but achieve equilibrium within the span of a single computational time step of 0.001 days. Moreover, oxygen and HAPs are assumed to be delivered from the blood vessels. Here, $v(\mathbf{x}, t)$ stands for the density of the blood vessels and $v(\mathbf{x}, t) = 1$ for the presence of the blood vessel and zero otherwise. Notice that a Hill function is again utilized for modelling the dependence of the oxygen consumption on the oxygen concentration. The function $g(t)$, controls the delivery of HAPs and when HAPs are delivered, $g(t) = 1$. The inactive HAPs ($c(\mathbf{x}, t)$) supplied by the vessels are activated at the presence of hypoxia and nitroreductases to produce activated HAPs ($c_a(\mathbf{x}, t)$). Once again a Hill function is used to mathematically show the dependence of the HAP activation rate on oxygen concentration. The parameter q_a accounts for the rate by which HAPs are activated by nitroreductases. The active metabolites diffuse farther to produce a bystander effect affecting both hypoxic and oxygenated tumour cells. The formulation of the model is then completed by prescribing no-flux boundary conditions and an initial condition on the tumour cell density [76].

3.2.1 Computational Domain and Parameters

The simulations are performed using the images (Fig. 3.1) obtained with the help of immunofluorescence staining techniques on a H460 xenograft to obtain vascularity, perfusion,

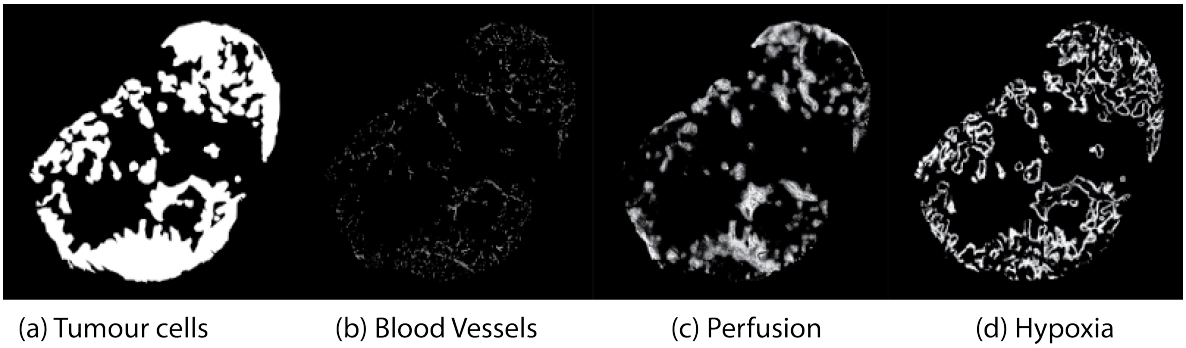

Figure 3.1: Binary images of the xenographt cross-section, illustrating total tumour area, blood vessels, perfusion and hypoxia, respectively.

and hypoxia using CD31 (endothelial marker), Hoechst 33342, and pimonidazole respectively, as described previously [72]. The stained tumour sections were then scanned and a threshold was applied to generate the corresponding binary masks.

Following Powathil *et al* [76], we assume that the perfused vascular network is the source of oxygen and drug supply, and thus gives the initial spatial distribution of concentrations. The perfused vasculature (at a fixed time) is obtained by combining the images of perfused areas (Hoechst 33342) and vascular structures (CD31) using the logical "AND" operation. The images of hypoxic regions (pimonidozole positive) are then used to compare the simulated hypoxic area and thus to calibrate/validate the mathematical model (Fig. 3.2). The simulation is carried out over the image of the tumour cross-section (tumour mask). Note that for the *in vitro* case, we may assume a uniform distribution of oxygen and drug concentrations (when given). Further details can be found in [76].

The parameters for the model are listed in the Table 3.1. When available, we have used suitable parameters from previous studies [51, 76]. The parameter values for oxygen dynamics have been calibrated to match the experimental results as shown in Fig. 3.2. The experimental findings [33, 84, 101], suggest that HAPs have the ability to diffuse into hypoxic areas and exert their effect. Importantly, the diffusion parameters used in our model are estimates based on experimental observations and therefore are reflective of both the diffusive properties of the substances as well as their interactions with cells near the blood vessel. Production or supply rate of the drug is assumed to be (around 1.6 times) lower than that of oxygen and the decay rates of HAPs and Activated Hypoxia-Activated Prodrugs (AHAP) are assumed to be 0.023 (1/s). Moreover, we assume that HAPs are activated when the oxygen concentration is less than 5 mmHg [102]. We have further

analyzed the effects of estimated parameter values using a sensitivity analysis, the results of which are reported in the relevant sections below. The initial spatial distribution of oxygen as determined from the vascular distribution is assumed to be constant with maximum value. Furthermore, we assume a uniform cell distribution as our initial condition, since we are considering a two dimensional cross section of *in vivo* xenografts.

To the best of our knowledge, most of the parameter values related to the evolution of HAPs and AHAPs are generally unknown or not clear and hence, these parameters are assumed phenomenologically based on the experimental observations and information. The clinical and experimental investigation into the effects and efficacy of HAPs alone or in combination with other treatment modalities is still in its infancy and consequently, modelling studies can play a vital role in providing a better overall qualitative or quantitative understanding. However, since these experimental and clinical studies are ongoing, the limited information available may not always help to accurately estimate all the necessary parameters needed for any modelling approaches. Nevertheless, they may help to give some qualitative, phenomenological estimates of the parameters that eventually help to provide qualitative inferences. Moreover, these modelling approaches can further inform experimental studies on accurately estimating appropriate parameters to provide quantitative insights. There are existing modelling works in this direction but each are focused on different compounds and settings and similarly use assumed values when accurate estimates are unavailable. However, these assumed values can be modified or refined when accurate values of these parameters are estimated. For the values that are assumed in the current study, a sensitivity analysis is given to illustrate the sensitivity of the model results on the parameter values. We believe that unavailability of such data should not hinder modelling studies that might inform and motivate related experimental research; although, one should consider these results with some reservations until accurate parameters are available.

The computational simulation involves a finite difference scheme in a MATLAB script applied to a system of equations which computes cell density, oxygen concentration, and the concentration of inactive and active HAPs over the tumour cross-section. A uniform distribution is used for the initial condition of tumour cells across the mask and the other equations are solved in the steady state, so an initial condition is not necessary. The tumour cross-section is considered to be a 200x200 grid and is treated over 5 days with the simulation consisting of 5000 time steps each of size 0.001 days. The time step length remains constant throughout the treatment and particularly during the treatment times.

Parameter	Symbol	Value (Unit)	Reference
Tumour Cell Diffusivity	D_n	0.32 (mm^2/day)	[51]
Growth Rate	r	0.35 (1/day)	[51]
Hill Coefficient	p	8	Assumed*
pO_2 at Half Maximum Growth	k_g	10 (mmHg)	Assumed*
Rate of HAP-Induced Cell Death	δ_a	10 (1/day[C_a])	Assumed*
Normoxic Radiosensitivity	α_n	0.30 (1/Gy)	[76]
Hypoxic Radiosensitivity	α_h	0.10 (1/Gy)	[76]
pO_2 at Half Maximum Radiation	k_s	3 (mmHg)	[76]
Radiation Dose	d	2-8 (Gy)	[72]
Irradiation Duration	τ	3 (minutes)	[76]
Radiation Schedule	$f(t)$	1 or 0	
Diffusion Coefficient (Oxygen)	D_k	2.50×10^{-5}(cm^2/s)	[76]
Rate of Oxygen Supply	r_k	0.12 (O_2/s)	Estimate*
Cellular Oxygen Consumption	q_k	0.04 (O_2/cells/s)	Estimate*
Hill Coefficient	m	2	Assumed*
pO_2 at Half Maximum Consumption	k_c	10 (mmHg)	Assumed*
Diffusion Coefficient (HAP)	D_c	$4.00e{-}5$ (cm^2/s)	Assumed*
Production Rate of HAP	r_c	0.07 ([HAP]/s)	Assumed*
HAP Schedule	$g(t)$	1 or 0	
Activation Rate of HAP	q_a	$8.40e{-}3$ (1/s)	Assumed*
Hill Coefficient (Activation)	u	2	Assumed*
pO_2 at Half Maximum Activation	k_a	5 (mmHg)	Assumed*
HAP Decay Rate	λ_C	$2.30e{-}2$ (1/s)	Assumed*
Diffusion Coefficient (AHAP)	D_a	$4.00e{-}5$ (cm^2/s)	Assumed*
AHAP Decay Rate	λ_a	$2.30e{-}2$ (1/s)	Assumed*

Table 3.1: List of Model Parameters (*for assumed and estimated parameters, refer to parameters section)

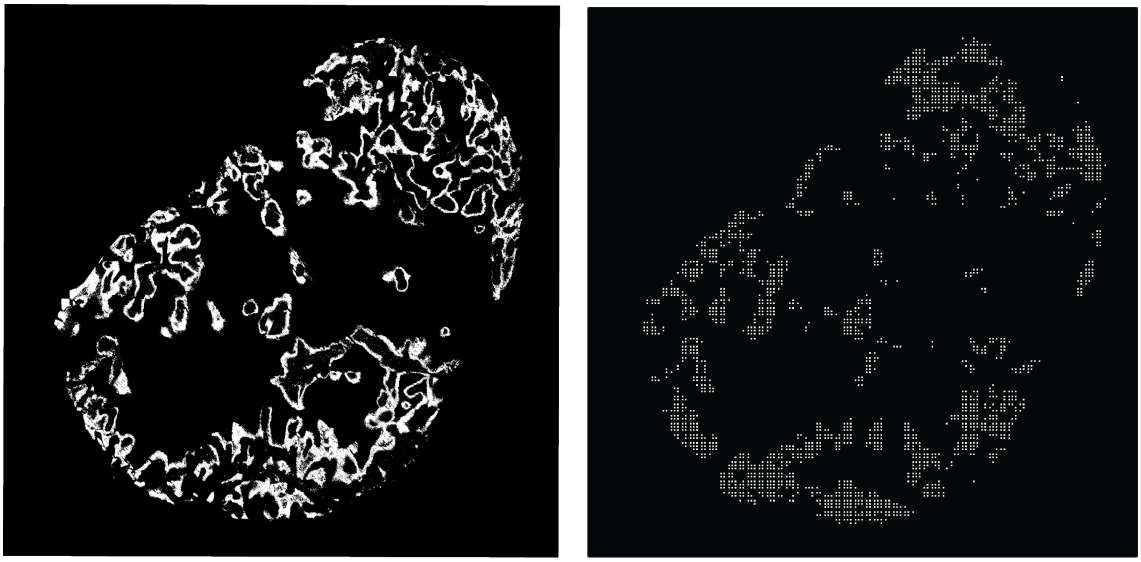

(a) Hypoxia from pimonidazole binding (b) Hypoxia from model simulations

Figure 3.2: Comparison of hypoxic images from (a) pimonidazole binding and (b) *in silico* model (white voxels in the *in silico* image correspond to hypoxic areas where $pO_2 < 10\ mmHg$). The amount of hypoxic area predicted by the model differs by 3.06% from hypoxic area calculated by pimonidazole binding. Furthermore, the images have an overall 90.63% agreement in their pixel colours.

The perfused vasculature network is read into the MATLAB script through the imread function.

3.3 Results and Discussions

The identification of hypoxia in many types of tumours and its role in treatment resistance, especially in radiation therapy, prompted the exploration of other treatment options - in particular, HAPs [44]. However, as discussed earlier, recent clinical studies have failed to demonstrate the success of various HAP-based treatments. One possible reason for this failure could be lack of detailed information about the hypoxia levels of each patient and how that affects the success of the therapy [44]. In this section, following Powathil *et al* [76], we discuss a theoretical, non-invasive approach to predict the spatial and temporal distribution of hypoxia (oxygen concentration) and analyze the effects of HAPs - alone and

in combination with radiation.

In earlier work, Powathil *et al* [76] discussed a computational approach to simulate and explore the spectrum of spatial hypoxia distributions at a snapshot in time that will result from a given vascular distribution. We used two-dimensional binary images of tumour cross-sections together with a vascular distribution as a computational domain on which a model for the oxygen distribution and tumour cell density was solved. The resulting hypoxic area was quantified and compared against the hypoxic proportions determined from images [76]. Here, since we are only considering viable tumour mass (tumour mask), necrotic regions are not included in the analysis. The methodology and results were discussed in detail in Powathil *et al* [76]. Here, we use a similar approach to estimate the hypoxia on a xenograft sample and use it to study the effects of HAPs under varying hypoxic conditions. Fig. 3.2 compares the binary images of hypoxia estimated using the mathematical model simulations and experiments (immunohistochemical analysis) and re-illustrates the usefulness of mathematical and theoretical approaches to predict hypoxic distributions. While the experimental and in silico tumours are not identical in their images, the model predicts hypoxic area to within 3.06% accuracy. As mathematical models are idealized by their nature, small discrepancies are expected. Furthermore, the model is still able to predict phenomena shown in experiments like efficacy based on hypoxic level and differences in sequencing.

3.3.1 HAPs and Hypoxic Levels

To study the role of spatial hypoxia distributions on HAP effectiveness, we used the above-described mathematical model to simulate the HAP response under two different hypoxic levels - low and high. In the low hypoxic case, we used all the perfused vessels obtained via image analysis of xenograft images [76] and in the high hypoxic case, we used a hypothetical scenario with only 50% of the perfused vessels. Fig. 3.3 shows the comparison of total cell number and corresponding hypoxic area before and after 5 days of HAP treatment. In both cases, HAPs are given as daily doses over 5 days (QD4). We assume that in each dose, the drug is active in the system (delivered via vessels) for up to 3 hours. This can be changed or adapted appropriately depending on the given drug or mode of delivery. Since the primary aim of this study is to qualitatively study the effects of HAPs, we believe this schedule to be sufficient.

The simulation results shown in Figure 3.3 are qualitatively in agreement with experimental results [72]. The plots show that HAPs are more effective in reducing the number of cells under high hypoxic conditions: HAP treatment reduces cell number by 60.4% in

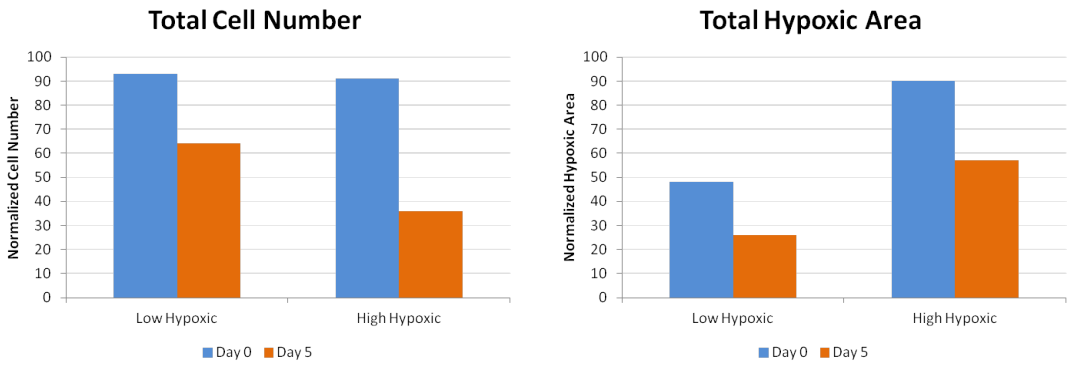

Figure 3.3: Plots showing the (a) total (normalized) tumour cell population and (b) (normalized) hypoxic area on day 0 and day 5, when the tumour is treated with HAPs only (4 daily doses with active metabolites for up to 3 hours). Cell number is normalized using the initial cell number and hypoxic area is scaled as a percentage of total tumour area.

the high hypoxic case and only by 31.1% in the low hypoxic case. Note that one possible reason for a relatively higher hypoxic area after treatment in simulation results might be due to the fact that experimental results account only for hypoxic area with viable cells (as binding is required), while simulation hypoxic area accounts for the hypoxic area within the entire domain (including regions with low cell density due to the cytotoxic effect of the released drug). This clearly indicates that information about hypoxic area can be a vital factor in determining the successfulness of treatments involving HAPs.

3.3.2 Combining HAPs with Radiation

Radiation therapy is widely known to be very effective at targeting well-oxygenated tumour cells while hypoxic cells often show a degree of radiation resistance. Therefore, the biological rationale in combining radiation with HAPs is very promising as HAPs target hypoxic cells, leaving radio-sensitive tumour cells to be killed by radiation. Furthermore, recent preclinical experimental studies [67, 70, 72] suggest that the antitumour effectiveness of HAPs is enhanced by combining HAPs with radiotherapy. Here, we use the formulated mathematical model to study the effects of HAPs alone and in combination with radiation in low- and high-hypoxic tumours. Fig. 3.4 shows the number of cells (Fig. 3.4(a)) and hypoxic area (Figure3.4(b)) before and after treatment under low- and high-hypoxic conditions. These results show that depending on the tumour type (hypoxia level), a com-

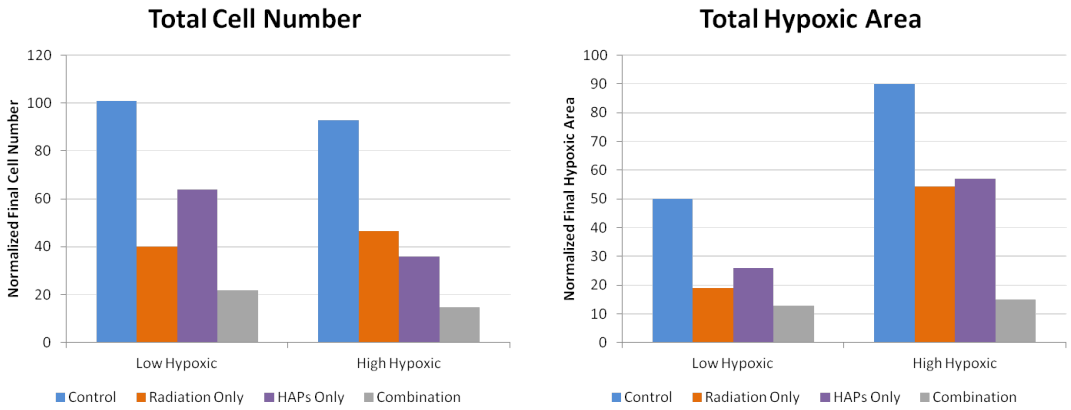

Figure 3.4: Plots showing the (a) total (normalised) cell number and (b) (normalized) hypoxic area at the end of day 5 when the tumour is treated with radiation only or combination of radiation and HAPs (8 Gy of radiation given over a 3 minute fraction on the first day of treatment with 4 daily doses of active metabolites for up to 3 hours). Cell number is normalized using the initial cell number and hypoxic area is scaled as a percentage of total tumour area.

bination treatment of radiation combined with HAPs can be very effective (compared to radiation alone).

3.3.3 Effects of Treatment Scheduling

Although combination therapies with HAPs have shown promising results in controlling a growing tumour, the positive response of this combination treatment often depends on the treatment sequencing and scheduling parameters. For example, Liu *et al* showed in xenograft models that TH-302 in combination with a conventional chemotherapeutic achieved the greatest tumour inhibition when TH-302 was administered 2-8 hours prior to its companion (either cisplatin, docetaxel, gemcitabine, or doxorubicin) [55]. This work hypothesized that administration of the conventional therapeutic prior to TH-302 caused a reoxygenation of the tumour microenvironment, therefore decreasing the activation rate of the HAP and leading to decreased efficacy. Conversely, HAP-first treatment was thought to lead to a reoxygenation allowing further penetration of the accompanying drug. Peeters *et al* examined the combination of TH-302 with radiotherapy applying TH-302 in different schedules with a single 8 *Gy* dose of radiation (as done in our simulations) [72]. They

showed that TH-302 combined with radiation therapy increased tumour control from the radiation monotherapy case. Furthermore, it was shown that pretreatment with TH-302 prior to radiation lead to optimal efficacy. They speculated that HAP treatment reduced the hypoxic fraction which enhanced the radiation effectiveness. Nytko *et al* showed the same qualitative results experimentally by combining radiation and HAP therapy, determining that a neoadjuvant (HAP-first) was the optimal treatment schedule [70].

Determining the optimal plan for administration of HAPs and radiation in a combination therapy is clearly an important goal. To help answer this question, the model was used to see the resulting tumour cell population and hypoxic area at the end of treatment for 5 different radiation schedules. In each schedule, HAPs are given on days 1 through 5 and the results are calculated at the end of the 5th day. An 8 Gy fraction of radiation is also given over a 3 minute interval on one of the first 4 days. Additionally, the case of splitting the dose into 4 fractions with 2 Gy/day was also included.

The analysis shows that the best option is to apply radiation on the 4th day of treatment, both in considering tumour cell population and hypoxic area. Though we only carried out this analysis for the 5-day treatment plan, we expect that this result would generalize to the best option simply being to apply radiation as late as possible. This is because the radiation has its highest effectiveness when hypoxic area is lowest: So naturally, the way to have the lowest hypoxic area is to apply the highest amount of HAPs before radiation. Similarly, the further fractionated 2 Gy/day schedule lies at a medium effectiveness. However this may not be the case for rapidly growing tumours where the turnover rate of hypoxic cells is very high. The results of this analysis are shown in Fig. 3.5.

3.4 Parameter Sensitivity Analysis

The effectiveness of HAPs is also influenced by other relevant measurable parameters. For example, the diffusivity of the inactive HAPs, D_c, impacts the delivery the drug to the hypoxic zones. To see this, we simulated the mathematical model with the drug diffusivity scaled by factors of 0.5 and 2 to see the effect on resulting tumour cell population and hypoxic area. This was done in combination with radiation therapy for radiation given either on day 1 or day 4. The results show that the larger diffusivity results in a decrease in tumour cells and hypoxic area while the smaller diffusivity results in an increase in tumour cells and hypoxic area. However, the overall effect due to either change in diffusivity is low.

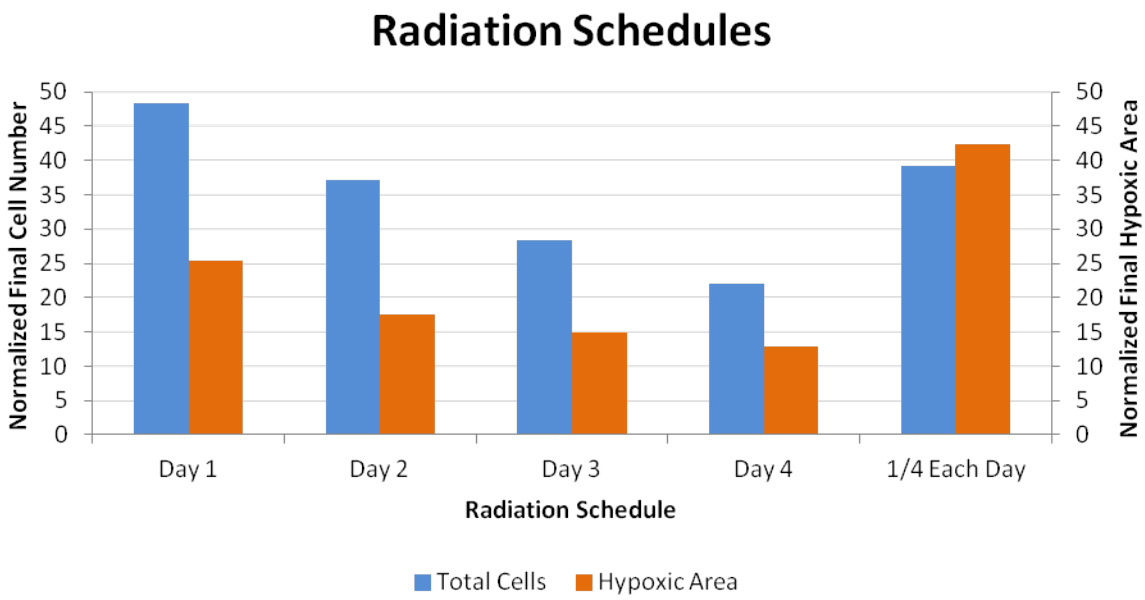

Figure 3.5: Plots showing the (a) total (normalized) cell number and (b) (normalized) hypoxic area on day 5 when the tumour is treated with Radiation and HAPs. HAPs are given on days 1 through 4 and remain active for up to 3 hours. 8 Gy of radiation is given over a 3 minute fraction on one of the first 4 days except for the final case in which 2 Gy radiation is given on each of the first 4 days. The cell number and hypoxic area are calculated at the end of the 5th day. Cell number is normalized using the initial cell number and hypoxic area is scaled as a percentage of total tumour area.

Another parameter which can be examined is the activation rate of the HAPs, q_a. While this activation rate can't easily be pharmacologically altered, it is potentially alterable through the expression of nitroreductases in the tumour cells. With measurements of the levels of these enzymes, this activation rate could be theoretically estimated. Like for the diffusivity, we simulated the model for the activation rate scaled by factors of 0.5 and 2 for radiation given on either day 1 or day 4. The results show that the higher activation rate leads to a decrease in cell number and hypoxic area and a decrease in activation rate leads to the opposite. The overall effect of the change in activation rate is more significant than the effect of changing the diffusivity.

The effectiveness of the HAPs also depends on the sensitivity of the activated HAPs in inducing cytotoxic effects to hypoxic and surrounding cells. For example, if it is an alkylating agent, the DNA repair status will be an important factor to consider while studying the effectiveness. DNA crosslinkers such as the drug evofosfamide TH-302, pose strong replication blocks and cellular survival requires the concerted action of nucleotide excision, Fanconi anemia (FA) and homologous recombination (HR) driven DNA repair pathways [88, 97]. The sensitivity to the drug is included into the model using the parameter δ_a and we have further explored its effects by varying this parameter. The results are reported in the Fig. 3.6. The results show that increased sensitivity improves final outcome (higher cell-kill and lower hypoxic area), as expected.

A similar analysis was performed to study the sensitivity of each of the parameters related to the HAPs including: r_c, λ_c, D_a, and λ_a in addition to D_c and q_a as mentioned above. This analysis consisted of simulating the model with each of the parameters sequentially scaled by a factor of either 0.5 or 2 for radiation given on either the first or the fourth day. The parameters are scaled one at a time to assess to which parameters the model is most dependent. Looking at Fig. 3.6, we can see that q_a, r_c, λ_c, and λ_a are the parameters which have the largest impact on tumour cell number and hypoxic area. Though this method is not a rigorous sensitivity analysis, it nonetheless is a good indicator of the stability and robustness of our model since scales of parameters do not lead to drastic changes in the overall results. As precise measurements of the parameter values are not reliably known, especially since they can vary patient-to-patient, we seek only to make qualitative predictions rather than quantitative ones. Accordingly, the goal of testing simple parameter scalings is to establish that the model is robust to changes of parameter values within a reasonable range. When precise measurements are able to be obtained, they can be used with the model to make more accurate predictions. The next step is thus to carefully design experimental studies to obtain relevant data such as HAP (drug specific) diffusivity and half-life to better understand and parameterize the mathematical model.

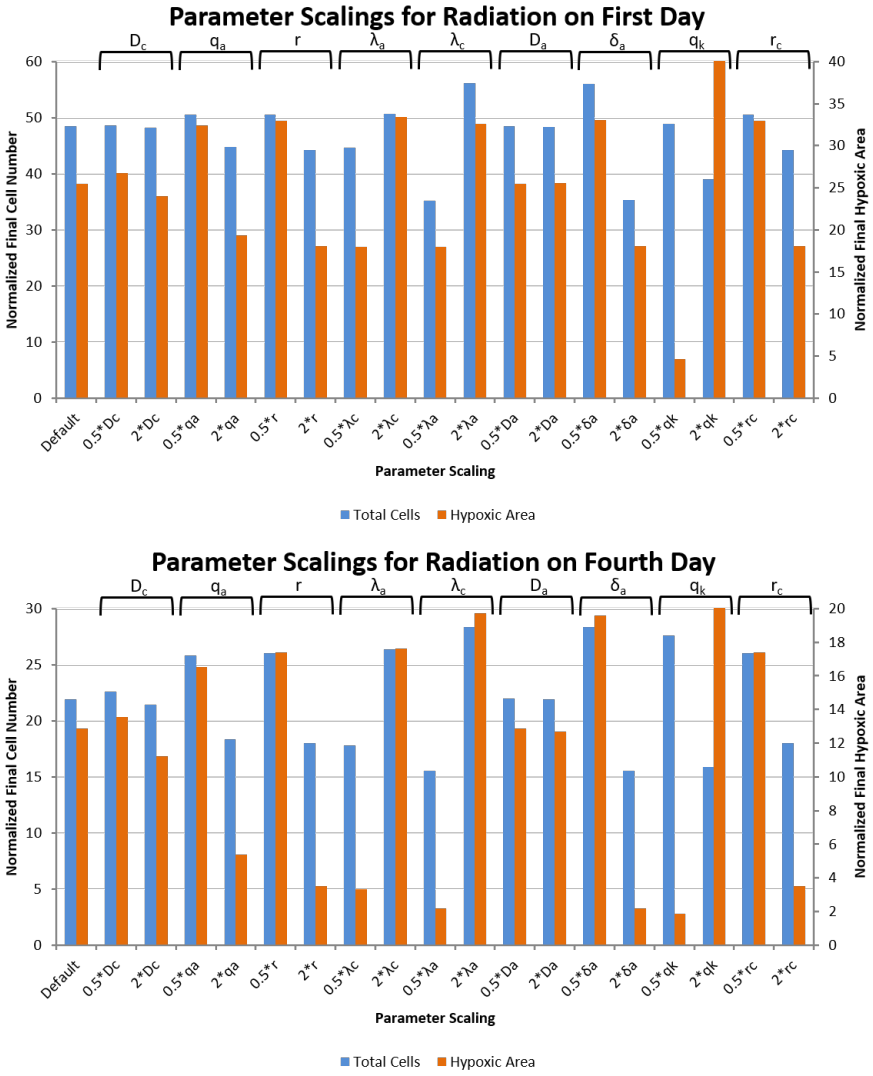

Figure 3.6: Plots showing the effect of scaling HAP diffusivity and activation rate on tumour cell population and hypoxic area for different radiation schedules. The top plot corresponds to HAPs given on each of days 1 through 4 which remain active up to 3 hours with radiation given on the first day. The bottom plot corresponds to the same HAP schedule with radiation given on day 4. The default parameters are given in Table 3.1. Cell number is normalized using the initial cell number and hypoxic area is scaled as a percentage of total tumour area.

3.5 Conclusions

We have developed here a spatio-temporal mathematical model to describe the effects of HAPs, alone and in combination with radiation, on a growing tumour. The model incorporates cell number, oxygen concentration, inactive HAPs, and activated metabolites. The system was solved on a domain obtained through imaging of perfused areas and vascular structures.

The model was solved for a low-hypoxia and high-hypoxia tumour to see which was more susceptible to treatment using HAPs. The model results showed a significant improvement in overall cell kill for tumours with high levels of hypoxia which was in agreement with experimental results [72]. This was extended to include a combination with radiation therapy which again predicted that the combination therapy is more effective for high-hypoxic tumours. Treatment sequencing was also altered to attempt to determine the optimal schedule of treatment methods. For our model, the best case scenario was to administer HAPs before radiation, which resulted in the highest cell kill and lowest hypoxic area. Additionally, scaling key model parameters can have an effect on the treatment efficacy. Simulating the results for different parameter scalings shows that increasing the diffusivity and activation rate of HAPs also improves the treatment efficacy, although the degree of change due to diffusivity scaling is relatively small.

Presently, the model is developed only using one cross-section of xenograft experimental image, showing its potential strength in studying the effects of HAPs in combination with radiation within a realistic microenvironmental setting. Further calibration and validation of the computational model using multiple images can help the model for further generalization. Also note that currently the model assumes a static vasculature over the treatment. Since the focus of this work is to study the effects of HAPs alone/in combination with radiation at a snapshot of the time with given spatial distribution of hypoxia resulted from a particular distribution of vasculature, the use of static vessels may be justified accordingly in a two dimensional settings. However, it would be ideal to simulate this in a three dimensional scenario, provided such spatial maps are available to implement the model. Furthermore, as the simulations take place over a maximum length of 5 days, the tumour vasculature is unlikely to change significantly over the course of treatment. For an *in vivo* tumour growing over a longer period of time, we would expect the vasculature to change throughout the treatment, thereby altering the transport of oxygen and drugs and effecting the treatment efficacy. This is another direction we hope to examine in the future. Another future direction is to incorporate a detailed pharmacodynamics of considered drug to improve the predictive ability of the model, moving a step closer to personalised therapeutic delivery. For example, for a drug such as PR-104, the inter-

mediate molecules along its activation path may play a significant role as they too can have cytotoxic effects [74]. However, for a drug such as TH-302, as we considered here, Bromo-Isophosphoramide Mustard (Br-IPM) is the lone dominant cytotoxic form (though the Cl-IPM metabolite also appears) [46]. Similarly, the simplified model that we used here to study radiation effects can be modified further to include multiple effects of radiation such as delayed cell death, indirect effects, cell-cycle sensitivity and so on, depending on the availability of the data and required complexity of the model. Spatial effects are also not examined to their full extent. Analysis of treatment efficacy as it relates to distance from vessels is an interesting question which we hope to examine in future works. As we use only one experimental image to generate the hypoxia distribution, the conclusions we can draw here are limited.

Although current predictions from the model are qualitative in nature, we have shown that the model can be used to understand the combined effects of radiation and HAPs in general. Moreover, the results from the model are in good agreement with experimental observations and the inferences from the model results, such as optimal combinations and sequencing, can be further analyzed and validated using appropriate experimental studies. Once the model is carefully calibrated with HAP-specific experimental data, it can be used for quantitative predictions and treatment optimizations. Furthermore, this model can be adapted for clinical applications by using relevant hypoxic data obtained from biopsies and novel imaging techniques such as perfusion CT imaging to spatially reconstruct tumour hypoxia map for the model.

Chapter 4

In Silico Analysis of Hypoxia-Activated Prodrugs in Combination with Anti-Angiogenic Therapy through Nanocell Delivery

Abstract

Tumour hypoxia is a well-studied phenomenon with implications in cancer progression, treatment resistance, and patient survival. While a clear adverse prognosticator, hypoxia is also a theoretically ideal target for guided drug delivery. This idea has lead to the development of hypoxia-activated prodrugs (HAPs): a class of chemotherapeutics which remain inactive in the body until metabolized within hypoxic regions. In theory, these drugs have the potential for increased tumour selectivity and have therefore been the focus of numerous preclinical studies. Unfortunately, HAPs have had mixed results in clinical trials, necessitating further study in order to harness their therapeutic potential. One possible avenue for the improvement of HAPs is through the selective application of antiangiogenic agents (AAs) to improve drug delivery. Such techniques have been used in combination with other conventional chemotherapeutics to great effect in many studies. A further benefit is achieved through nanocell administration of the combination. In the following, a mathematical model is outlined and used to compare the predicted efficacies of separate vs. nanocell administration for AAs and HAPs in tumours. The model is experimentally motivated, both in mathematical form and parameter values. Preliminary results of the

model are highlighted throughout which qualitatively agree with existing experimental evidence. The model predicts an increase in the efficacy of HAPs when combined with AAs and that the optimal administration method is through nanocell delivery.

4.1 Introduction

Hypoxia is a common feature of solid tumours resulting from an inadequate oxygen supply and has been associated with many negative cancer behaviours including increased metastasis and aggressive phenotypes, promotion of genetic instability, and decreased treatment effectiveness for immunotherapy, radiotherapy, and chemotherapy [19, 30, 31, 34, 37, 38, 40, 47, 60, 96, 102]. Accordingly, strategies to combat tumour hypoxia are in high demand. On the other hand, tumour hypoxia has gained significant interest in recent years for its potential as a target for selective drug delivery in cancer. In particular, hypoxia-activated prodrugs (HAPs) have emerged as a method for selective targeting of tumours through the exploitation of their hypoxic cores. HAPs are bioreductive compounds which remain inactive under normoxic conditions, but are metabolized under hypoxic conditions within the body into their cytotoxic forms. Their hypoxic selectivity is achieved through a $1e^-$ or $2e^-$ reduction reaction which is rapidly reversed under an abundance of oxygen, but serves as the first step in a reduction cascade under hypoxia. Importantly, this activation exclusively in hypoxic zones does not prevent HAPs from attacking non-hypoxic tumour cells. Once activated in hypoxic regions, HAPs are able to diffuse back into non-hypoxic regions and attack normoxic tumour cells - a phenomenon termed the Bystander Effect (although there is some debate regarding the overall importance of these bystander effects [33, 41, 91]). In the present study, we focus on the nitroimidazole-based HAP, TH-302 (Evofosfamide), which undergoes a $1e^-$ reduction to form the DNA cross-linking bromo-isophosphoramide mustard (Br-IPM) under hypoxia [32, 74].

Numerous experimental preclinical studies have analyzed the use of HAPs alone or in combination with other therapies, showing positive outcomes for the control of tumour growth and invasion ([33, 41, 55, 58, 70, 72, 101, 104] for example). Furthermore, mathematical models of HAP action have been developed which are able to accurately reproduce experimental results ([25, 26, 39, 83, 65] for example). Despite the theoretical understanding and promising traits of HAPs, clinical success has been hard to achieve as many HAPs have failed recent clinical trials [32, 44, 74]. In the case of TH-302, clinical trials have been ongoing for both its use in monotherapy and combination therapy for many years. TH-302 monotherapies have generally showed limited results in phase I/II clinical trials, whereas

its combination with radiation and/or other chemotherapeutics has had more positive results with the outcomes of ongoing trials eagerly awaited (see [7, 90] for recent overviews). Fortunately, there is genuine optimism in the field with the development and improvement of technologies such as medical imaging, biomarking, and genetic screening [44, 74]. Moreover, the disconnect between theory and practice is thought to be mainly a symptom of inappropriate patient selection, as treatment efficacy will be based on patient levels of hypoxia and nitroreductase expression [44, 67]. Nonetheless, HAPs also suffer from many of the same problems as conventional therapeutics. Most notable of these is the inefficient delivery of drugs to the tumour core due to insufficient blood supply and high interstitial fluid pressures caused by dysfunctional tumour vasculature.

Tumour vasculature is abnormal in a number of ways, including differences in the general structure and the specific behaviours of cells. Tumours achieve these differences largely through an up-regulation of pro-angiogenic factors such as Vascular Endothelial Growth Factor (VEGF) and Tumour Growth Factor - β (TGF-β) and a down-regulation of anti-angiogenic factors such as Thrombospondin-1 (TSP-1), causing the 'angiogenic switch' to be permanently switched to 'on' [16, 17, 35, 64]. Tumour vessels branch irregularly, forming a chaotic web of interconnecting paths which impede blood flow. Furthermore, the endothelial cells lining the vessel walls of tumours are often able to detach or stack on one another, leading to openings in the vessel wall. These openings not only enhance the ability of tumour cells to enter the blood stream, but contribute to the leakiness of vessels, allowing blood to pool in tissues and increase fluid pressures in the interstitium. These pressures prevent blood from exiting at the proper spots and delivering drugs or essential nutrients such as oxygen.

Notably, the inefficient delivery from tumour vessels is often not due to a reduction in the blood volume flowing through the tumour system (the number of vessels in the area). Instead, the main culprit is the inability of molecules to be properly delivered from vessels to tumour tissue due to the previously mentioned vascular irregularities. In the case of oxygen, hypoxic zones may be caused by two separate mechanisms. Some hypoxic regions may simply be a result of a lack of nearby blood vessels - which we refer to as diffusion-limited hypoxia - however, other regions become hypoxic due to inefficient delivery from a nearby vessel - which we refer to as perfusion-limited hypoxia. This has lead to the idea of tumours being 'over-vascularized', as the up-regulation of pro-angiogenic factors causes unregulated angiogenesis. From this has stemmed the notion of vessel normalization: the strategy of using antiangiogenic agents (AAs) to prune (rather than destroy) the tumour vasculature in attempt to improve the delivery of cytotoxic drugs to the tumour area. This normalized state appears for only a small amount of time after which the over-vascularization reappears, again causing decreased oxygen and drug delivery. This, in

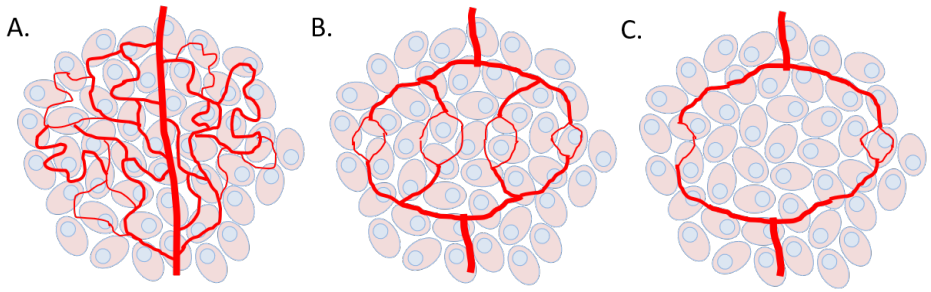

Figure 4.1: Cases of tumour vascularization. In A. the tumour is overvascularized with chaotic, irregular vessels ($m > 1$) causing perfusion-limited hypoxia. In B. vascular normalization ($m \approx 1$) is achieved where optimal oxygen or drug extravasation is realized. In C. a strong dose of AAs causes vascular destruction ($m < 1$), leading to diffusion-limited hypoxia in the tumour. Figure is adapted from Figure 3 in [45].

turn, activates Hypoxia-Inducible Factor (HIF-1α), which causes an up-regulation of pro-angiogenic factors. This has been termed the 'normalization window' and has been the subject of experimental ([9, 27, 103]) and mathematical ([50, 105]) studies. Together, these works have highlighted the importance of precise timing and dosing in administrations of combination therapies.

There are few experimental studies examining AA/HAP combinations, and these are compared with our model predictions in the discussion below. The strategy generally employed by these studies is to give a high dose of AAs in order to increase the level of hypoxia and therefore HAP activation. Although this may seem beneficial for the application of HAPs, the elimination of the tumour vessels prevents proper delivery of the HAPs from vessel to tumour. It was for this reason that using AAs for vessel normalization was initially suggested. However, the incorporation of normalization creates a paradox of optimal sequencing. In particular, if AAs are first applied to prune the vasculature and increase HAP delivery, then the drug activation will be hindered through the simultaneous increase in oxygen delivery (due to normalization of the vasculature). Conversely, if HAPs are applied first, then the aforementioned inefficient delivery will remain a hindrance. Similarly, the simultaneous administration does not avoid the trade-off between delivery and activation as if the HAPs do arrive during the normalization window, then they will arrive during optimal oxygen delivery as well.

To solve this dilemma, the use of redox-responsive nanocarriers is examined as a delivery vehicle for combination therapies involving AAs and HAPs. These nanocarriers were first

examined by Sengupta *et al* [86] who published a work detailing delivery via a 'nanocell' for the chemotherapeutic agent doxorubicin with the AA combretastatin. Nanocell administration allows for precise control over the temporal release of the drugs which was shown to increase the treatment efficacy from the separate administration case. The initial release of the AA causes a collapse of the tumour vasculature, leaving the subsequently released cytotoxin trapped within the tumour tissue. In [86], it is also suggested that nanocell administration technology could be extended to include additional chemotherapeutic agents, which we examine in the following for the administration of HAPs. The nanocells allow for an escape from the previously mentioned paradox by allowing HAPs to take advantage of both improved delivery and high activation rates.

As the use of HAPs increases, experimental and clinical explorations into their combination with AAs will inevitably appear. We therefore think it timely for applications of their combination to be examined to inform future studies and the feasibility of eventual translation to the clinic. We present here a mathematical model of AA/HAP combination treatments both in separate and nanocell delivery. We focus on the HAP, TH-302, and the AA, combretastatin, for the purposes of model form and parameter values. The model of separate administration is first explained, including a description of the reasoning for specific terms. The model is tested and refined by matching previously published experimental data and the results of previous mathematical studies including HAP efficacy based on tumour hypoxia level and efficacy of HAP/radiotherapy combination treatments. The ability of our model to produce the different cases of AA effect by examining hypoxic area under different strengths of AAs is also shown. The model is then extended to include nanocell delivery and show its improvement in cell kill over the separate administration case.

4.2 Methods

The mathematical model presented here is developed through building off of existing mathematical models and incorporating results from previously published experimental data. It consists of a system of reaction-diffusion equations for the essential components of the tumour growth and treatment system. The parameter meanings, values, and sources for separate administration can be found in Table 4.1 and for nanocell administration in Table 4.2. Most of the parameters are taken directly from previous mathematical modelling studies which estimated the parameters from experimental data. Parameters describing tumour cell growth, vasculature development, and oxygen distribution were taken from Kohandel *et al* 2007 [51] who estimated the parameters based on the experimental results

of Winkler *et al* 2004 [103]. For parameters describing the distribution and effect of the AA combretastatin, we rely on the reported values from Yonucu *et al* 2017 [105] who estimated parameters from the experimental results of [28, 53] and estimated some themselves. Parameters describing the HAP TH-302 were taken from Meaney *et al* 2019 [65] who estimated the parameters by matching to post-treatment images obtained through immunofluorescence staining techniques on a H460 xenograft tumour. Radiation parameters were taken from Powathil *et al* 2012 [76] and nanocell parameters were taken from Kohandel *et al* 2011 [50]. Since mathematical terms for cellular oxygen consumption and nanocell decay were not included in previous modelling studies, the values of the relevant rates were estimated by attempting to match with existing experimental results (as explained in Table 4.1). Each of the mathematical studies from which parameters were taken conducted sensitivity analyses, so we do not include another one here.

The model is first shown for the case of separate administration of combretastatin and TH-302 (Eqs. (4.1) - (4.7)), then for the nanocell administration (Eqs. (4.8) - (4.10)). Eq. (4.1) describes the tumour cell density, $n(\vec{x},t)$, at position $\vec{x}$ and time t, including a Laplacian diffusion term and logistic growth. These mathematical forms for cell growth and diffusion have been widely used in mathematical modelling of tumours [25, 26, 36, 50, 51, 65, 69, 77, 105]. To incorporate the increased growth rate of those cells nearby to tumour vessels, $m(\vec{x},t)$, the coupling term $\alpha_{mn}mn$ is included which allows for the cell density to exceed the carrying capacity imposed by logistic growth. This term is phenomenological and has similarly been used by previous studies ([105] for example). The final two terms of Eq. (4.1) allow for the killing effect of activated HAPs, $a(\vec{x},t)$, and radiation therapy administered on the schedule $R(t)$.

In order to model tumour vasculature, a course-grained model is used to develop the functionally deficient vessels. In Eq.(4.2), $m(\vec{x},t)$ represents the average blood vessel density which we assume to evolve in the same way as outlined in previous modelling studies [50, 51, 105]. The term $m(\gamma+\delta m+\epsilon m^2)$ allows for three fixed points under appropriate conditions on the constants $(\gamma<0,\delta>0,\epsilon<0)$. For the specific case of $\beta=-3\alpha$ and $\gamma=2\alpha$, there are two stable fixed points at $m=0$ and $m=1$ and an unstable fixed point at $m=1/2$. The case $m=1$ is considered to be vascular and $m=0$ to be nonvascular. In the absence of tumour cells, the vasculature will simply develop into a web of $m=0,1$ with steep drop-offs in the transitions. To model the overvascularization induced by the presence of tumour cells, the terms $\alpha_{nm}nm$ and $-\beta_{nm}\nabla\cdot(m\nabla n)$ are included. The first of these models the recruitment of pro-angiogenic factors by tumour cells and the second models the chemotaxis of blood vessels toward the tumour core. Importantly, these terms allow for the over-vascularization $(m>1)$ typical of tumours to occur. The final term of Eq. (4.2) allows for the destruction of vessels through the application of AAs, $A(\vec{x},t)$.

Eq. (4.3) describes the partial pressure due to oxygen in the tumour area. The distribution of oxygen is assumed to be in quasi-steady state with respect to the computational time-step length. Importantly, this does not mean that the distribution remains constant throughout the simulation, but rather that it will reach its equilibrium state within the length of a single computational step (which is described below). Eq. (4.3) uses a combination of mathematical terms from Kohandel *et al* 2007 [51], Powathil *et al* 2012 [76], and Meaney *et al* [65]. Oxygen is assumed to diffuse according to the common Laplacian diffusion and decay exponentially at a rate η. It is also assumed that, as in [65], oxygen is consumed by tumour cells at a rate dependent on the local oxygen availability. This rate is dictated by a Hill function, a common form in biological modelling. Notice that this consumption rate approaches q_k (its maximum consumption rate) as oxygen concentration increases and 0 as it decreases. For oxygen delivery from vessels, the form $r_k m e^{-\left(\frac{m}{m_{lim}}\right)^2}$ is used which allows for a different delivery efficiency depending on the density of tumour vasculature. This term has been utilized in previous modelling studies for delivery of oxygen as well as drugs to tumour sites [50, 51]. Notice that if $m_{lim} = \sqrt{2}$, this delivery curve attains a maximum at $m = 1$ (also see Fig. 4.2 for this delivery curve). With this form, the delivery of oxygen (and HAPs in Eq. (4.5)) is hindered by the over-vascularization in the tumour. Mathematically, the goal of vessel normalization is to bring the value of m toward 1 to improve the delivery of drugs and oxygen as controlled by this term.

For combretastatin (Eq. (4.4)), the equation outlined by Yonucu *et al* 2017 [105] is adopted which describes the concentration of AAs throughout the tumour area. As with oxygen, combretastatin concentration is assumed to be in quasi-steady state with respect to the computational time step. Combretastatin diffuses and decays exponentially at a rate k_A. $A_\nu(t)$ is the combretastatin concentration in plasma which is manually selected according to the appropriate treatment schedule. Diffusion from the vessels occurs with a transvascular diffusivity λ_A. Drainage of combretastatin to the lymph vessels is included such that drainage is hindered in the tumour. This is done with the cell density-dependent parameter $\Gamma_l(n)$ which takes a different value depending on the cell density at that location. Computationally, this is applied using a 'smoothed' step-function to maintain continuity so as to avoid computational errors.

Eq. (4.5) models the concentration of inactive TH-302, which is assumed to diffuse and undergo exponential decay. Additionally, TH-302 is transported into the system through the imperfect delivery term as in the case of oxygen in Eq. (4.3). The factor $H(t)$ is the administration schedule for HAP treatment which is manually assigned. The activation of TH-302 to Br-IPM is modelled by the term $-\frac{q_c k_a^2}{k_a^2+k^2}c$ in Eq. (4.5) and its negative in Eq. (4.6).

To model the effect of radiation therapy on the tumour, an Oxygen Enhancement Ratio (OER) is employed as done by others ([25, 65]). This models the phenomenon of radiation therapy having a larger effect on well-oxygenated cells than on hypoxic cells because of the creation of oxygen free-radicals which cause DNA damage. As can be seen in the first part of Eq. (4.7), as oxygen concentration increases, the OER approaches the value of α_1, and as oxygen concentration decreases, the OER approaches α_2 (with $\alpha_1 > \alpha_2$). Accordingly, radiation effect is given by the well-known linear-quadratic (LQ) model for radiation efficacy as in the second part of Eq. (4.7) with the radiobiological parameters α and β.

Tumour Cell Density

$$\frac{\partial n(\vec{x},t)}{\partial t} = D_n \nabla^2 n + rn\left(1 - \frac{n}{n_{lim}}\right) + \alpha_{mn} mn - \delta_a an - nR(t) \tag{4.1}$$

Vessel Density

$$\frac{\partial m(\vec{x},t)}{\partial t} = D_m \nabla^2 m + m(\gamma + \delta m + \epsilon m^2) + \alpha_{nm} nm - \beta_{nm} \nabla \cdot (m \nabla n) - \sigma m A \tag{4.2}$$

Oxygen Partial Pressure

$$0 = D_k \nabla^2 k + r_k m e^{-\left(\frac{m}{m_{lim}}\right)^2} - \frac{q_k k^2}{k_c^2 + k^2} n - \eta k \tag{4.3}$$

Anti-Angiogenic Agent (Combretastatin)

$$0 = D_A \nabla^2 A + \lambda_A m(A_\nu(t) - A) - \Gamma_l(n) A - k_A A, \quad \Gamma_l(n) = \begin{cases} \lambda_l^{tumour}, \text{ if in tumour} \\ \lambda_l^{normal}, \text{ otherwise} \end{cases} \tag{4.4}$$

Hypoxia-Activated Prodrug (TH-302)

$$0 = D_c \nabla^2 c + r_c H(t) m e^{-\left(\frac{m}{m_{lim}}\right)^2} - \frac{q_c k_a^2}{k_a^2 + k^2} c - \lambda_c c \tag{4.5}$$

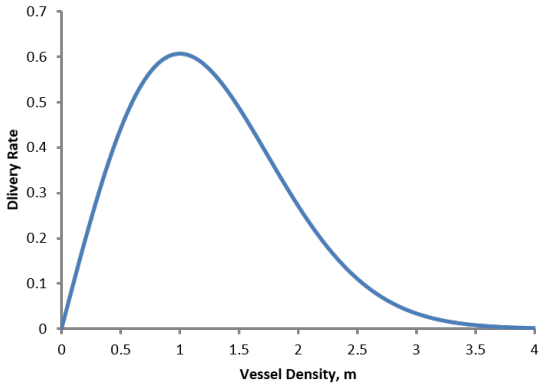

Figure 4.2: The delivery rate from vessels as a function of the average vessel density, $m(\vec{x},t)$. Curve is described by the function $me^{-\left(\frac{m}{m_{lim}}\right)^2}$. Notice that the optimal vessel delivery occurs at $m = 1$. As m becomes greater than 1, the delivery rate decreases, allowing for the impaired delivery due to overvascularization.

Activated HAP (Br-IPM)

$$0 = D_a \nabla^2 a + \frac{q_c k_a^2}{k_a^2 + k^2} c - \lambda_a a \tag{4.6}$$

Radiation Equations

$$O(k) = \frac{\alpha_1 k + \alpha_2 k_s}{k + k_s}, \quad R(t) = \begin{cases} [\alpha + \beta O(k) D]\, O(k) D, & \text{during radiation} \\ 0, & \text{otherwise} \end{cases} \tag{4.7}$$

The separate administration model can be extended to include nanocell delivery. The equations for cells, vasculature, and oxygen remain unchanged, but the equations for Combretastatin and TH-302 require slight alterations. First, an equation for nanocell concentration, $N(\vec{x},t)$, is added which involves only transport into the system and exponential

Parameter	Symbol	Value (Unit)	Reference
Cell Growth			
Diffusivity of Tumour Cells	D_n	3.50e-2 (mm^2/day)	[51]
Cell Proliferation Rate	r	0.35 (1/day)	[51]
Cell Carrying Capacity	n_{lim}	2.00e6 (1/mm^2)	[51]
Proliferation Rate from Vessels	α_{mn}	0.40 (1/day)	[51]
Tumour Vasculature			
Diffusivity of Blood Vessels	D_m	1.75e-4 (mm^2/day)	[51]
Vessel Production Rate	α_{nm}	4.38e-8 (1/day)	[105]
Vessel Chemotaxis Rate	β_{nm}	4.40e-10 (mm^2/day)	Estimate[1]
Vasculature Scale	m_{lim}	$\sqrt{2}$	[51]
Vessel Efficiency Factor	γ	-0.35 (1/day)	[51]
Vessel Efficiency Factor	δ	1.05 (1/day)	[51]
Vessel Efficiency Factor	ϵ	-0.70 (1/day)	[51]
Oxygen			
Diffusivity of Oxygen	D_k	1.05e-3 (mm^2/day)	[51]
Oxygen Supply Rate	r_k	0.280 (1/day)	[51]
Max Oxygen Consumption Rate	q_k	1.75e-8 (mmHg/cell/day)	Estimate[2]
Half-Max P_{O_2} Consumption	k_c	10.0 (mmHg)	[65]
Oxygen Decay Rate	η	7.14e-2 (1/day)	[51]
Anti-Angiogenesis Drugs			
Diffusivity of Anti-Angiogenic	D_A	3.46 (mm^2/day)	[105]
Transvascular Diffusivity	λ_A	0.35 (1/day)	[105]
Anti-Angiogenic Decay Rate	k_A	0.14 (1/day)	[105]
Hydraulic Conductivity	λ_l^{tumour}	0 (1/mmHg/day)	[105]
Hydraulic Conductivity	λ_l^{normal}	57.54 (1/mmHg/day)	[105]
Hypoxia-Activated Prodrugs			
Diffusivity of Inactive HAP	D_c	2.16e-2 (mm^2/day)	[65]
Diffusivity of Active HAP	D_a	2.16e-2 (mm^2/day)	[65]
Inactive HAP Supply Rate	r_c	0.07 ([HAP]/day)	[65]
Max HAP Activation Rate	q_c	726 (1/day)	[65]
P_{O_2} for Half-Max Activation	k_a	5.00 (mmHg)	[65]
Inactive HAP Decay Rate	λ_c	2.30e-2 (1/day)	[65]
Active HAP Decay Rate	λ_a	2.30e-2 (1/day)	[65]
Death Rate Due to HAP	δ_a	10.0 (1/[HAP]/day)	[65]
Radiation			
Max Oxygen Enhancement	α_1	1	[76]
Min Oxygen Enhancement	α_2	1/3	[76]
P_{O_2} for Half-Max Radiation	k_s	3.00 (mmHg)	[76]
LQ Model Linear Constant	α	0.10 (1/Gy)	[76]
LQ Model Quadratic Constant	β	0.03 (1/Gy^2)	[76]
Radiation Dose Rate	D	8 (Gy/day)	[72]

Table 4.1: [1] The term involving β_{nm} originally comes from [105] who used a finite difference scheme to solve their model. The difference in spatial discretization necessitates an alteration of the value of β_{nm}. Its new value is estimated to qualitatively match the vasculature obtained in [105]. [2] q_k was changed from the value in [51] to increase the effect of combretastatin and make the differentiation between cases of AAs more pronounced.

decay. The production term is given by the same imperfect delivery form as utilized previously for oxygen and drug transport. $N_\nu(t)$ is manually assigned and controls the schedule of administration. Since TH-302 and combretastatin are released from nanocells, the production terms from Eqs. (4.4) and (4.5) are altered such that the molecules emerge from nanocells instead of vessels. Additionally, $S_A(t)$ and $S_C(t)$ are introduced which are the release profiles of the combretastatin and TH-302 from nanocells, respectively. The forms of the release profiles are taken from Kohandel *et al* 2011 [50] who chose them based on the experimental results by Sengupta *et al* 2005 [86]. Sengupta *et al* found that the release of doxorubicin was delayed relative to the release of the combrestatin. The forms of the release profiles are given below where N_C and N_A are the normalization constants and $t_0^{(A)}$ and $t_0^{(C)}$ are the start time of the release profiles relative to the nanocells which are selected based on the administration schedule. These normalization constants are included to ensure a fair comparison between the administration types and more details on their derivation can be found in the appendix. The equations remain unchanged otherwise. They can be seen below in Eqs. (4.8)-(4.10).

Nanocell (NC) delivery

$$0 = R_N N_\nu(t) m e^{-\left(\frac{m}{m_{lim}}\right)^2} - \lambda_N N \tag{4.8}$$

Combretastatin through NCs

$$0 = D_A \nabla^2 A - \lambda_A m A - \Gamma_l(n) A - k_A A + R_A N S_A(t), \quad S_A(t) = N_A (t - t_0^{(A)})^{P_A} e^{-(t-t_0^{(A)})/t_A} \tag{4.9}$$

TH-302 through NCs

$$0 = D_c \nabla^2 c + R_c N S_C(t) - \frac{q_c k_a^2}{k_a^2 + k^2} c - \lambda_c c, \quad S_C(t) = N_C (t - t_0^{(C)})^{P_C} e^{-(t-t_0^{(C)})/t_C} \tag{4.10}$$

The model was computationally implemented using a second-order accurate continuous Galerkin finite element method with Euler time-stepping solved on a circular domain. The

Parameter	Symbol	Value (Unit)	Reference
Nanocell Supply Rate	R_N	0.28 (1/day)	[50]
Nanocell Decay Rate	λ_N	0.18 (1/day)	Estimate[1]
Anti-Angiogenic Release Rate	P_A	0.10	[50]
HAP Release Rate	P_c	0.30	[50]
Anti-Angiogenic Half-Life	t_A	0.83 (days)	[50]
HAP Half-Life	t_C	0.12 (days)	[65]

Table 4.2: [1] The nanocell decay rate is estimated by matching initial concentrations of combretastatin from the separate and nanocell cases.

FEniCS Project Finite Element PDE Solver [4, 57] was used to solve the system using a Neumann (no flux) boundary condition on the circular domain boundary. The system was nondimensionalized prior to solving (details in appendix). For initial conditions, the tumour cell density begins with a small Gaussian distribution at the centre with a standard deviation of approximately 0.63mm (2 nondimensional units). Vessels begin randomly distributed over the domain between 0 and 1. From there, they evolve into the normal vascular structure. The rest of the model equations are solved in quasi-steady state and therefore do not require initial conditions. The administration schedules of the drugs and nanocells are added computationally with temporal step functions. The drug concentrations in the plasma are assumed to decay exponentially. The schedules used will be pointed out as appropriate in the results section below. The normalization constant used in the release profiles from nanocells is included such that the total drug administered to the patient is equal so that a fair comparison between the two methods can be made. Importantly, this does not mean that the total drug concentration is the same. In particular, in the cases involving vascular normalization, the point of using AAs is to improve delivery and therefore have more drugs extravasated to the tumour area. Rather, the normalization of the drug schedules ensures that the same amount of drug would enter the system if the vessel distributions were identical. For all simulations, the same initial conditions were used (see Fig. 4.3). A time step length of 1 hour was used for most simulations and 10 minutes for those involving radiation therapy. The unstructured spatial grid was generated such that there were 32 elements along the radius of the circular domain.

4.3 Results

To test the model, previously obtained results from experimental and mathematical studies were reproduced. The simplest of these was that TH-302, singly administered, is more effective in a tumour with a higher level of hypoxia. To show this, two tumours were simulated from identical initial conditions for 15 days with different oxygen supply rates, r_k. One tumour had the supply rate as reported in Table 4.1, the other had a supply rate half of that. To these tumours, 5 doses of TH-302 were given in two-day increments starting on the 15th day (days 15, 17, 19, 21, and 23) where the plasma concentration of TH-302 is assumed to halve every 3 hours (as in [65]). The results show that treatment on the high-hypoxia tumour kills 57% of the tumour cells while treatment on the low-hypoxia tumour kills only 23% of the cells. These results can be seen in Fig. 4.4. This matches with the qualitative results as obtained by Meaney *et al* [65] who performed the same numerical experiment with a different mathematical model. Importantly, the mathematical model used in that study did not include an equation for vessel distribution, but rather used a constant vasculature obtained from imaging. Also, that study used a finite difference scheme to solve the model whereas a finite element method was used here. Though this result is unsurprising based on our understanding of the action of HAPs, we believe that it is important to include as it not only acts as a check on the qualitative predictions of our model, but also stresses the importance of pre-treatment knowledge of the hypoxia level of the tumour when predicting the effectiveness of HAPs.

Another preliminary result examined was the combination of TH-302 with radiation therapy. Specifically, Peeters *et al* [72] administered TH-302 with radiotherapy to rabdomyosarcoma R1 and H460 NSCLC and showed that the combination was an improvement over either therapy administered singly. Furthermore, they showed that a single 8 Gy dose of radiation was most effective when given after administration of TH-302, rather than prior to or simultaneously with TH-302. They hypothesized that HAP treatment reduced the hypoxic fraction of cells, thus leading to more oxygen free-radicals which improved the radiation efficacy. Nytko *et al* [70] determined the same qualitative result by showing that neoadjuvant (HAP-first) therapy was optimal when combined with radiotherapy. Meaney *et al* [65] were able to produce the same qualitative results using mathematical modelling. They showed that for TH-302 given once per day for five straight days, the optimal timing for radiotherapy was on the 5th day after the final dose of HAPs. This would align with the hypothesis suggested by [72] and echoed by [70]. Here, our model was used to reproduce the findings of [65] so as to further verify the action of TH-302 in our system. The treatment schedule used was exactly that as in [65] with TH-302 given on each of 5 straight days with 8 Gy of radiation given on one of the days.

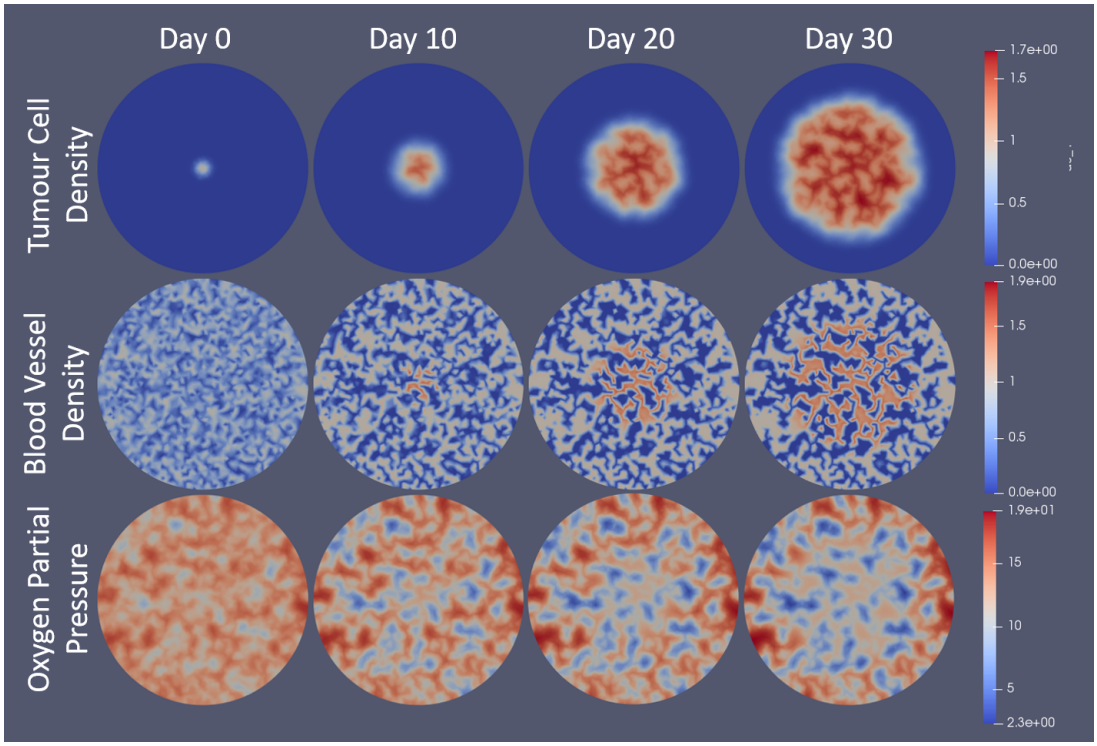

Figure 4.3: Visualization of model results for tumour cell density, blood vessel density, and oxygen partial pressure over a 30 day span with no treatment. Model is solved using the FEniCS Project Finite Element Solver [4, 57] and is visualized in Paraview [6]. Tumour cells begin as a normalized Gaussian distribution with a standard deviation of approximately 0.63mm. Vessels start randomly distributed between 0 and 1 over the domain. Oxygen is solved in quasi-steady state with respect to the time step length. Day 0 corresponds to the solution of the system after the first time step. Notice that vessels grow toward islands or tubes of density 0 and 1 in the absence of tumour cells, but will become overvascularized ($m > 1$) in the presence of tumour cells. Also notice that the oxygen concentration decreases in tumour area due to the overvascularization. Scales on the right correspond to the nondimensional units.

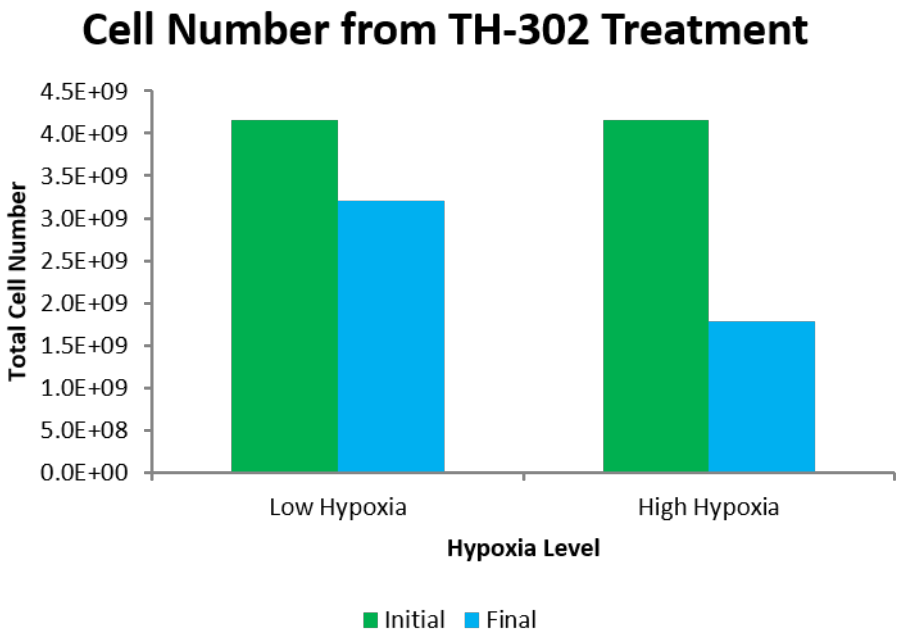

Figure 4.4: Comparison of TH-302 effectiveness for tumours of different hypoxic levels. The tumour is allowed to grow for 15 days before TH-302 treatment. TH-302 is given every other day starting on the 15th day and the plasma concentration is assumed to have a half life of 3 hours. The high hypoxic case is from the parameters listed in Table 4.1 while the low hypoxia case assumes a halved oxygen supply rate (r_k). Initial cell number is taken from the time step immediately before treatment and final cell number is taken from the time step immediately following treatment. TH-302 treatment kills only 23% of tumour cells in the low hypoxic case while it kills 57% of cells in the high hypoxic case.

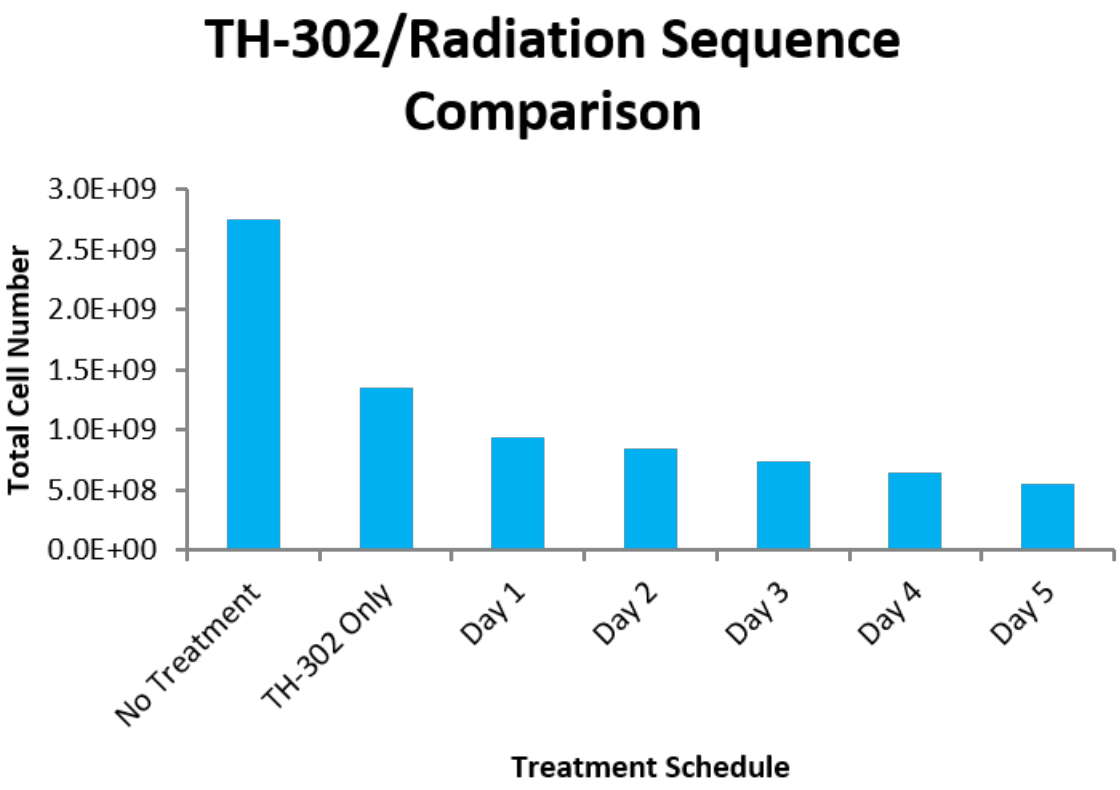

Figure 4.5: Efficacy of TH-302/radiotherapy combinations based on administration sequence. The tumour is allowed to grow for 15 days with TH-302 treatment starting on the 15th day. TH-302 is then given every day for 5 straight days with radiation given 6 hours after TH-302 on one of the days. Resulting cell number is calculated at the end of the 5th day, after all treatment has ceased. Notice that the later radiotherapy is administered, the more tumour cells are killed.

Next, we used the model to simulate the effect of single administration of combretastatin given in the same schedule as in Yonucu *et al* 2017 [105] who gave 5 daily doses in decreasing amounts (of magnitudes 1, 0.75, 0.5, 0.25, and 0.1) with a half life of 20 hours as used in [65]. From this, the antiangiogenic strength parameter, σ was altered to generate different cases of drug effect. The change in hypoxic area was examined in order to observe the phenomenon of application of antiangiogenic agents resulting in an improvement in oxygen distribution. The results are shown in Fig. 4.6 where three distinct cases of effects can be seen. For a weak combretastatin effect, there is a small increase in normoxic area ($[O_2] > 10$mmHg) and a small decrease in the amount of moderate hypoxic area ($5 < [O_2] < 10$mmHg) in addition to a very small increase in severe hypoxic area ($[O_2] < 5$mmHg). The hypoxic ranges were chosen from the accepted ranges in literature ([39, 40] for example). Generally, areas which are severely hypoxic are diffusion-limited and those which are moderately hypoxic are perfusion-limited. As the strength of the combretastatin increases, there is a point where the increase in normoxic area (and corresponding decrease in perfusion limited hypoxia) is optimized. Beyond this point, the normoxic increase declines and the area becomes diffusion limited and severely hypoxic. This shows the ability of the model to produce the different cases of AA effect. Very strong AA strength causes vascular destruction which greatly reduces the oxygen. For intermediate AA strength, optimal oxygen proliferation is achieved through vasculature normalization by pruning $m(\vec{x}, t)$ such that it is brought closer to 1.

With the preliminary results, the paradox of AA/HAP sequencing can be examined. The application of a strong dose of AAs will result in a large increase in hypoxic area, but the destruction of tumour vessels will prevent effective delivery of HAPs to the tumour. Accordingly, the normalization case of AA effect is used in the combinations in attempt to produce optimal cell kill. In theory, appropriate administration of combretastatin prior to TH-302 should improve TH-302 delivery (through normalization process), while impairing TH-302 activation to Br-IPM. Conversely, if TH-302 is given first, the delivery from vessels will be sub-optimal. In the simulations, treatment schedules began on the 18th day with doses being given every other day. In the sequencing cases, the drug types were either given at the same time or six hours apart on each of the days. Many different sequencing schedules were simulated, and the six hour interval produced the largest sequencing effect. Specifically, leaving a longer time between administration of combretastatin and TH-302 allowed the normalization window to close before TH-302, and a shorter time did not allow for the vasculature to be fully normalized. When simulated, the model shows that the combination improves cell kill, but that this improvement is significantly smaller than the sum of the individual effects of the combretastatin and TH-302. This can be seen in Fig. 4.7. The combretastatin-first treatment gives the highest cell kill, albeit slightly,

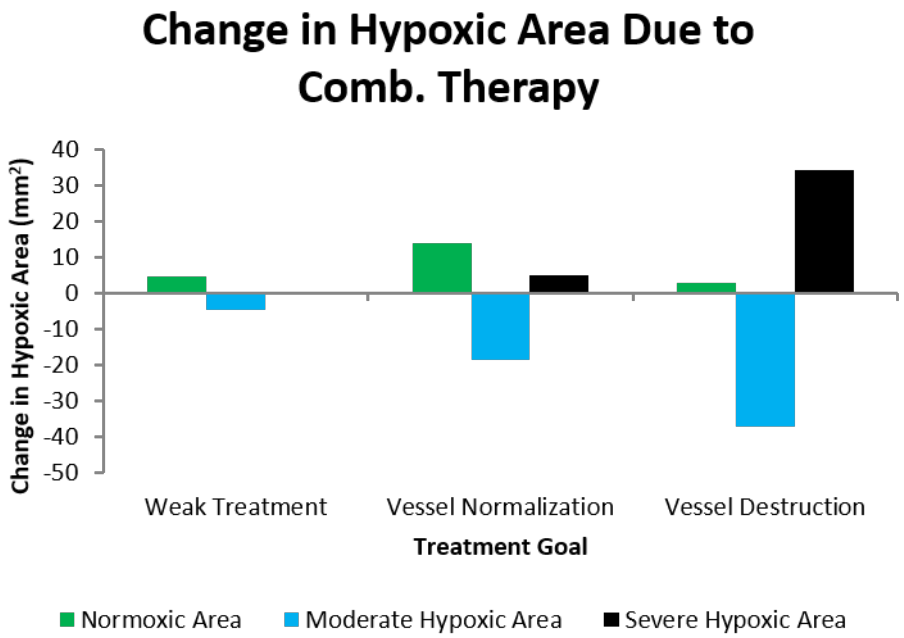

Figure 4.6: Cases of antiangiogenic therapy effect based on combretastatin strength. Weak treatment corresponds to an antiangiogenic strength parameter of $\sigma = 20$, vessel normalization to $\sigma = 30$, and vessel destruction to $\sigma = 70$. Normoxic area is where $[O_2] > 10$mmHg, moderate hypoxic where $5 < [O_2] < 10$mmHg, and severe hypoxic where $[O_2] < 5$mmHg. The hypoxic ranges were chosen from the understood ranges of tumour hypoxia ([39, 40] for example). Combretastatin is given every other day starting on the 15th day in decreasing amounts (of magnitudes 1, 0.75, 0.5, 0.25, and 0.1). Notice that there is an optimal middle strength where the increase in normoxic area is maximized.

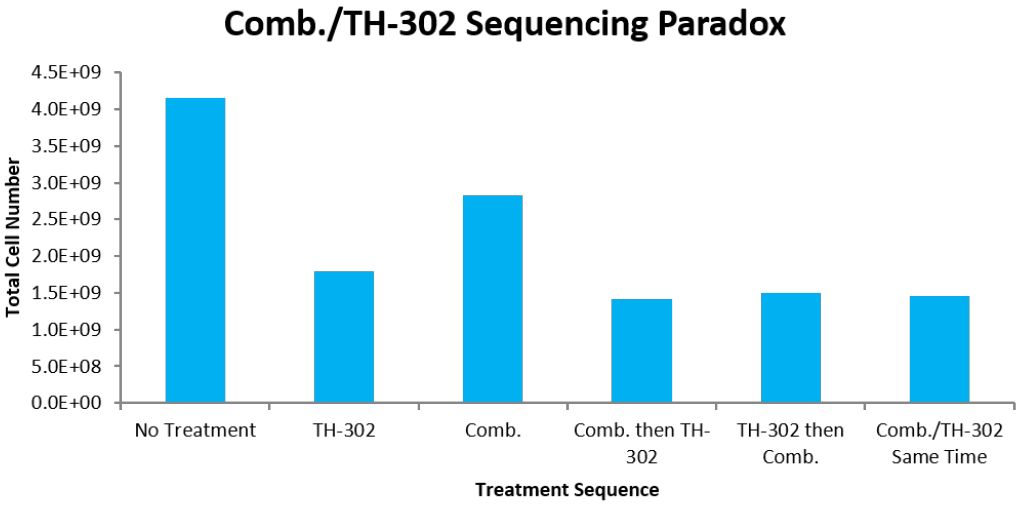

Figure 4.7: Combretastatin/TH-302 sequencing paradox with vessel normalization. The tumour is allowed to grow for 18 days before the start of treatment. Five doses of drugs are given in 2 day increments, each at the same strength. If both types of drugs are given non-simultaneously, then there is a 6 hour delay between their administrations. The optimal schedule is to give combretastatin 6 hours prior to TH-302, although it is only slightly better than other sequences. Furthermore, the combination therapy fails to show any drug synergy effects.

compared to the other sequences. This improved the cell kill to 66%, which is notably less than the sum of the effect of combretastatin (32%) and TH-302 (57%) individually.

To improve the combination, nanocell administration was simulated using the model outlined in Eqs. (4.8) - (4.10). The schedule used was the same as in the combretastatin-first sequence in Fig 4.7. Ideally, nanocell administration will result in improved TH-302 delivery while retaining the hypoxia needed for activation to Br-IPM. The resulting drug concentrations from the different administration methods can be seen in Fig. 4.8. Notice that the release profile from nanocells produces a different drug concentration profile than separate administration. Importantly, the concentration of drugs in the plasma remains constant between the methods while the concentration seen by the tumour depends on the perfusion rate from vessels. The plasma concentration is kept constant through normalization factors in Eqs. (4.9) and (4.10) (details in appendix). The difference in cell kill can be seen in Fig. 4.9 where the nanocell delivery improves cell kill from the 66% reported

above to 85%. Although the 85% still falls below the sum of the individual effects, a 19% increase in cell kill is a notable improvement.

4.4 Discussion

Although HAPs have been investigated for several decades, their mainstream application has become popular in recent years primarily due to advancements in various medical technologies. The most attractive quality of HAPs is their specificity towards neoplastic tissue, leading to less patient side effects and maximal observed drug concentration for the tumour. The motivation for their continued development despite limited clinical success is a function of nonspecificity of other conventional chemotherapeutics. The lack of clinical success has been attributed largely to inefficient patient selection in trials, but other improvements are still necessary [32, 44, 67, 74, 90, 108]. For instance, the hypoxia selectivity for many HAPs is simply too low for effective treatment [32]. Furthermore, *in vivo* evaluations of HAPs have taken place over differing delivery methods including intravenous injection, intraperitoneal injection, and oral administration [90]. A deeper understanding of preferred administration methods is needed for clinical advancement of HAPs. Additionally, as we move further into the era of personalized medicine, knowledge of the key reductases involved in the activation, transportation, *etc* of HAPs will be crucial [44, 74, 90]. In all of these endeavors, mathematical models have and can continue to provide valuable insight [25, 26, 39, 41, 61, 65, 83]. Hopefully HAPs can progress through the various stages of clinical development, where they currently reside.

Since HAPs remain largely in testing phases, there are few experimental studies examining their combination with AAs. In 2015, Yoon *et al* [106] combined TH-302 and radiotherapy with the AA DC101 to examine combination effects in xenograft mouse models of sarcoma. Their results showed that the addition of TH-302 to the combination treatment improved the blockage of tumour growth, with tumours remaining dormant for up to 3 months after treatment. The TH-302/DC101 combination was shown to significantly decrease the tumour proliferation from the individual cases. It is unclear whether or not there was any evidence of drug synergy, or whether the effect of combination was simply the sum of the effects of the individual drugs. Furthermore, the effects of treatment sequencing were not examined, with DC101 always being given 2 hours prior to TH-302 or radiation. Furthermore, vessel normalization for the purpose of enhancing drug delivery was not discussed, rather DC101 was given mainly for the purpose of oxygenating the tumour and improving radiotherapy. Following this, in 2016 Yoon *et al* [18] combined TH-302 with pazopanib in genetically engineered and xenograft mice, showing that the

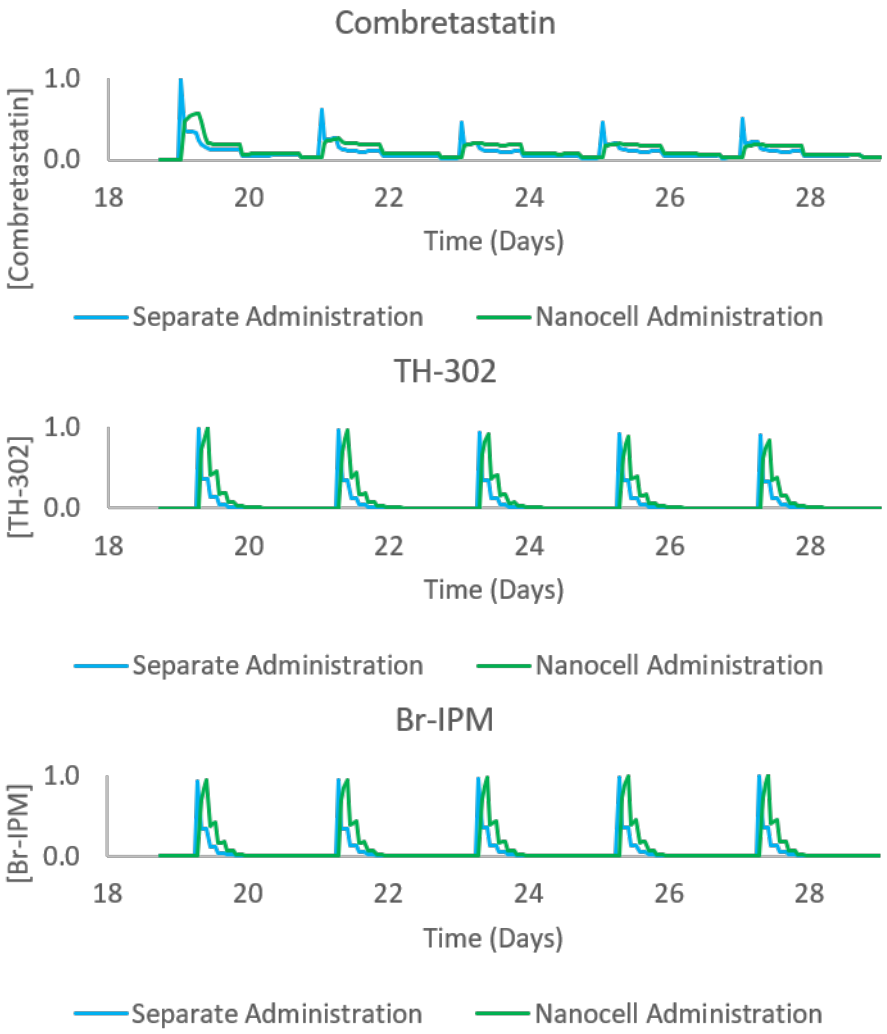

Figure 4.8: Normalized drug concentrations in the tumour area over the treatment schedule for combretastatin-first treatment administered either separately or through nanocells. Notice the delayed release through the nanocell release profiles.

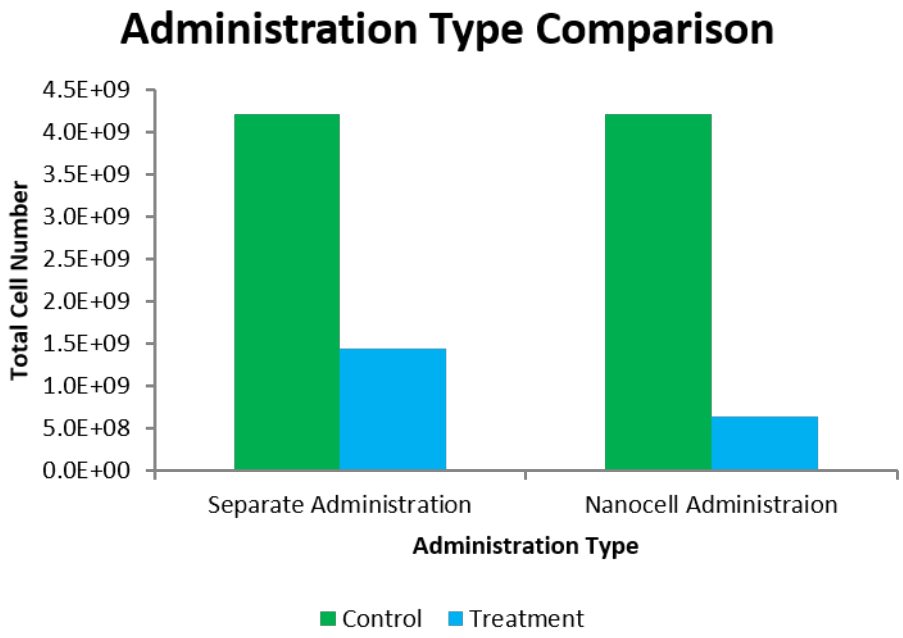

Figure 4.9: Comparison of optimal separate administration sequence vs. nanocell administration. Treatment schedules are as shown in Fig. 4.8. Notice the improvement in cell kill in the nanocell administration.

multimodal therapy enhanced the treatment in all cases. Sequencing, nor vessel normalization were discussed here as well. In 2017, Liu *et al* [56] combined TH-302 with the AA sunitinib in either short-term or long-term treatment, with the two being given at the same time. In the long-term treatment, the combination was more effective in reducing tumour volume than either drug individually, but there was no evidence of drug synergy as, over long treatment, each drug resulted in a large drop in tumour volume already. In the short-term case, the effect of the sunitinib individually was negligible, however when combined with TH-302 resulted in a dramatic decrease in tumour volume. Interestingly, the investigators assumed the increased efffect of the TH-302 to be due to an increase in hypoxia from the sunitinib. However, there was no discussion of drug delivery changes due to vessel normalization. The presence of drug synergy in the short-term case and not the long-term case is perhaps suggestive that vessel normalization occurred in such a way that drug delivery was optimized with a minimal reduction in hypoxic area. Finally, Kumar *et al* [52] again combined TH-302 with sunitinib, but no drug synergy was evident. They even speculated that the lack of drug synergy was perhaps due to vessel normalization which reduced the hypoxia such that the TH-302 was less effective. Clearly, the combination of AA/HAP treatment has potential to be a powerful one, but more experimental studies are necessary in order to fully understand the mechanisms at play. The little available evidence suggests that drug synergy is possible, but that precise scheduling and dosing is crucial to success. We propose in this mathematical study that nanocell administration may be beneficial in realizing the right dosing and scheduling and be able to increase effectiveness through utilizing the increased delivery and hypoxia.

Similarly, vessel normalization techniques are a relatively new concept in oncology, although the theory is well-understood and many experimental studies have examined its effect ([22, 49, 103] for example or [17, 62] for recent reviews). Through these, it has become abundantly clear that normalizing, rather than destroying tumour vasculature is the preferred mode of treatment [62]. To rationalize this phenomenon, it is helpful to understand that tumour oxygenation is one of the best indicators of patient survival, largely through its ability to promote aggression and metastasis, further immunosuppression, and enhance treatment resistance [17, 19, 31, 37, 62, 96]. It is then reasonable that reoxygenating a tumour could improve patient survival. This is often done through VEGF inhibitors - the action of most AAs. The AA examined here, combretastatin, has a different effect which is to suppress the capillary-like tube formation of endothelial cells by attacking vessel walls (although it appears to have some VEGF blocking capabilities as well) [89]. As such, combretastatin was modelled as attacking vessels from within (as was done in [105]).

As with any mathematical model, ours is not perfect, nor do we claim it to be. Specifically, the model can only be used reliably for qualitative predictions. This is largely due

to the imprecision of parameter measurements and the variability of parameters between patients. The key parameters used in our system have all been subject to sensitivity analyses within the works that they came from. Although the mathematical assumptions made have generally been made by others as well, one could legitimately question their validity. The infinite diffusion speed imposed by Laplacian diffusion is obviously non-physical. Similarly, the immediate, rather than delayed effect of drugs and radiation is not biologically reasonable. One could also question the validity of using a vessel density field to model vasculature. It should be stressed again that these are mathematical approximations made in order to derive qualitative predictions, not precise measurements used for quantitative analysis. Ideally, a similar analysis can be done using imaged vasculature which can be imported into the model, but this is obviously far more difficult and costly.

4.5 Conclusion

The use of HAPs has increased greatly in recent years due to the advancement of medical technologies and biological understanding. With the slow pace of HAPs in clinical trials, the need has arisen for novel methods of improving HAP efficacy. One potential avenue for improvement is through the use of AAs which could improve drug delivery through normalizing the abnormal and inefficient tumour vasculature. Unfortunately, in this lies an apparent paradox of increased HAP delivery leading to decreased HAP activation. Although there may exist an optimal middle ground between the two extremes, this work investigates drug nanocells, an alternative approach which has the potential to achieve both increased delivery and activation. This is done through a mathematical analysis, building off many previous modelling studies and using experimental results to inform model approximations and parameters. The model is able to reproduce known results of HAPs, AAs, and radiotherapy, which help to inform the model. The model predicts an increase in AA/HAP combination efficacy through the use of drug nanocells from the separately applied cases, regardless of sequencing. Qualitatively, the model predictions match with published experimental results, but clearly more results are necessary. Hopefully, models such as this can inspire further exploration into the combinations of HAPs with AAs in order to accelerate HAPs through clinical trials. One such way to do this could be through the use of drug nanocells, as outlined here.

Chapter 5

Conclusion

5.1 Summary

This thesis includes three research papers each devoted to answering questions in oncology by utilizing mathematical and computational techniques. The first of these developed a mathematical approach to spatially optimize the application of XRT using data obtained from pre-treatment MRIs. The analysis showed that by changing the spatial distribution of radiation, the total cell kill can be increased from the clinically-applied uniform case. The second paper outlined a system of reaction-diffusion PDEs which modelled the activity and effect of the HAP TH-302. It also modelled the combination of TH-302 with XRT, attempting to optimize the administration schedule of the combination. The results showed that the model was able to predict results similar to those obtained through imaging and existing experiments, most notably in that the optimal schedule was realized when TH-302 was administered prior to the radiation. The final paper described tumour vasculature as a system of PDEs and used this model to examine the combination of TH-302 with the AA combretastatin. The work outlined the trade-off between HAP delivery and activation, eventually using the model to show that administration of the combination through drug-carrying nanocells allowed for a bypassing of the trade-off altogether, achieving optimal cell kill.

Given the impressive history of applied mathematics in science, the inclusion of mathematical modelling into the life sciences should be viewed with significant optimism. Though mathematical oncology remains in its infancy as a subfield of research, the contributions from it are nonetheless remarkable. Ideally this thesis provides justification for that optimism in the future of cancer research.

5.2 Future Directions

In addition to the model extensions mentioned throughout this thesis, there are numerous future studies that we hope to pursue. First, while the results presented match with or are based on existing experimental evidence, the predictions made need to be experimentally validated. In order to do this, the models would need to be calibrated to the specific experimental setting, then the predictions could be rigorously tested. Second, the models provided here are mainly formulated in two dimensions, when extensions to three dimensions are certainly possible. While this is mathematically quite simple, it would require considerable computational power. However, in order for these models to be eventually utilized in a clinical setting, extending them to three dimensions would likely be a necessary first step. Finally, recent work has shown that the distributions of important populations in a system may be fully predictable exclusively from a discrete set of noisy measurements of that system [78, 79, 80]. This method could potentially be used with imaging data to obtain crucial information about a tumour which could be used to plan treatments.

References

[1] J. C. L. Alfonso, G. Buttazzo, B. García-Archilla, M. A. Herrero, and L. Núñez. A class of optimization problems in radiotherapy dosimetry planning. *Discrete and Continuous Dynamical Systems - Series B*, 17(6):1651–1672, 2012.

[2] J. C. L. Alfonso, G. Buttazzo, B. García-Archilla, M. A. Herrero, and L. Núñez. Selecting Radiotherapy Dose Distributions by Means of Constrained Optimization Problems. *Bulletin of Mathematical Biology*, 76(5):1017–1044, 2014.

[3] J. C. L. Alfonso, M. A. Herrero, and L. Núñez. A dose-volume histogram based decision-support system for dosimetric comparison of radiotherapy treatment plans. *Radiation Oncology*, 10(1):1–9, 2015.

[4] M. S. Alnæs, J. Blechta, J. Hake, A. Johansson, B. Kehlet, A. Logg, C. Richardson, J. Ring, M. E. Rognes, and G. N. Wells. The fenics project version 1.5. *Archive of Numerical Software*, 3(100), 2015.

[5] A. R. A. Anderson and P. K. Maini. Mathematical Oncology. *Bulletin of Mathematical Biology*, 80(5):945–953, 2018.

[6] U. Ayachit. The paraview guide: A parallel visualization application. *Kitware, 2015, ISBN 978-1930934306*, 2015.

[7] N. Baran and M. Konopleva. Molecular pathways: Hypoxia-activated prodrugs in cancer therapy. *Clinical Cancer Research*, 23(10):2382–2390, 2017.

[8] I. B. Barsoum, C. A. Smallwood, D. R. Siemens, and C. H. Graham. A mechanism of hypoxia-mediated escape from adaptive immunity in cancer cells. *Cancer Research*, 74(3):665–674, 2014.

[9] T. T. Batchelor, A. G. Sorensen, E. Tomaso, D. G. Duda, K. S. Cohen, K. R. Kozak, D. P. Cahill, J. Chen, M. Zhu, M. Ancukiewicz, M. M. Mrugala, S. Plotkin, J. Drappatz, D. N. Louis, P. Ivy, D. T. Scadden, T. Benner, S. Jay, P. Y. Wen, and R. K. Jain. AZD2171, a Pan-VEGF Receptor Tyrosine Kinase Inhibitor, Normalizes Tumor Vasculature and Alleviates Edema in Glioblastoma Patients. *Cancer*, 11(1):83–95, 2009.

[10] S. M. Bentzen and V. Gregoire. Molecular-imaging-based dose painting a novel paradigm for radiation therapy prescription. *Semin Radiat Oncol*, 21(2):101–110, 2011.

[11] G. Berg, E. Blomquist, and E. Cavallin-Ståhl. A systematic overview of radiation therapy effects in brain tumours. *Acta Oncologica*, 42(5-6):582–588, 2003.

[12] P. Black. Management of malignant glioma: role of surgery in relation to multimodality therapy. *Journal of NeuroVirology*, 4:227–236, 1998.

[13] A. Brahme and A. K. Argren. Optimal dose distribution for eradication of heterogeneous tumors. *Acta Oncologica*, 26(5):377–385, 1987.

[14] P. K. Burgess, P. M. Kulesa, J. D. Murray, and E. C. Alvord. The Interaction of Growth Rates and Diffusion Coefficients in a Three-Dimensional Mathematical Model of Gliomas. *Journal of Neuropathology and Experimental Neurology*, 56(June):704–713, 1997.

[15] Canadian Cancer Sociey. Canadian Cancer Statistics Special topic : Pancreatic Cancers. *Canadian Cancer Society*, pages 1–132, 2017.

[16] P. Carmeliet and R. K. Jain. Molecular mechanisms and clinical applications of angiogenesis. *Nature*, 473(7347):298–307, 2011.

[17] P. Carmeliet and R. K. Jain. Principles and mechanisms of vessel normalization for cancer and other angiogenic diseases. *Nature Reviews Drug Discovery*, 10(6):417–427, 2011.

[18] Y. Changhwan, K. C. Kevin, H. L. Jun, D. T. William, C. P. Hart, M. C. Simon, and Sam S. Multimodal targeting of tumor vasculature and cancer stem-like cells in sarcomas with VEGF-A inhibition, HIF-1α inhibition, and hypoxia-activated chemotherapy. *Proceedings of the 2002 Congress on Evolutionary Computation, CEC 2002*, 7(28):42844–42858, 2016.

[19] J. P. Cosse and C. Michiels. Tumour Hypoxia Affects the Responsiveness of Cancer Cells to Chemotherapy and Promotes Cancer Progression. *Anti-Cancer Agents in Medicinal Chemistry*, 8(7):790–797, 2008.

[20] L. M. DeAngelis, Peter C. Burger, S. B. Green, and J. G. Cairncross. Malignant glioma: Who benefits from adjuvant chemotherapy? *Annals of Neurology*, 44(4):691–695, 1998.

[21] A. di Lonardo, S. Nasi, and S. Pulciani. Cancer: We should not forget the past. *Journal of Cancer*, 6(1):29–39, 2015.

[22] S. Du, H. Xiong, C. Xu, Y. Lu, and J. Yao. Attempts to strengthen and simplify tumor vascular normalization strategy using tumor vessel normalization promoting nanomedicine. *Biomaterials Science*, 2019.

[23] S. Duckett. *The Pathology of the aging human nervous system*. Oxford University Press, 1991.

[24] L. Feuvret, G. Noël, J. J. Mazeron, and P. Bey. Conformity index: A review. *International Journal of Radiation Oncology Biology Physics*, 64(2):333–342, 2006.

[25] A. Foehrenbacher, K. Patel, M. R. Abbattista, C. P. Guise, T. W. Secomb, W. R. Wilson, and K. O. Hicks. The Role of Bystander Effects in the Antitumor Activity of the Hypoxia-Activated Prodrug PR-104. *Frontiers in Oncology*, 3(October):1–18, 2013.

[26] A. Foehrenbacher, T. W. Secomb, W. R. Wilson, and K. O. Hicks. Design of Optimized Hypoxia-Activated Prodrugs Using Pharmacokinetic/Pharmacodynamic Modeling. *Frontiers in Oncology*, 3(December):33–35, 2013.

[27] M. Franco, S. Man, L. Chen, U. Emmenegger, Y. Shaked, A. M. Cheung, A. S. Brown, D. J. Hicklin, F. S. Foster, and R. S. Kerbel. Targeted anti-vascular endothelial growth factor receptor-2 therapy leads to short-term and long-term impairment of vascular function and increase in tumor hypoxia. *Cancer Research*, 66(7):3639–3648, 2006.

[28] A. Gabizon, R. Catane, B. Uziely, B. Kaufman, T. Safra, R. Cohen, F. Martin, A. Huang, and Y. Barenholz. Prolonged circulation time and enhanced accumulation in malignant exudates of doxorubicin encapsulated in polyethylene-glycol coated liposomes. *Cancer Research*, 54(4):987–992, 1994.

[29] T. Galochkina, A. Bratus, and V. M. Pérez-García. Optimal radiation fractionation for low-grade gliomas: Insights from a mathematical model. *Mathematical Biosciences*, 267:1–9, 2015.

[30] T. G. Graeber, C. Osmanian, T. Jacks, D. E. Housman, C. J. Koch, S. W. Lowe, and A. J. Giaccia. Hypoxia-mediated selection of cells with diminished apoptotic potential in solid tumours, 1996.

[31] K. Graham. Overcoming tumor hypoxia as a barrier to radiotherapy , chemotherapy and immunotherapy in cancer treatment. *International Journal of Nanomedicine*, pages 6049–6058, 2018.

[32] C. P. Guise, A. M. Mowday, A. Ashoorzadeh, R. Yuan, W. H. Lin, D. H. Wu, J. B. Smaill, A. V. Patterson, and K. Ding. Bioreductive prodrugs as cancer therapeutics: Targeting tumor hypoxia. *Chinese Journal of Cancer*, 33(2):80–86, 2014.

[33] C. Hajj, J. Russell, C. P. Hart, K. A. Goodman, M. A. Lowery, A. Haimovitz-Friedman, J. O. Deasy, and J. L. Humm. A Combination of Radiation and the Hypoxia-Activated Prodrug Evofosfamide (TH-302) is Efficacious against a Human Orthotopic Pancreatic Tumor Model. *Translational Oncology*, 10(5):760–765, 2017.

[34] E. M. Hammond, M. C. Asselin, D. Forster, J. P. B. O'Connor, J. M. Senra, and K. J. Williams. The Meaning, Measurement and Modification of Hypoxia in the Laboratory and the Clinic. *Clinical Oncology*, 26(5):277–288, 2014.

[35] D. Hanahan and R. A. Weinberg. Hallmarks of Cancer: The Next Generation. *Cell*, 144:646–674, 2011.

[36] H. L. P. Harpold, E. C. Alvord, and K. R. Swanson. The Evolution of Mathematical Modeling of Glioma Proliferation and Invasion. *Journal of Neuropathol Exp Neurol*, 66(1):1–9, 2007.

[37] A. L. Harris. Hypoxia a Key Regulatory Factor in Tumour Growth. *Nature Reviews Cancer*, 2(1):38–47, 2002.

[38] L. Harrison. Hypoxia and Anemia: Factors in Decreased Sensitivity to Radiation Therapy and Chemotherapy? *The Oncologist*, 9(suppl_5):31–40, 2004.

[39] K. O. Hicks, F. B. Pruijn, T. W. Secomb, M. P. Hay, R. Hsu, J. M. Brown, W. A. Denny, M. W. Dewhirst, and W. R. Wilson. Use of three-dimensional tissue cultures to model extravascular transport and predict in vivo activity of hypoxia-targeted anticancer drugs. *Journal of the National Cancer Institute*, 98(16):1118–1128, 2006.

[40] M. Hockel and P. Vaupel. Tumor Hypoxia: Definitions and Current Clinical, Biologic, and Molecular Aspects. *JNCI Journal of the National Cancer Institute*, 93(4):266–276, 2001.

[41] C. R. Hong, G. Bogle, J. Wang, K. Patel, F. B. Pruijn, W. R. Wilson, and K. O. Hicks. Bystander Effects of Hypoxia-Activated Prodrugs: Agent-Based Modeling Using Three Dimensional Cell Cultures. *Frontiers in Pharmacology*, 9(September):1–16, 2018.

[42] C. R. Hong, W. R. Wilson, and K. O. Hicks. An Intratumor Pharmacokinetic/Pharmacodynamic Model for the Hypoxia-Activated Prodrug Evofosfamide (TH-302): Monotherapy Activity is Not Dependent on a Bystander Effect. *Neoplasia (United States)*, 21(2):159–171, 2019.

[43] R. Hsu and T. W. Secomb. A Green's function method for analysis of oxygen delivery to tissue by microvascular networks. *Mathematical biosciences*, 96(1):61–78, 1989.

[44] F. W. Hunter, B. G. Wouters, and W. R. Wilson. Hypoxia-activated prodrugs: Paths forward in the era of personalised medicine. *British Journal of Cancer*, 114(10):1071–1077, 2016.

[45] R. K. Jain. Lessons from multidisciplinary translational trials on anti-angiogenic therapy of cancer. *Perspectives*, 8(april), 2008.

[46] S. M. F. Jamieson, P. Tsai, M. K. Kondratyev, P. Budhani, A. Liu, N. N. Senzer, E. G. Chiorean, S. I. Jalal, J. J. Nemunaitis, D. Kee, A. Shome, W. W. Wong, D. Li, N. Poonawala-Lohani, P. M. Kakadia, N. S. Knowlton, C. R. H. Lynch, C. R. Hong, T. W. Lee, R. A. Grénman, L. Caporiccio, T. D. McKee, M. Zaidi, S. Butt, A. M. J. Macann, N. P. McIvor, J. M. Chaplin, K. O. Hicks, S. K. Bohlander, B. G. Wouters, C. P. Hart, C. G. Print, W. R. Wilson, M. A. Curran, and F. W. Hunter. Evofosfamide for the treatment of human papillomavirus-negative head and neck squamous cell carcinoma. *JCI insight*, 3(16), aug 2018.

[47] P. Jayaprakash, M. Ai, A. Liu, P. Budhani, T. Bartkowiak, J. Sheng, C. R. Ager, C. Nicholas, A. R. Jaiswal, Y. Sun, K. Shah, S. Balasubramanyam, N. Li, G. Wang, J. Ning, A. Zal, T. Zal, M. A. Curran, A Michael, M. Ai, A. Liu, P. Budhani, T. Bartkowiak, J. Sheng, C. R. Ager, C. Nicholas, A. R. Jaiswal, Y. Sun, K. Shah, S. Balasubramanyam, N. Li, G. Wang, J. Ning, A. Zal, T. Zal, and M. A. Curran. Targeted hypoxia reduction restores T cell infiltration and sensitizes prostate cancer to immunotherapy. *Journal of Clinical Investigation*, sep 2018.

[48] L. Jones, P. Hoban, and P. Metcalfe. The use of the linear quadratic model in radiotherapy :. *Australasian Physical & Engineering Sciences in Medicine*, 24(3):132–133, 2001.

[49] Kim, S. J. and Jung, K. H. and Son, M. K. and Park, J. H. and Yan, H. H. and Fang, Z. and Kang, Y. W. and Han, B. and Lim, J. H. and Hong, S. S. Tumour Vessel Normalization by the PI3K Inhibitor HS-173 Enhances Drug Delivery. *Cancer Letters*, 403:339–353, 2017.

[50] M. Kohandel, C. A. Haselwandter, M. Kardar, S. Sengupta, and S. Sivaloganathan. Quantitative Model for Efficient Temporal Targeting of Tumor Cells and Neovasculature. *Computational and Mathematical Methods in Medicine*, 790721(10), 2011.

[51] M. Kohandel, M. Kardar, M. Milosevic, and S. Sivaloganathan. Dynamics of tumor growth and combination of anti-angiogenic and cytotoxic therapies. *Physics in Medicine and Biology*, 52(13):3665–3677, 2007.

[52] S. Kumar, J. D. Sun, L. Zhang, Reza B. M., B. Wu, F. Meng, Q. Liu, D. Bhupathi, Y. Wang, H. Yeger, C. Hart, and S. Baruchel. Hypoxia-Targeting Drug Evofosfamide (TH-302) Enhances Sunitinib Activity in Neuroblastoma Xenograft Models. *Translational Oncology*, 11(4):911–919, 2018.

[53] K. M. Laginha, S. Verwoert, G. J. R. Charrois, and T. M. Allen. Determination of doxorubicin levels in whole tumor and tumor nuclei in murine breast cancer tumors. *Clinical Cancer Research*, 11(19 I):6944–6949, 2005.

[54] D. Lindsay, C. M. Garvey, S. M. Mumenthaler, and J. Foo. Leveraging Hypoxia-Activated Prodrugs to Prevent Drug Resistance in Solid Tumors. *PLoS Computational Biology*, 12(8):1–25, 2016.

[55] Q. Liu, J. D. Sun, J. Wang, D. Ahluwalia, A. F. Baker, L. D. Cranmer, D. Ferraro, Y. Wang, J. X. Duan, W. S. Ammons, J. G. Curd, M. D. Matteucci, and C. P. Hart. TH-302, a hypoxia-activated prodrug with broad in vivo preclinical combination therapy efficacy: Optimization of dosing regimens and schedules. *Cancer Chemotherapy and Pharmacology*, 69(6):1487–1498, 2012.

[56] S. Liu, M. T. Tetzlaff, T. Wang, X. Chen, R. Yang, S. M. Kumar, A. Vultur, P. Li, J. S. Martin, M. Herlyn, R. Amaravadi, B. Li, X. Xu, S. Liu, M. T. Tetzlaff, T. Wang, X. Chen, R. Yang, S. M. Kumar, A. Vultur, P. Li, J. S. Martin, M. Herlyn, R. Amaravadi, B. Li, and X. Xu. Hypoxia-activated prodrug enhances therapeutic effect of sunitinib in melanoma. *Oncotarget*, 8(70):115140–115152, 2017.

[57] A. Logg, G. N. Wells, and J. Hake. *DOLFIN: a C++/Python Finite Element Library*, chapter 10. Springer, 2012.

[58] I. Lohse, J. Rasowski, P. Cao, M. Pintilie, T. Do, M. Tsao, R. P. Hill, and D. W. Hedley. Targeting hypoxic microenvironment of pancreatic xenografts with the hypoxia-activated prodrug TH-302. *Oncotarget*, 7(23), 2016.

[59] S. Lonardi, A. Tosoni, and A. A Brandes. Adjuvant chemotherapy in the treatment of high grade gliomas. *Cancer Treatment Reviews*, 31(2):79–89, 2005.

[60] K. R. Luoto, R. Kumareswaran, and R. G. Bristow. Tumor hypoxia as a driving force in genetic instability. *Genome Integrity*, 4(1):1, 2013.

[61] X. Mao, S. Mcmanaway, J. K. Jaiswal, P. B. Patel, R. Wilson, Hicks K. O., and G. Bogle. An agent-based model for drug-radiation interactions in the tumour microenvironment : Hypoxia-activated prodrug SN30000 in multicellular tumour spheroids. *PLOS Computational Biology*, pages 1–30, 2018.

[62] J. D. Martin, G. Seano, and R. K. Jain. Normalizing Function of Tumor Vessels : Progress , Opportunities , and Challenges. *Annual Review of Physiology*, 81:505–534, 2019.

[63] W. P. Mason and J. G. Cairncross. Drug Insight: temozolomide as a treatment for malignant glioma–impact of a recent trial. *Nature clinical practice. Neurology*, 1(2):88–95, 2005.

[64] D. M. McDonald and P. L. Choyke. Imaging of angiogenesis: From microscope to clinic. *Nature Medicine*, 9(6):713–725, 2003.

[65] C. Meaney, G. G. Powathil, A. Yaromina, L. J. Dubois, P. Lambin, and M. Kohandel. Role of hypoxia-activated prodrugs in combination with radiation therapy: An in silico approach. *In submission*, 2019.

[66] A. I. Minchinton and I. F. Tannock. Drug penetration in solid tumours. *Nature Reviews Cancer*, 6(8):583–592, 2006.

[67] I. N. Mistry, M. Thomas, E. D. D. Calder, S. J. Conway, and E. M. Hammond. Clinical Advances of Hypoxia-Activated Prodrugs in Combination With Radiation Therapy. *International Journal of Radiation Oncology Biology Physics*, 98(5):1183–1196, 2017.

[68] J. D. Murray. *Mathematical Biology : I . An Introduction , Third Edition*, volume 1. Springer, 2002.

[69] J. D. Murray. *Mathematical Biology II - Spatial Models and Biomedical App lications*. Springer, 2008.

[70] K. J. Nytko, I. Grgic, S. Bender, J. Ott, M. Guckenberger, O. Riesterer, and M. Pruschy. The hypoxia-activated prodrug evofosfamide in combination with multiple regimens of radiotherapy. *Oncotarget*, 8(14):23702–23712, 2017.

[71] F. Pappalardo, G. Russo, F. M. Tshinanu, and M. Viceconti. In silico clinical trials: concepts and early adoptions. *Briefings in Bioinformatics*, 1(April):1–10, 2018.

[72] S. Peeters, C. M. L. Zegers, R. Biemans, N. G. Lieuwes, R. G. P. M. Van Stiphout, A. Yaromina, J. D. Sun, C. P. Hart, A. D. Windhorst, W. Van Elmpt, L. J. Dubois, and P. Lambin. TH-302 in combination with radiotherapy enhances the therapeutic outcome and is associated with pretreatment [¹⁸F]HX4 hypoxia PET imaging. *Clinical Cancer Research*, 21(13):2984–2992, 2015.

[73] S. F. Petit, A. L. A. J. Dekker, R. Seigneuric, L. S. Murrer, N. A. W. Van Riel, M. Nordsmark, J. Overgaard, P. Lambin, and B. G. Wouters. Intra-voxel heterogeneity influences the dose prescription for dose-painting with radiotherapy: A modelling study. *Physics in Medicine and Biology*, 54(7):2179–2196, 2009.

[74] R. M. Phillips. Targeting the hypoxic fraction of tumours using hypoxia-activated prodrugs. *Cancer Chemotherapy and Pharmacology*, 77(3):441–457, 2016.

[75] C. Phipps and M. Kohandel. Mathematical model of the effect of interstitial fluid pressure on angiogenic behavior in solid tumors. *Computational and Mathematical Methods in Medicine*, 2011, 2011.

[76] G. Powathil, M. Kohandel, M. Milosevic, and S. Sivaloganathan. Modeling the spatial distribution of chronic tumor hypoxia: Implications for experimental and clinical studies. *Computational and Mathematical Methods in Medicine*, 2012, 2012.

[77] G. Powathil, M. Kohandel, S. Sivaloganathan, A. Oza, and M. Milosevic. Mathematical modeling of brain tumors: Effects of radiotherapy and chemotherapy. *Physics in Medicine and Biology*, 52(11):3291–3306, 2007.

[78] Maziar Raissi and George Em Karniadakis. Hidden physics models: Machine learning of nonlinear partial differential equations. *Journal of Computational Physics*, 357:125–141, 2018.

[79] Maziar Raissi, Paris Perdikaris, and George Em Karniadakis. Physics Informed Deep Learning (Part I): Data-driven Solutions of Nonlinear Partial Differential Equations. *Journal of Computational Physics*, 1(Part I):1–22, 2017.

[80] Maziar Raissi, Paris Perdikaris, and George Em Karniadakis. Physics Informed Deep Learning (Part II): Data-driven Discovery of Nonlinear Partial Differential Equations. *Journal of Computational Physics*, 1(Part II):1–19, 2017.

[81] R. Rockne, E. C. Alvord, J. K. Rockhill, and K. R. Swanson. A mathematical model for brain tumor response to radiation therapy. *Journal of Mathematical Biology*, 58(4-5):561–578, 2009.

[82] R. Rockne, J. K. Rockhill, M. Mrugala, A. M. Spence, I. Kalet, K. Hendrickson, A. Lai, T. Cloughesy, E. C. Alvord, and K. R. Swanson. Predicting the efficacy of radiotherapy in individual glioblastoma patients in vivo: a mathematical modeling approach. *Physics in Medicine and Biology*, 55(12):3271–3285, 2010.

[83] M. Sabir, A. Shah, W. Muhammad, I. Ali, and P. Bastian. A mathematical model of tumor hypoxia targeting in cancer treatment and its numerical simulation. *Computers and Mathematics with Applications*, 74(12):3250–3259, 2017.

[84] J. K. Saggar and I. F. Tannock. Activity of the hypoxia-activated pro-drug TH-302 in hypoxic and perivascular regions of solid tumors and its potential to enhance therapeutic effects of chemotherapy. *International Journal of Cancer*, 134(11):2726–2734, 2014.

[85] T. W. Secomb, R. Hsu, R. D. Braun, J. R. Ross, J. F. Gross, and M. W. Dewhirst. Theoretical simulation of oxygen transport to tumors by three-dimensional networks of microvessels., 1998.

[86] S. Sengupta, D. Eavarone, I. Capila, G. Zhao, N. Watson, T. Kiziltepe, and R. Sasisekharan. Temporal targeting of tumour cells and neovasculature with a nanoscale delivery system. *Nature*, 436(7050):568–572, 2005.

[87] N. A. Stavreva, P. V. Stavrev, and W. H. Round. A mathematical approach to optimizing the radiation dose distribution in heterogeneous tumours. *Acta Oncologica*, 35(6):727–732, 1996.

[88] J. Stingele, R. Bellelli, and S. J. Boulton. Mechanisms of DNA-protein crosslink repair. *Nat. Rev. Mol. Cell Biol.*, 18(9):563–573, Sep 2017.

[89] M. Su, J. Huang, S. Liu, Y. Xiao, X. Qin, J. Liu, C. Pi, T. Luo, J. Li, X. Chen, and Z. Luo. The anti-angiogenic effect and novel mechanisms of action of Combretastatin A-4. *Scientific Reports*, 6(June):1–11, 2016.

[90] M. Su, L. Zhang, Z. Huang, J. Shi, and J. Lu. Investigational Hypoxia-Activated Prodrugs: Making Sense of Future Development. *Current Drug Targets*, 20, 2018.

[91] J. D. Sun, Q. Liu, J. Wang, D. Ahluwalia, D. Ferraro, Y. Wang, J. Duan, W. S. Ammons, J. G. Curd, M. D. Matteucci, and C. P. Hart. Selective tumor hypoxia targeting by hypoxia-activated prodrug TH-302 inhibits tumor growth in preclinical models of cancer. *Clinical Cancer Research*, 18(3):758–770, 2012.

[92] K. R. Swanson, E. C. Alvord, and J. D. Murray. A quantitative model for differential motility of gliomas in grey and white matter. *Cell Proliferation*, 33(5):317–329, 2000.

[93] P. Tracqui, G. C. Cruywagen, D. E. Woodward, G. T. Bartooll, J. D. Murray, E. C. Alvord, and E. C. Alvord. A mathematical model of glioma growth: the effect of chemotherapy on spatio-temporal growth. *Cell ProliJ*, 28:17–3, 1995.

[94] L. N. Trefethen and N. Trefethen. *Finite Difference and Spectral Methods for Ordinary and Partial Differential Equations*. unpublished, 1996.

[95] J. Unkelbach, B. H. Menze, E. Konukoglu, F. Dittmann, N. Ayache, and H. A. Shih. Radiotherapy planning for glioblastoma based on a tumor growth model: Implications for spatial dose redistribution. *Physics in Medicine and Biology*, 59(3):771–789, 2014.

[96] P. Vaupel and A. Mayer. Hypoxia in cancer: Significance and impact on clinical outcome. *Cancer and Metastasis Reviews*, 26(2):225–239, 2007.

[97] C. V. M. Verhagen, D. M. Vossen, K. Borgmann, F. Hageman, R. Grenman, M. Verwijs-Janssen, L. Mout, R. J. C. Kluin, M. Nieuwland, T. M. Severson, A. Velds, R. Kerkhoven, M. J. O'Connor, M. van der Heijden, M. L. van Velthuysen, M. Verheij, V. B. Wreesmann, L. F. A. Wessels, M. W. M. van den Brekel, and C. Vens. Fanconi anemia and homologous recombination gene variants are associated with functional DNA repair defects in vitro and poor outcome in patients with advanced head and neck squamous cell carcinoma. *Oncotarget*, 9(26):18198–18213, Apr 2018.

[98] S. Webb, P. M. Evans, W. Swindell, and J. O. Deasy. A proof that uniform dose gives the greatest TCP for fixed integral dose in the planning target volume. *Physics in Medicine and Biology*, 39(11):2091–2098, 1994.

[99] R. Weinberg. *The biology of cancer*. Garland Science, Taylor and Francis Group, 2006.

[100] I. B. Weinstein and K. Case. The history of cancer research: Introducing an AACR centennial series. *Cancer Research*, 68(17):6861–6862, 2008.

[101] G. J. Weiss, J. R. Infante, E. G. Chiorean, M. J. Borad, J. C. Bendell, J. R. Molina, R. Tibes, R. K. Ramanathan, K. Lewandowski, S. F. Jones, M. E. Lacouture, V. K. Langmuir, H. Lee, S. Kroll, and H. A. Burris. Phase 1 study of the safety, tolerability, and pharmacokinetics of TH-302, a hypoxia-activated prodrug, in patients with advanced solid malignancies. *Clinical Cancer Research*, 17(9):2997–3004, 2011.

[102] W. R. Wilson and M. P. Hay. Targeting hypoxia in cancer therapy, 2011.

[103] F. Winkler, S. V. Kozin, R. T. Tong, S. Chae, M. F. Booth, I. Garkavtsev, L. Xu, D. J. Hicklin, D. Fukumura, E. di Tomaso, L. L. Munn, and R. K. Jain. Kinetics of Vascular Normalization by VEGFR2 Blockade Governs Brain Tumor Response to Radiation. *Cancer Cell*, 6(6):553–563, 2004.

[104] A. Yaromina, M. Granzier, R. Biemans, N. Lieuwes, W. van Elmpt, G. Shakirin, L. Dubois, and P. Lambin. A novel concept for tumour targeting with radiation: Inverse dose-painting or targeting the Low Drug Uptake Volume. *Radiotherapy and Oncology*, 124(3):513–520, 2017.

[105] S. Yonucu, Y. Defne, C. Phipps, M. B. Unlu, and M. Kohandel. Quantifying the effects of antiangiogenic and chemotherapy drug combinations on drug delivery and treatment efficacy. *PLoS Computational Biology*, pages 1–17, 2017.

[106] C. Yoon, H. J. Lee, D. J. Park, Y. J. Lee, W. D. Tap, T. S. K. Eisinger-Mathason, C. P. Hart, E. Choy, M. C. Simon, and S. S. Yoon. Hypoxia-activated chemotherapeutic TH-302 enhances the effects of VEGF-A inhibition and radiation on sarcomas. *British Journal of Cancer*, 113(1):46–56, 2015.

[107] M. Yoon. A new homogeneity index based on the statistical analysis of dose volume histogram. *Journal of Applied Clinical Medical Physics*, 8(2):9–17, 2007.

[108] Z. Yun, M. Jingwen, Y. Z. Chen, X. Q. Z. Xinyi, and L. X. Jimin. Hypoxia-activated prodrugs and redox-responsive nanocarriers. *International Journal of Nanomedicine*, 2018.

APPENDICES

Appendix A

Spatial Optimization for Radiation of Brain Tumours - Appendix Material

A.1 Proof of Uniform Resulting Cell Density for Arbitrary Death Mechanism

We have seen in the previous sections that the resulting cell density profile after one fraction of radiation is uniform for both exponential and logistic death. However, one might wonder whether this result holds for any arbitrary death mechanism. In fact, this is the case, and for any arbitrary radiation death mechanism, $g(n(r,t))$, the cytotoxic profile which minimizes the total number of surviving cells results in a uniform cell density.

To show this, we first modify Eq. (5) to include the arbitrary death mechanism

$$\frac{\partial n}{\partial t} = -\gamma f(r) g(n(r,t)),$$

where $g(n(r,t))$ is the death mechanism (ie. exponential, logistic, or other). Note that we are still limited here to the death rate being proportional to $f(r,t)$; we suspect that this result is not true for arbitrary functions of $f(r,t)$. Integrating this equation with respect to t over the fraction (total time of Δt) yields:

$$\int_{n_0(r)}^{n_1(r)} \frac{dn}{g(n(r,t))} = -\gamma \Delta t f(r).$$

We now differentiate this equation with respect to f, using the Fundamental Theorem of Calculus, and the fact that $\frac{\partial n_0}{\partial f} = 0$ (since the initial cell density is of course independent of our radiation profile). This leaves us simply with

$$\frac{\partial n_1}{\partial f}\frac{1}{g(n_1(r))} = -\gamma\Delta t. \tag{A.1}$$

Then, from our optimization constraint (equivalent to Eq. (8))

$$\tilde{N_1} = \int d^d\vec{x}\ n_1(r) + \lambda\Big(\int d^d\vec{x}\ f(\vec{x}, t_0) - F\Big),$$

we can use the Euler-Lagrange Equation to arrive at the constraint on f of

$$\frac{\partial n_1}{\partial f} + \lambda = 0.$$

Substituting this into Eq. (A.1) above and rearranging gives:

$$g(n_1) = \frac{\lambda}{\gamma\Delta t}.$$

Since λ, γ, and Δt are all constants, and $g(n_1(r))$ only explicitly depends on $n_1(r)$, this equation can be rearranged to solve for $n_1(r)$ as a constant for any arbitrary and invertible function $g(n(r,t))$.

Thus, the continuous profile which minimizes the total number of surviving cells will always yield a uniform surviving cell density.

A.2 Optimal Profile with Two Fractions of Exponential Death

The optimal XRT profile in the first fraction naturally does not depend on the tumour growth mechanism. However, it is reasonable to expect that the additional growth of the tumour prior to application of the second fraction will lead to joint optimal profiles that do. Since it it difficult to treat the full non-linear (logistic) growth, we make the further assumption that the growth process in the interval between the two fractions is exponential (this will be the case if the initial fraction reduces the density to well below n_{max}, and the

interval between the two fractions is short enough for $n(\vec{x},t)$ to remain smaller than this saturation value). Formal integration of the linear partial differential equation now leads to the following cell density profile after a time $t_1 = t_0 + \tau$ since application of the first fraction

$$n(\vec{x},t_1) = \exp\left[\tau\left(\rho + D_n\nabla^2\right)\right] * \left[e^{-f(\vec{x},t_0)}n(\vec{x},t_0)\right], \tag{A.2}$$

where $*$ indicates a convolution of the 2 functions and τ is the time between fractions.

If the resulting cell density from the first fraction was uniform, then Eq. (A.2) will simply leave us with another uniform distribution, in which case, the optimal radiation fraction is, of course, uniform. However, if the optimal first fraction was cut-off as in the semi-circular example above, then we will have to take more care in the application of our second fraction. Leaving the cell density general, following the application of a second fraction, the cell density is

$$n(\vec{x},t_1+\Delta t) = e^{-f_2(\vec{x})}\exp\left[\tau\left(\rho + D_n\nabla^2\right)\right] * \left[e^{-f_1(\vec{x})}n(\vec{x},t_0)\right], \tag{A.3}$$

where we have used $f_1(\vec{x}) \equiv f(\vec{x},t_0)$ and $f_2(\vec{x}) \equiv f(\vec{x},t_1)$. Using properties of the diffusion operator, the total number of tumour cells after the second fraction can be written as

$$N_2 = e^{\rho\tau}\int \frac{d^d\vec{x}d^d\vec{x'}}{(2\pi D\tau)^{d/2}}\ \left(e^{-f_2(\vec{x})}\right)e^{-\frac{(\vec{x'}-\vec{x})^2}{2D\tau}}\left(e^{-f_1(\vec{x'})}n(\vec{x'},t_0)\right). \tag{A.4}$$

Minimizing the above expression, we arrive at the conditions

$$\left[e^{-f_2(\vec{x})}\right]e^{\tau D_n\nabla^2}\left[e^{-f_1(\vec{x})}n(\vec{x},t_0)\right] = \lambda_2 e^{-\rho\tau}, \tag{A.5}$$

$$\left[e^{-f_1(\vec{x})}n(\vec{x},t_0)\right]e^{\tau D_n\nabla^2}\left[e^{-f_2(\vec{x})}\right] = \lambda_1 e^{-\rho\tau}. \tag{A.6}$$

Here, λ_1 and λ_2 are distinct Lagrange multipliers to impose separate constraints on the total flux in each fraction. If the constraint acts only on the sum of the two fractions, then $\lambda_1 = \lambda_2 = \lambda$. Actually, the equations are symmetric with respect to exchange of the functions $\Phi_1(\vec{x}) \equiv e^{-f_1(\vec{x})}n(\vec{x},t_0)$ and $\Phi_2(\vec{x}) \equiv e^{-f_2(\vec{x})}n(\vec{x},t_0)$, suggesting solutions of the form $\Phi_1(\vec{x}) = \Phi_2(\vec{x})$ implying $\lambda_1 = \lambda_2$, i.e. constraining radiation in each fraction, or in the sum, would correspond to the same optimal solution. In the absence of other constraints, the above equations are solved by $\nabla^2\Phi_1 = \nabla^2\Phi_2 = 0$, i.e. position-independent Φ_1 and Φ_2. This again leads to $f_1 = \ln(n_0/\lambda)$ (as in Eq. (9)), albeit for a different reason) followed by a uniform f_2. This general solution is not particularly useful and may not be viable given various constraints.

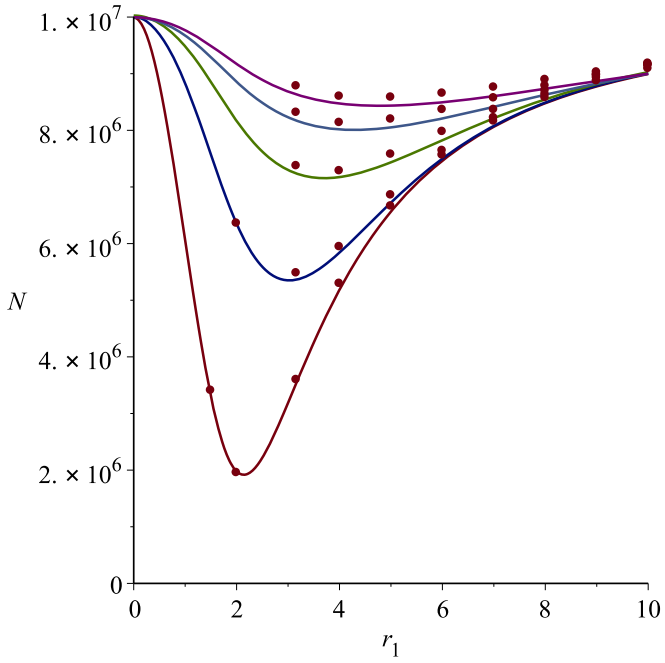

Figure A.1: Total cells after first fraction vs. radius of step in cytotoxic profile. The solid lines correspond to different values of σ with red for $\sigma = 1$, blue for $\sigma = 2$, green for $\sigma =$, teal for $\sigma = 4$, and purple for $\sigma = 5$. The dots correspond to individual runs of the pseudo-spectral method.

A.3 Additional Figures and Simulations

In addition to the optimization procedure outlined in the main text of the paper, Eq. (2) was also implemented numerically using a pseudo-spectral method [94]. Using this implementation, the results from the optimization procedure can be checked. As an illustrative example of this, take the case of the 1-step cytotoxic profile with logistic growth and death. Using the psuedo-spectral implementation, Eq. (2) (with $a = b = 0$) was simulated for many different forms of $f(r, t)$ and the total cell number N calculated immediately after the fraction. The $f(r, t)$ that produced the minimum cell number from this method was obtained and compared to the optimal $f(r, t)$ from the procedure in the main text. Fig. S2 shows some justification of the agreement of the 2 methods on the optimal profile.

From this numerical method, the cell-density profiles were also obtained so that the results can be better visualized. These figures are shown in Fig. S3 through S9.

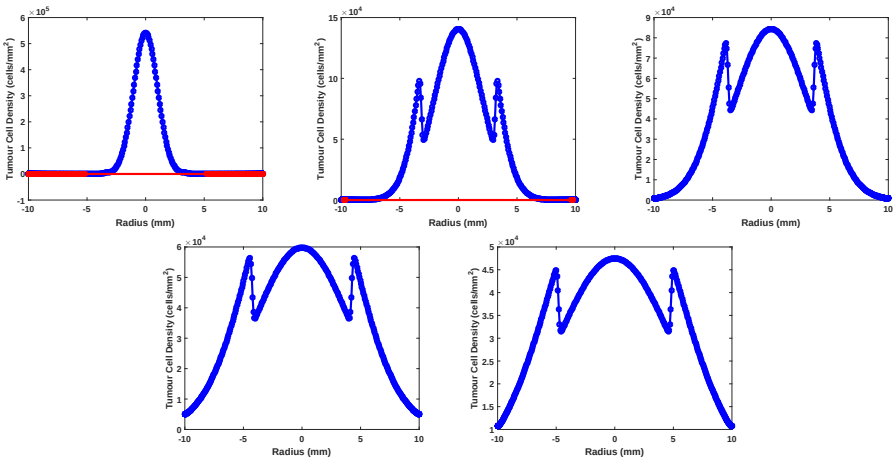

Figure A.2: Cell densities resulting from the optimal radiation profiles from one 1-step fraction of exponential growth and death for the initial density deviations of (from top left to bottom right) $\sigma = 1$, $\sigma = 2$, $\sigma = 3$, $\sigma = 4$, and $\sigma = 5$. The red dots are those below the detectable threshold in imaging, of 5 cells/mm^2, and the blue dots those above. Note the different y-axis scales to highlight the resulting shape.

For simulations we employ values of $\rho = 0.35$ (1/day) and $D_n = 0.32$ (mm^2/day) in Eq. (1), in accord with common works and previous measurements [51], although the results are not sensitive to this choice.

For cases with logistic growth, we cannot use a Gaussian as our initial profile. Logistic growth causes the tumour to form a flat-top profile as the density in the centre approaches n_{max}. Since Eq. (1) has no analytical solution for logistic growth, we instead use a numerical technique to find the initial profile. Starting with initial profiles in the form of normal distributions, with widths $\sigma = 1$, 3, and 5, the density profile is simulated with logistic growth for a time of 12.5 days. The resulting profile is then fitted to Eq. (35).

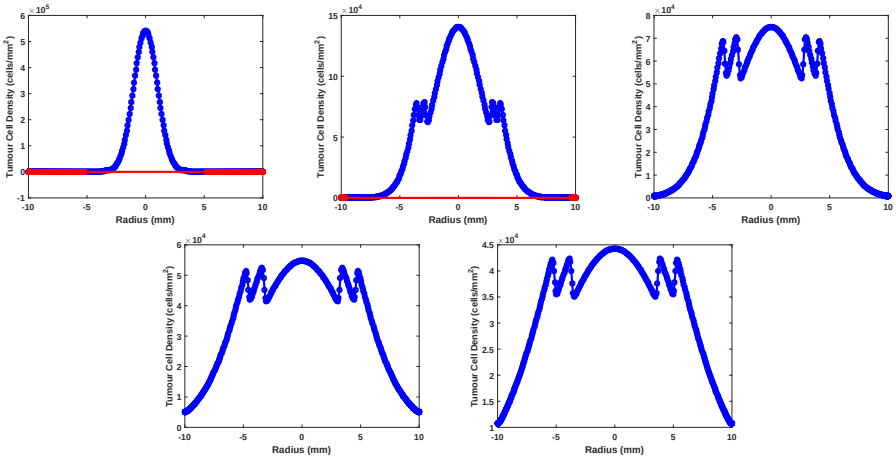

Figure A.3: Cell densities resulting from the optimal radiation profiles from one 2-step fraction of exponential growth and death for the initial density deviations of (from top left to bottom right) $\sigma = 1$, $\sigma = 2$, $\sigma = 3$, $\sigma = 4$, and $\sigma = 5$. The red dots are those below the detectable threshold in imaging, of 5 cells/mm^2, and the blue dots those above. Note the different y-axis scales to highlight the resulting shape.

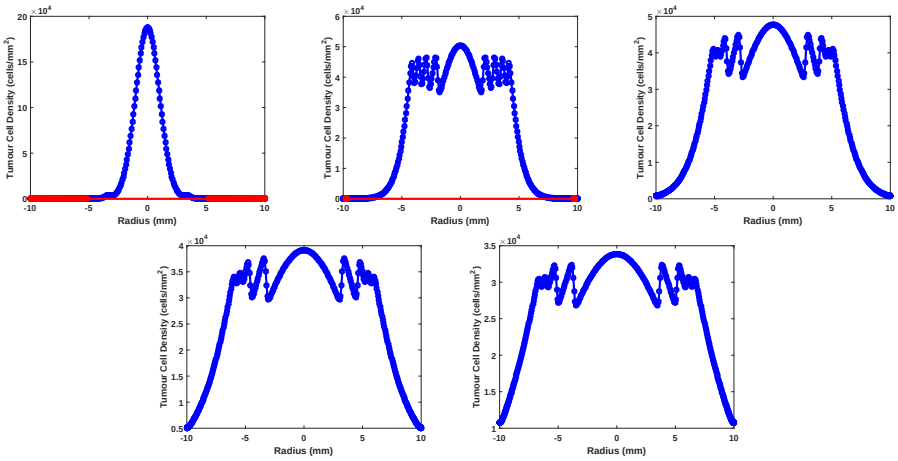

Figure A.4: Cell densities resulting from the optimal radiation profiles from two separately constrained 2-step fraction of exponential growth and death for the initial density deviations of (from top left to bottom right) $\sigma = 1$, $\sigma = 2$, $\sigma = 3$, $\sigma = 4$, and $\sigma = 5$. The red dots are those below the detectable threshold in imaging, of 5 cells/mm^2, and the blue dots those above. Note the different y-axis scales to highlight the resulting shape.

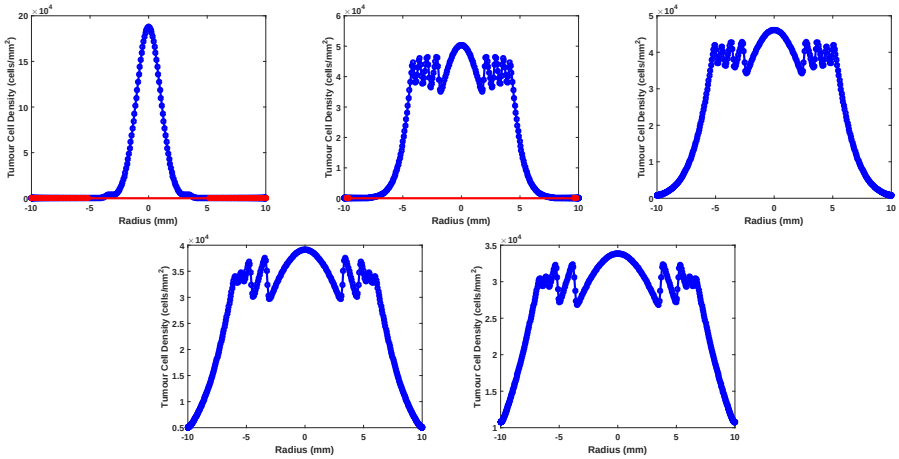

Figure A.5: Cell densities resulting from the optimal radiation profiles from two mutually constrained 2-step fraction of exponential growth and death for the initial density deviations of (from top left to bottom right) $\sigma = 1$, $\sigma = 2$, $\sigma = 3$, $\sigma = 4$, and $\sigma = 5$. The red dots are those below the detectable threshold in imaging, of 5 cells/mm^2, and the blue dots those above. Note the different y-axis scales to highlight the resulting shape.

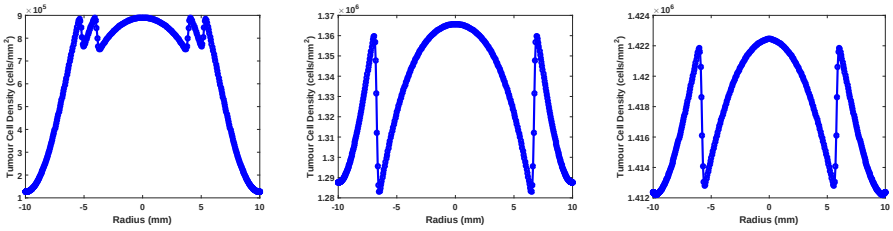

Figure A.6: Cell densities resulting from the optimal radiation profiles from one 2-step fraction of logistic growth and exponential death for the initial density deviations of (from left to right) $\sigma = 1$, $\sigma = 3$, and $\sigma = 5$. The red dots are those below the detectable threshold in imaging, of 5 cells/mm^2, and the blue dots those above. Note the different y-axis scales to highlight the resulting shape.

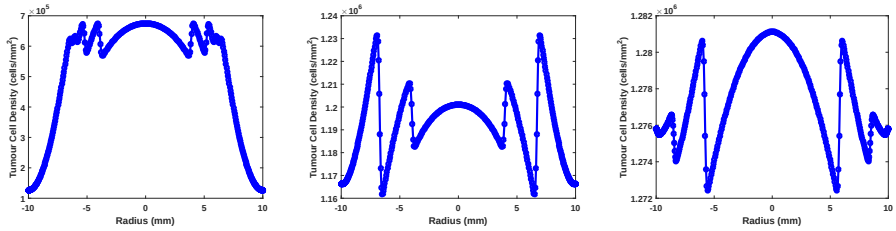

Figure A.7: Cell densities resulting from the optimal radiation profiles from two 2-step fractions of logistic growth and exponential death of (from left to right) $\sigma = 1$, $\sigma = 3$, and $\sigma = 5$. The red dots are those below the detectable threshold in imaging, of 5 cells/mm^2, and the blue dots those above. Note the different y-axis scales to highlight the resulting shape.

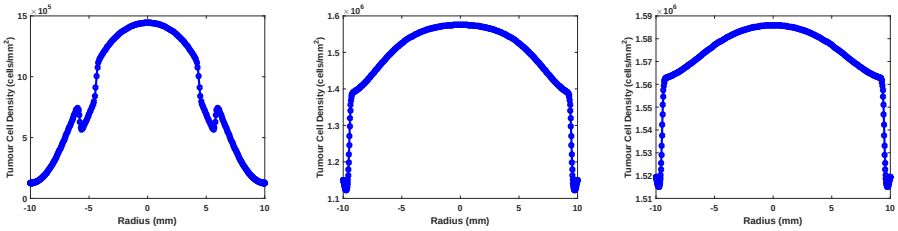

Figure A.8: Cell densities resulting from the optimal radiation profiles from one 2-step fraction of logistic growth and death of (from left to right) $\sigma = 1$, $\sigma = 3$, and $\sigma = 5$. The red dots are those below the detectable threshold in imaging, of 5 cells/mm^2, and the blue dots those above. Note the different y-axis scales to highlight the resulting shape.

Appendix B

In Silico Analysis of Hypoxia-Activated Prodrugs in Combination with Anti-Angiogenic Therapy through Nanocell Delivery - Appendix Material

B.1 Nondimensionalization of System

The tumour growth/treatment system is nondimensionalized using the transformations

$$x = \tilde{x}\sqrt{\frac{D_n}{r}}, \quad t = \frac{\tilde{t}}{r}, \quad n = \tilde{n}n_{lim}. \tag{B.1}$$

The system is implemented computationally using the nondimensionalized version.

B.2 Derivation of Release Profile Normalization Constant

To ensure a fair comparison between the administration types, the plasma concentration of the drugs should be the same. To do this, the release profiles are integrated. For the

separate administration:

$$\int_{t_0}^{\infty} e^{-\frac{(t-t_0)}{t_i}} dt = t_i, \tag{B.2}$$

where t_i is the half life of the drug. Then for the nanocell administration:

$$\int_{t_0}^{\infty} (t-t_0)^{P_i} e^{-\frac{(t-t_0)}{t_i}} dt = t_i^{1+P_i} \Gamma(1+P_i). \tag{B.3}$$

So, equating these with a normalization constant implies that the normalization constant for each drug must be:

$$N_i = \frac{1}{t_i^{P_i} \Gamma(1+P_i)}. \tag{B.4}$$

This is the form of the normalization constant used to implement the drug schedules.